FRIEDRICH-SCHILLER-UNIVERSITÄT JENA

Methods for *in silico* design of innovative materials

Dissertation

To Fulfill the Requirements for the Degree of
doctor rerum naturalium (Dr. rer. nat.)
in the Field Materials Science.

Submitted to the Council of the: Faculty of Physics and Astronomy
                                    of the Friedrich Schiller University Jena

by: M.Sc. Andreas Erlebach
                                    born on April 12, 1988 in Suhl.

May 28, 2019

1st referee:	Prof. Dr. Marek Sierka
2nd referee:	Prof. Dr. Petr Nachtigall
3rd referee:	Prof. Dr. Stefanie Gräfe

Disputation:	Jena, September 27, 2019

"Building models is very different from proclaiming truths. It's a never-ending process of discovery and refinement, not a war to win or destination to reach. Uncertainty is intrinsic to the process of finding out what you don't know, not a weakness to avoid. Bugs are features – violations of expectations are opportunities to refine them. And decisions are made by evaluating what works better, not by invoking received wisdom."

Neil Gershenfeld in "Truth is a Model" (2011)

Abstract

Time and cost efficient optimization of existing and design of novel materials is achieved by prediction of the materials structure and properties by employing computational - *in silico* - methods. For this purpose, pragmatic approaches for the targeted materials design are presented providing good compromise of prediction accuracy and computational efforts by the exploitation of synergy between atomistic simulations and experiments. This is exemplarily shown for three distinct types of materials.

The first example concerns predictions of the phase stability and thermomechanical properties for optimization of the microstructure of zero thermal expansion glass ceramics consisting of $Ba_{1-m}Sr_mZn_{2-2n}Mg_{2n}Si_2O_7$ (BZS) solid solutions. First, the tunable temperature of the martensitic phase transition T_t from the low to the desired high temperature (HT) phase of BZS solid solutions showing negative thermal expansion is predicted. This is achieved by calculations of the vibrational density of states at the density functional theory (DFT) level using the harmonic approximation (HA). Since calculations using the HA fail to predict T_t even qualitatively, model functions for the vibrational free energy are derived from DFT simulations in combination with an empirical correction using experimentally observed T_t for consideration of anharmonic effects avoiding computationally demanding *ab initio* simulations. Predictions of T_t for chemical compositions not included in the model derivation show good agreement with experimental observations. In addition, those chemical compositions at which the HT phase emerges from glass crystallization can be rapidly predicted by using the proposed computational approach. Among these compositions are $Ba_{1-m}Sr_mZn_2Si_2O_7$ solid solutions with $m > 0.1$. The thermomechanical properties of the HT phase of $Ba_{1-m}Sr_mZn_2Si_2O_7$ as a function of the chemical composition m are elucidated, namely, the elastic constants, thermal expansion and macroscopic Grüneisen parameters by combining DFT simulations with experimentally determined lattice parameters. Moreover, the origin of the negative thermal expansion at the atomic level is revealed for $Ba_{0.5}Sr_{0.5}Zn_2Si_2O_7$ by calculation of the microscopic Grüneisen parameters using DFT simulations along with the quasi-harmonic approximation.

The second case study is the elucidation of atomic structure and crystallization of nanoparticulate Fe_2O_3 starting from its smallest Fe_2O_3 building block up to nanometer-sized Fe_2O_3 particles. Structure predictions of small $(Fe_2O_3)_n$ ($n = 1$-10) gas phase clusters used global structure optimizations along with a two stage procedure that combines tailored, *ab initio* derived interatomic potential functions (IP) with refinements at the DFT level. Computations for the crystallization of larger nanoparticles up to a diameter of 5 nm used molecular dynamics simulations along with the tailored IP. Most of the $(Fe_2O_3)_n$ clusters show compact, almost amorphous structures with little or no symmetry, except for the tetrahedral, adamantane-like $(Fe_2O_3)_2$ structure. Larger gas phase clusters with $n > 5$ increasingly assume tetrahedral shape with the adamantane-like $(Fe_2O_3)_2$ entity as the main building unit. Such tetrahedral morphology persists for Fe_2O_3 nanoparticles with diameters up to 3 nm. In contrast, single crystals

with hexagonal morphology were obtained by simulated crystallization of larger nanoparticles with diameters of about 5 nm leading to formation of ϵ-Fe$_2$O$_3$. The hexagonal morphology is in excellent agreement with the results obtained for fabricated Fe$_2$O$_3$ nanopowders confirming the reliability of the computational procedure employed and providing the first direct indication that ϵ-Fe$_2$O$_3$ may be thermodynamically the most stable phase for nanoparticles of this size. In addition, the atomistic structure models predicted can serve as a starting point for future simulations to shed a light on the thermodynamic and magnetic properties of nanoparticulate Fe$_2$O$_3$.

Finally, the third example case focusses on the optimization of polymeric nanocarriers for the efficient encapsulation of biologically active substances such as drugs. The thermodynamic compatibility of polymers with low molecular weight compounds is evaluated using thermodynamic models parameterized by atomistic simulations. Here, a computationally efficient procedure based on the concept of inherent structures is proposed for the profound statistical sampling of polymer conformations. Comprehensive test simulations confirm the accuracy of the employed simulation procedure for calculation of the physico-chemical properties such as cohesive energy densities (CED). Calculation of the CED along with their energetic contributions allow the determination of (Hansen) solubility parameters that facilitate rapid, qualitative solubility predictions in combination with the Flory-Huggins (FH) theory. However, the FH theory fails to model specific interactions such as hydrogen bonding, even though atomistic simulations of polymer mixtures explicitly consider such interactions. Therefore, the more accurate perturbed hard sphere chain (PHSC) equation of state (EOS) was parameterized by using not only calculated CED but also pressures as a function of the temperature. As test case, aqueous polyethylene glycol (PEG) solutions have been chosen, which are known to show strong hydrogen bonding. The physico-chemical properties including the phase diagram of PEG-water calculated by the PHSC EOS show good agreement with experimental observations. Consequently, a two stage procedure is proposed for the efficient *in silico* guided design of polymeric drug nanocarriers. It combines qualitative solubility predictions using the FH theory for rapid prescreening of promising polymers that efficiently solubilize active substances with computationally more demanding simulations for consideration of specific interactions and an accurate modeling of the physico-chemical properties by parameterization of the PHSC EOS.

Zusammenfassung

Die zeit- und kosteneffiziente Optimierung existierender sowie das Designs neuer Materialien wird durch die Vorhersage der Materialstruktur und -eigenschaften mithilfe rechengestützter - *in silico* - Methoden erzielt. Zu diesem Zweck werden pragmatische Ansätze für das gezielte Materialdesign vorgestellt, die einen guten Kompromiss zwischen Vorhersagegenauigkeit und Rechenaufwand darstellen, indem Synergien zwischen atomistischen Simulationen und Experimenten genutzt werden. Dies wird beispielhaft für drei verschiedene Arten von Materialien gezeigt.

Das erste Beispiel betrifft Vorhersagen der Phasenstabilität und der thermomechanischen Eigenschaften zur Optimierung der Mikrostruktur von Glaskeramiken mit null Wärmeausdehnung, bestehend aus $Ba_{1-m}Sr_mZn_{2-2n}Mg_{2n}Si_2O_7$ (BZS) Mischkristallen. Zunächst wird die anpassbare Temperatur des martensitischen Phasenübergangs T_t von der Tief- zur gewünschten Hochtemperatur-Phase (HT) der BZS-Mischkristalle vorhergesagt, die eine negative thermische Ausdehnung aufweist. Dies wird durch Berechnungen der Schwingungszustandsdichte auf dem Niveau der Dichtefunktionaltheorie (DFT) und mithilfe der harmonischen Näherung (HN) erreicht. Da Berechnungen unter Verwendung der HN die T_t nicht einmal qualitativ vorhersagen können, werden Modellfunktionen für die freie Schwingungsenergie aus DFT-Simulationen zusammen mit einer empirischen Korrektur mithilfe experimentell bestimmter T_t abgeleitet zur Berücksichtigung anharmonischer Effekte, um somit rechenintensive *ab initio*-Simulationen zu vermeiden. Vorhersagen von T_t für jene chemische Zusammensetzungen, die nicht in der Modellableitung enthalten sind, zeigen gute Übereinstimmung mit experimentellen Beobachtungen. Außerdem können die chemischen Zusammensetzungen, bei denen ausschließlich die HT-Phase aus der Glaskristallisation hervorgeht, unter Verwendung des vorgeschlagenen, computergestützten Ansatzes schnell vorhergesagt werden. Zu diesen Zusammensetzungen gehören $Ba_{1-m}Sr_mZn_2Si_2O_7$ Mischkristalle mit m > 0.1. Die thermomechanischen Eigenschaften der HT-Phase von $Ba_{1-m}Sr_mZn_2Si_2O_7$ Mischkristallen in Abhängigkeit der chemischen Zusammensetzung m werden ermittelt und zwar die elastischen Konstanten, Wärmeausdehnung sowie die makroskopischen Grüneisen-Parameter durch die Kombination von DFT-Simulationen mit experimentell bestimmten Gitterparametern. Außerdem wird der Ursprung der negativen thermischen Ausdehnung auf atomaren Niveau für $Ba_{0.5}Sr_{0.5}Zn_2Si_2O_7$ durch Berechnung der mikroskopischen Grüneisen-Parameter mithilfe von DFT Simulationen zusammen mit der quasi-harmonischen Näherung aufgeklärt.

Die zweite Fallstudie ist die Aufklärung der atomaren Struktur und Kristallisation von

nanopartikulärem Fe_2O_3, beginnend mit dem kleinsten Fe_2O_3-Baustein bis zu nanometer-
großen Fe_2O_3-Partikeln. Strukturvorhersagen von kleinen $(Fe_2O_3)_n$ (n = 1-10) Gasphasen-
clustern verwendeten globale Strukturoptimierungen zusammen mit einem zweistufigen Ver-
fahren, welches maßgeschneiderte, *ab initio* parametrisierte, interatomare Potentialunktio-
nen (IP) mit Verfeinerungen auf DFT Niveau kombiniert. Berechnungen für die Kristallisa-
tion von größeren Nanopartikeln bis zu einem Durchmesser von 5 nm verwendeten Molekül-
dynamiksimulationen zusammen mit den maßgeschneiderten IP. Die meisten der $(Fe_2O_3)_n$-
Cluster zeigen kompakte, fast amorphe Strukturen mit geringer oder keiner Symmetrie, mit
Ausnahme der tetraedrischen, Adamantan-ähnlichen $(Fe_2O_3)_2$ Struktur. Größere Gasphasen-
Cluster mit $n>$ 5 nehmen zunehmend tetraedrische Form an, wobei die Adamantan-artige
$(Fe_2O_3)_2$-Einheit das Hauptstrukturmerkmal darstellt. Eine solche tetraedrische Morpholo-
gie bleibt für Fe_2O_3-Nanopartikel mit Durchmessern bis zu 3 nm bestehen. Im Gegen-
satz dazu wurden Einkristalle mit hexagonaler Morphologie durch die simulierte Kristalli-
sation größerer Nanopartikel mit Durchmessern von etwa 5 nm erhalten, was zur Bildung
von ϵ-Fe_2O_3 führte. Die hexagonale Morphologie stimmt hervorragend mit den Ergebnis-
sen überein, die für hergestellte Fe_2O_3-Nanopulver experimentell bestimmt wurden, was die
Zuverlässigkeit des verwendeten Rechenverfahrens bestätigt und den ersten direkten Hin-
weis darauf liefert, dass ϵ-Fe_2O_3 die thermodynamisch stabilste Phase für Nanopartikel dieser
Größe sein kann. Darüber hinaus können die vorhergesagten atomistischen Strukturmodelle
als Ausgangspunkt für zukünftige Simulationen dienen, um einen tieferen Einblick in die ther-
modynamischen und magnetischen Eigenschaften von nanopartikulärem Fe_2O_3 zu erhalten.

Das dritte Fallbeispiel befasst sich mit der Optimierung von polymeren Nanopartikeln
für die effiziente Einkapselung biologisch aktiver Substanzen, u.a. von Wirkstoffen. Hi-
erfür wird die thermodynamische Kompatibilität von Polymeren mit niedermolekularen
Verbindungen mithilfe thermodynamischer Modelle errechnet, die durch atomistische Sim-
ulationen parametrisiert werden. Hier wird ein recheneffizientes Verfahren vorgeschla-
gen, das auf dem Konzept der inhärenten Strukturen (IS) basiert, für die fundierte statis-
tische Erfassung von Polymerkonformationen. Umfassende Testsimulationen bestätigen
die Genauigkeit des verwendeten Simulationsverfahrens zur Berechnung der physikalisch-
chemischen Eigenschaften wie der kohäsiven Energiedichte (CED). Die Berechnung der CED
ermöglicht zusammen mit ihren energetischen Beiträgen die Bestimmung der (Hansen)-
Löslichkeitsparameter, die schnelle qualitative Löslichkeitsvorhersagen in Kombination mit
der Flory-Huggins (FH) Theorie ermöglichen. Die FH-Theorie erlaubt jedoch nicht die Mod-
ellierung spezifischer Wechselwirkungen, wie z. B. Wasserstoffbrücken, obwohl atomistische
Simulationen der Polymermischungen solche Wechselwirkungen explizit berücksichtigen.
Daher wurde die genauere PHSC-Zustandsgleichung nicht nur unter Verwendung der berech-
neten CED, sondern auch mithilfe der Temperaturabhängigkeit des Drucks parametrisiert.
Als Testfall wurden wässrige Polyethylenglykol (PEG)-Lösungen gewählt, von denen bekannt
ist, dass sie starke Wasserstoffbrückenbindungen aufweisen. Die physikalisch-chemischen
Eigenschaften einschließlich des PHSC berechneten Phasendiagramms von PEG-Wasser
zeigen gute Übereinstimmung mit experimentellen Beobachtungen. Daher wird ein zweistu-
figes Verfahren für das effiziente Design von polymeren Wirkstoff-Nanoträgern vorgeschla-
gen. Es kombiniert qualitative Löslichkeitsvorhersagen unter Verwendung der FH-Theorie

für ein schnelles Screening von vielversprechenden Polymeren, die aktive Substanzen effizient lösen, mit rechenintensiveren Simulationen zur Berücksichtigung spezifischer Wechselwirkungen und einer genauen Modellierung der physikalisch-chemischen Eigenschaften durch Parametrisierung der PHSC.

Acknowledgements

Contents

1   **Introduction**

Key prerequisite for the targeted design of novel materials showing a tailored property profile is the profound understanding and control of structure-property relationship. However, in case of, *e.g.*, nanomaterials the experimental elucidation of the atomic structure and properties is a challenging task. In addition, if a vast number of chemical compounds along with their structural modifications comes into question for a certain application, the experimental optimization of the materials properties can be costly and time-consuming. Therefore, driven by increasing computational performance within the past decades, *in silico* methods using computer simulations have considerably gained importance for modeling, prediction and screening of structure and properties of novel materials complementary to experimental characterization [1–3]. In particular, atomistic simulations at the density functional theory (DFT) level as well as simulations using well parameterized interatomic potential functions proved successful for the targeted materials design in various fields applications. These range from the design of active substances in pharmacy [4] through materials for energy generation and storage [5] to materials in optoelectronics [2, 6], chemical catalysis and membrane technology [7].

Starting point of the materials modeling based on atomistic simulations is the determination of suitable structure models. While in some cases (*e.g.*, simple ionic solids) sufficiently accurate structure models can be obtained from experiments, elucidation of the atomic structure of more complex chemical compounds and nanomaterials is very challenging. Therefore, predictions of the atomic structure is of vital importance in such cases requiring computationally efficient methods [1, 8] that make no assumptions regarding the materials structure. With knowledge of the atomic structure, the thermodynamic stability and physico-chemical properties can be calculated as well by employing atomistic simulations [9, 10]. However, if complex structure models or numerous calculations are required for prediction of the materials properties at various operating conditions, sufficiently accurate simulations become computationally too demanding. Hence, lowering the computational costs by approximations is often unavoidable, yet limit the prediction accuracy making the targeted materials design challenging.

Therefore, central aim of this thesis is to facilitate an efficient, *in silico* guided materials design providing good compromise of accuracy and computational effort. For this purpose, computationally efficient methods for prediction of the atomic structure and materials properties are presented. These include multistage procedures employing different approximations including a combination of rapid prescreening calculations with more accurate simulations for property evaluation. In addition, available experimental data facilitate empirical corrections of the models derived for pragmatic and time efficient property predictions.

In this thesis, atomistic simulations combined with thermodynamic modeling are used for elucidation of structure and properties of three distinct types of materials:

(I) Prediction of the phase stability and modeling of anisotropic thermomechanical properties of zero thermal expansion glass ceramics made of $Ba_{1-m}Sr_mZn_{2-2n}Mg_{2n}Si_2O_7$ solid solutions (BZS)

(II) Elucidation of the atomic structure and crystallization of Fe_2O_3 gas phase clusters and nanoparticles

(III) Solubility predictions of active substances in amorphous polymers for optimization of polymeric nanocarriers

The results of (II) were previously published in *Nanoscale* (RSC Publishing) [XI] and parts of this publication are adapted in this thesis. My contribution to this publication was the conduct of atomistic simulations, analysis of the results and draft preparation of the manuscript.

1.1 Computer-aided materials design
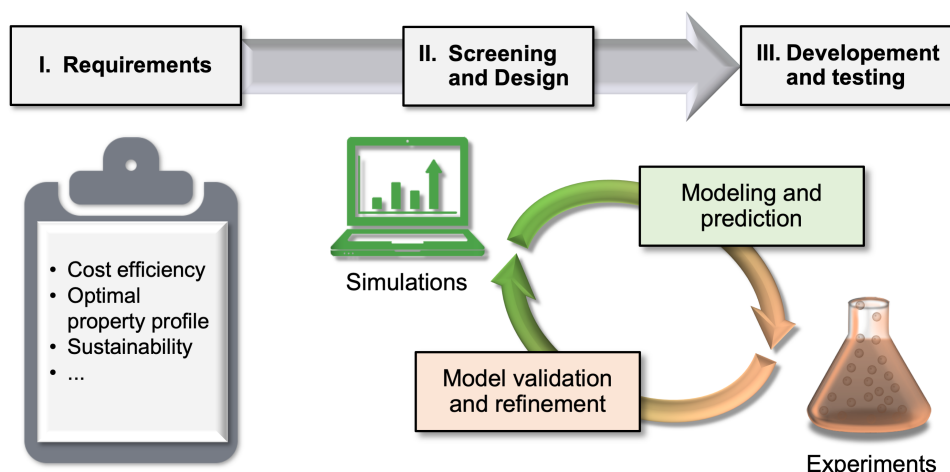
FIGURE 1.1: Stages of the computer-aided design of materials that fulfill predefined requirements in the best possible way [2].

The process of the computer aided - *in silico* - design of novel materials is schematically shown in Figure 1.1 [2]. Starting point of the materials design process is the definition of the requirements on the materials properties, *e.g.,* by using figure of merit. In addition, the demands for sustainable materials (green chemistry) and their cost-effective synthesis as alternative to existing materials considerably increased in the past two decades [11–13]. While previous knowledge and experience such as chemical intuition provides a certain preselection of materials that might fulfill the desired property profile, unexpected chemical compounds and materials structures potentially showing unprecedented properties can only be obtained by trial-and-error approaches. Since such approaches become costly and time consuming by using experiments, the modeling and prediction of materials properties even of hypothetical materials by employing computer simulations provide a promising route for the design

of novel materials. In addition, if numerous materials are already known as potential candidates for a certain application, yet their structure and properties are difficult to characterize, simulations are capable screen the most promising ones.

However, as mentioned above, in case of materials that require complex structure models and predictions for various operating conditions, simulations become computationally very demanding, in particular at the atomic level. Therefore, approximations are indispensable to ensure time efficient design process. However, this limits the accuracy of the predictions rendering the targeted materials design difficult. Thus, the synthesis of at least some prescreened materials and experimental characterization of the properties is essential for validation and refinement of the employed model predictions. Establishing such feedback loop based on synergy between theory and experiments is expected to provide an efficient *in silico* guided design of novel materials. The computational methods presented in this work aim to facilitate such a design process.

1.2 Zero thermal expansion glass ceramics

Zero thermal expansion (ZTE) materials have various applications ranging from commonplace ceramic hobs through telescope mirrors to micromechanical devices [14–16]. Among these materials are glass ceramics containing crystal phases with highly anisotroic thermomechanical properties along with negative thermal expansion (NTE) in at least one crystallographic direction [17]. This applies also to the high temperature (HT) crystal phase of $Ba_{1-m}Sr_mZn_{2-2n}Mg_{2n}Si_{2-o}Ge_oO_7$ solid solutions (BZS) [18, 19]. Figure 1.2 summarizes the change of the phase stability and thermal expansion for wide variety of possible chemical compositions of BZS solid solutions. The pronounced dependence of the coefficient of thermal expansion of the HT BZS phase on the chemical composition allows straightforward tailoring of the thermomechanical properties of the corresponding glass ceramics. However, exploitation of the tunable NTE of the HT BZS phase for technical applications is hampered due to the martensitic phase transition from the low temperature (LT) to the HT phase. This phase transition is connected with a volume change of about 3 vol.% [20]. Thus, such large volume change makes the use of the bulk glass ceramics as ZTE material at operating temperatures close to the phase transition impossible.

Therefore, knowledge of the phase transition temperature T_t is indispensable for the targeted design of BZS glass ceramics. It was shown, that the incorporation of Mg^{2+} and Sr^{2+} into the crystal lattice of $BaZn_2Si_2O_7$ shows strongly opposite effects on T_t [21, 22]. While the substitution of Zn^{2+} with Mg^{2+} in $BaZn_{2-2n}Mg_{2n}Si_2O_7$ increases T_t from about 550 K ($n = 0$) to 1210 K ($n = 1$), [21] the incorporation of Sr^{2+} in $Ba_{1-m}Sr_mZn_2Si_2O_7$ solid solutions T_t considerably decreases down to 473 K even at low Sr^{2+} concentrations of $m = 0.06$ [22]. In addition, the crystallization of glasses with ($m = 0.06$, $n = 0$) yields mixtures of the HT and LT phase. If the Sr^{2+} concentration is further increased ($m > 0.1$), only the HT phase emerges during glass crystallization and, consequently, T_t cannot be determined experimentally. This indicates that the substitution of Ba^{2+} with Sr^{2+} leads to thermodynamic stabilization of the HT phase. Therefore, the incorporation of both, Mg^{2+} and Sr^{2+} into the crystal structure of $BaZn_2Si_2O_7$, is expected to provide a simple way to tune the phase stability of the HT phase as well as T_t over a
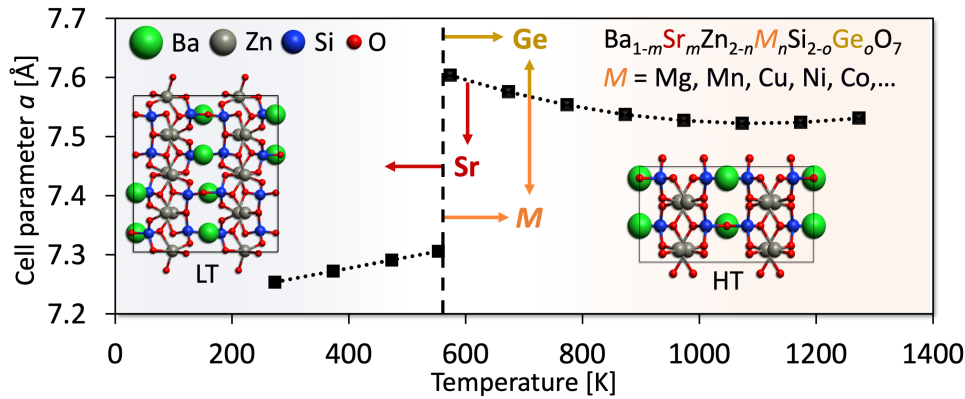
FIGURE 1.2: Change of structure and phase stability of the low (LT) and high temperature (HT) phase of $BaZn_2Si_2O_7$ (black curve) caused by variation of the chemical composition [18, 19].

large temperature range from (theoretical) 0 up to 1200 K. However, the experimental characterization for a high number of possible chemical compositions of $Ba_{1-m}Sr_mZn_{2-2n}Mg_{2n}Si_2O_7$ is a time-consuming task.

For this reason, the prediction of T_t by using atomistic simulations would facilitate the targeted design of these BZS based ZTE glass ceramics. In particular, simulations at the density functional theory (DFT) level proved successful for prediction of polymorphic phase transitions [23, 24]. Predictions of the phase stability of crystalline polymorphs require the calculation of the free energy as a function of temperature. For this, the vibrational density of states (VDOS) and the corresponding vibrational free energy is calculated, *e.g.*, by using the harmonic approximation (HA) [24]. That is, the vibrational frequencies are assumed to be independent of volume and temperature. However, predictions using the HA are limited in accuracy, in particular at elevated temperatures and for materials showing strongly anharmonic lattice vibrations [25]. More accurate, but still qualitative predictions of the phase stability can be achieved by combining DFT simulations with the quasiharmonic approximation (QHA), which takes the volume dependence of the VDOS into account (*e.g.*, Ref. [26]). Quantitative predictions of phase stabilities require the explicit consideration of anharmonicity at a particular temperature by employing *ab initio* molecular dynamics simulations (MD) [27–29]. However, applying *ab initio* MD or phonon calculations using the QHA to a large number of chemical compositions (*cf.* Fig. 1.2) is computationally very demanding.

In order to provide rapid predictions of T_t as a function of chemical composition, simulations at the DFT level for calculation of the VDOS of $Ba_{1-m}Sr_mZn_{2-2n}Mg_{2n}Si_2O_7$ solid solutions are combined with parameterization of composition dependent model functions for the harmonic free energy (*cf.* Chapter 2.2.2). For consideration of anharmonic effects on the temperature dependence of the free energy, an empirical correction is derived using experimentally determined T_t of the solid solution series $Ba_{1-m}Sr_mZn_2Si_2O_7$ ($n = 0$) and $BaZn_{2-2n}Mg_{2n}Si_2O_7$ ($m = 0$). This empirically corrected model is then used for predictions of the phase transition temperatures of $Ba_{1-m}Sr_mZn_{2-2n}Mg_{2n}Si_2O_7$ (m, $n > 0$) solid solutions (Chapter 3.1).

For chemical compositions which lead to a sufficient thermodynamic stabilization of the HT BZS phase, that is, lowering T_t far below operating or even room temperature, the characterization of the anisotropic thermomechanical properties is of fundamental importance. In

particular, the anisotopic thermal expansion is the key factor for the design of the microstructure of such glass ceramics in order to facilitate zero volume expansion of the bulk material. In addition, together with the (anisotropic) elastic properties (stiffness tensor *C*), the thermal expansion has major influence on the residual stresses introduced in the microstructure during fabrication of glass ceramics, which are of vital importance for crack formation in such materials [30].

Therefore, a deeper understanding of both, the anisotropic elastic properties and thermal expansion, is crucial for the targeted design of ZTE glass ceramics. In this context, DFT simulations proved to accurately predict the thermal expansion as well as elastic properties for a variety of materials [10, 31, 32]. In addition, calculations of the VDOS using the QHA and simulations at the DFT level provide insight into the microscopic mechanisms of NTE at the atomic level [33]. Key quantity for characterization of thermal expansion is the Grüneisen parameter that provides the relation between the thermal and mechanical properties of solids [34]. Furthermore, the microscopic Grüneisen parameter describes the volume dependency of the phonon frequencies and its calculation using the QHA allows the elucidation of those vibrational modes that contribute to the NTE. Chapter 3.2 describes the calculation of the anisotropic thermomechanial properties and the Grüneisen parameters at the DFT level for Ba$_{1-m}$Sr$_m$Zn$_2$Si$_2$O$_7$ solid solutions with $m = 0, 0.25, 0.5, 0.75$.

1.3 Magnetic nanopowders: nanoparticulate Fe$_2$O$_3$

Tuning of the thermodynamic stability and properties of crystalline materials cannot only be achieved by variation of the chemical composition as in the case of the glass ceramics introduced in the previous section. For example, nanoparticulate materials show a pronounced size dependence of their atomic structure and properties [35, 36]. Hence, the elucidation how structure and properties change with increasing aggregation state, starting from small clusters through nanoparticles to the bulk material is of fundamental importance for the design of nanomaterials. This issue is addressed for nanoparticulate Fe$_2$O$_3$ in Ref. [XI], previously published in *Nanoscale* (RSC Publishing), and parts of this section are adapted from [XI].

Fe$_2$O$_3$ nanoparticles (NP) find a number of applications due to their unique magnetic, biochemical and catalytic properties [37]. They are used in catalysis, biomedicine for hyperthermia based anticancer therapy and targeted drug delivery, magnetic resonance imaging and immunoassays as well as for magnetic data storage [37–39]. Fe$_2$O$_3$ shows pronounced size dependence of its structural and magnetic properties [40, 41]. As bulk material it exists either as the thermodynamically most stable hematite (α-Fe$_2$O$_3$) or metastable maghemite (γ-Fe$_2$O$_3$), both naturally occurring as minerals. In addition, two Fe$_2$O$_3$ polymorphs are known, β-Fe$_2$O$_3$ and ϵ-Fe$_2$O$_3$ that can only be obtained in nanoparticulate form [40]. ϵ-Fe$_2$O$_3$ has attracted particular attention since the discovery of its unique magnetic and dielectric properties [41] such as the giant coercive field due of the large magneto-crystalline anisotropy and a relatively small saturation magnetization [42]. This makes ϵ-Fe$_2$O$_3$ a promising candidate for advanced materials. Its crystal structure can be described as intermediate between α- and γ-Fe$_2$O$_3$, containing one-quarter of Fe atoms in tetrahedral interstices and three-quarters in octahedral sites. A unique feature ϵ-Fe$_2$O$_3$ is the presence of five-fold coordinated O atoms. It has been suggested [43] that below certain particle size ϵ-Fe$_2$O$_3$ may be thermodynamically the most stable phase.

However, this assumption has not yet been explicitly verified [41]. It addition to the crystalline forms it is also possible to obtain amorphous Fe_2O_3 [40].

Apart from determination of the thermodynamically most stable crystal phase of Fe_2O_3 NP, the elucidation of the atomic structure is one of the key prerequisites for determination and control of, *e.g.*, their magnetic properties. In particular, small iron oxide clusters and Fe_2O_3 NP with diameters between 1-5 nm show strongly size dependent magnetic properties [44]. Furthermore, small nanoclusters can display chemical and physical properties distinct from both small molecules and the corresponding bulk materials or larger NP [45]. However, atomic level characterization of iron oxide nanoclusters is a very challenging task due to its complicated electronic structure. In addition, computational studies of larger clusters are generally hampered by a steeply increasing number of local minima with increasing cluster size [8, 46]. This makes the search for low energy structures by manual construction of all possible isomers followed by local structure optimizations very challenging. Therefore, several global energy minimization techniques for automatic determination of the most stable cluster structure have been proposed [47, 48]. Among them, genetic algorithm (GA) finds the global minimum structure by an evolutionary process [46, 48, 49] and has been applied successfully for structure predictions of various metal oxide nanoclusters (see, *e.g.*, Ref. [8]).

Due to these difficulties computational studies of iron oxide clusters have so far been limited to small non-stoichiometric ionic [50–56] and neutral species [57, 58]. Stoichiometric, neutral $(Fe_2O_3)_n$ clusters were investigated up to $n = 2$ [59–61] as well as for $n = 2$-6 and 10 [62] using only manually constructed and locally optimized structures. A previous study [XII] reported the first global structure optimization of $(Fe_2O_3)_n$ clusters with $n = 1$-5 employing density functional theory (DFT) and including precise determination of their magnetic (spin) states. It was demonstrated that the geometric structure of larger $(Fe_2O_3)_n$ clusters is virtually independent of their magnetic configurations. In addition, starting from $n = 4$ the precise spin state has only a minor influence on relative energies of different cluster isomers.

The steep increase of computational cost of global structure optimization algorithms makes search for global energy minima of larger clusters and nanoparticles virtually impossible. Even if the global minimum of a large system could eventually be located the large number of very close-lying local minima renders the result meaningless. Instead, low-energy structures can be located employing molecular dynamics (MD) simulations along with carefully parameterized interatomic potential functions (IP) [46, 63]. As an example, the simulated annealing procedure was employed to investigate the crystallization process and structure of metal oxide NP with several nm in diameter [64–66]. However, similar studies of Fe_2O_3 NP with diameters in the range of 2-5 nm lead only to amorphous structures,[67] most probably due to short simulation times and shortcomings of the potential functions employed. Despite the unique properties, technological relevance and complex polymorphous transformations of crystalline $(Fe_2O_3)_n$ NP no computational investigations of their structure and crystallization processes have been reported before.

The first systematic, comprehensive study of nanoparticulate Fe_2O_3 starting from its smallest Fe_2O_3 building unit and $(Fe_2O_3)_n$ clusters of increasing size through to nanometer-sized Fe_2O_3 particles is presented in Chapter 4. This is achieved by employing tailored, *ab initio* parameterized interatomic potential functions [68] (IP-Fe_2O_3) combined with a refinement at the DFT level (*cf.* Chapter 2.2.3) to locate global energy minima of $(Fe_2O_3)_n$ clusters with $n =$

1-10. Finally, the IP-Fe$_2$O$_3$ are used for simulated crystallization of Fe$_2$O$_3$ NP with diameters up to 5 nm.

1.4 Solubility optimization of actives in polymeric nanocarriers

Solubility of low molecular weight compounds, such as solvents, dyes or other active substances in polymers is of fundamental importance for numerous industrial applications ranging from membrane separations through solvent extraction to thin film coating [69]. In particular, the optimization of polymeric nanocarriers for the efficient encapsulation of biologically active substances plays a crucial role in nanomedicine, *e.g.*, for targeted delivery of anticancer therapeutics [70] or tumor imaging agents [71]. However, experimental optimization of the encapsulation efficiency (EE) by adjustment of the polymer structure and chemical composition using trial-and-error approaches is costly and time-consuming. Therefore, solubility predictions by employing thermodynamic modeling of polymer mixtures are a powerful tool in the process of discovery and optimization of new drug delivery systems [72].
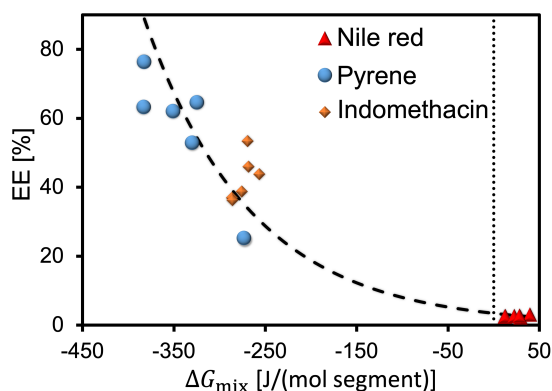
FIGURE 1.3: Encapsulation efficiency (EE) of actives in PEG-PLA copolymer nanoparticles as a function of predicted free energies of mixing ΔG_{mix} [X].

For this purpose, atomistic simulations proved successful for predictions of the thermodynamic drug-polymer compatibility and beyond that provide also a detailed understanding of the intermolecular interactions between polymers and active substances (*e.g.*, refs. [X] and [73–75]). Key quantity for determination of the intermolecular interactions is the Hildebrand solubility parameter (SP) of polymer and active, respectively, defined as the square root of the cohesive energy density (CED) [76, 77]. In most theoretical studies, the CED are used for parameterization of the Flory-Huggins (FH) theory [78, 79] yielding the free energy of mixing as measure for the thermodynamic compatibility between polymer and active substances. Figure 1.3 depicts the successful correlation of predicted free energies of mixing and experimentally observed EE of different actives in copolymer nanoparticles comprising different ratios of polyethylene glycol (PEG) and polylactic acid (PLA) [X]. In addition, an extension of the SP approach was proposed by Hansen [80] that uses a separation of the CED into different energetic contributions such as dispersion and hydrogen bonding interactions. This facilitates a more detailed characterization of the intermolecular interactions, which can be potentially used for rapid screening of the thermodynamic polymer-active compatibility. For example, a machine learning approach was recently proposed for calculation of Hansen SP in order to provide a versatile tool for polymer solubility predictions [81].

Although atomistic simulations combined with the FH theory provided solubility predictions in agreement with experimental observations in several cases [73–75], the general applicability of this approach was under debate recently [82–84]. Employing the FH theory parameterized from atomistic simulations contradicting results were obtained in comparison with experimental data for several polymer-active mixtures [83] clearly indicating the limited accuracy of such solubility predictions. This is connected with two major factors that determine accuracy and reliability of the the thermodynamic modeling.

The first challenge is the atomistic modeling of bulk amorphous materials using structure models with periodic boundary conditions which inherently assume long-range order. Thus, generation and sampling of a sufficiently large number of polymer conformations is indispensable for an accurate atomistic modeling of amorphous polymers. Some theoretical studies employed molecular dynamics (MD) simulations with long equilibration times up to microseconds for relaxation of the polymer conformations [84, 85]. On the other hand, configurational biased Monte-Carlo (MC) algorithms [86, 87] were applied for generation of polymer conformations, which were subsequently used for the sampling of the CED (*cf.* refs. [73] and [X]) by employing comparatively short MD simulations in the ns scale. However, the accuracy and reproducibility of the latter sampling approach for calculation of the CED has not yet been critically evaluated.

Another computational method for calculation of the atomic structure and thermodynamic quantities of amorphous materials employs the concept of so called inherent structures (IS) initially proposed by Stillinger and Weber [88–90]. It is based on the separation of the $3N$-dimensional potential energy surface (PES) and the corresponding partition function into non-overlapping basins for a system containing N atoms [89]. The IS represent these basins, which can be calculated by applying geometry optimizations to MD trajectories of the equilibrated liquid state at temperatures above the glass transition temperature T_g. The resulting distribution of the IS potential energy minima corresponds to the probability distribution that a structure extracted from the liquid state is associated with the IS and their corresponding properties [91, 92]. Consequently, not only atomic structures but also thermodynamic quantities of glass forming liquids at temperatures close to T_g can be calculated [92]. Simulations employing the concept of IS were used for elucidation of the structure and properties of various amorphous materials including polymers and biomolecules [90, 93–95]. However, to the best of the author's knowledge this methodology has not yet applied to polymer solubility predictions.

The second key factor for accurate thermodynamic description of polymer solutions is the model parameterized from the simulation results. While atomistic simulations are capable to describe the intermolecular interactions including specific interactions such as hydrogen bonding, mean-field lattice theories such as the FH theory fail to model such interactions [82, 83]. For example, the FH theory is based on the regular solution theory assuming positive entropy of mixing of the ideal lattice. However, several strongly hydrogen bonding solutions such as alcohol water mixtures [96] are known to show negative entropy of mixing due to the formation clusters in solution [97]. This applies also to aqueous solutions of polyethylene glycol (PEG) [98] and PEG drug mixtures [99] showing pronounced hydrogen bonding. Therefore, it was pointed out in ref. [82] that more sophisticated equation of state (EOS) theories are required for reliable predictions of polymer-drug compatibility. Among the numerous EOS theories for polymers [100] are the statistical associating fluid theory (SAFT) [101, 102] and the

perturbed hard sphere chain (PHSC) EOS [103–105]. Most frequently the parameters of these EOS were obtained by using experimentally determined pressure temperature dependencies and phase diagrams. Despite also few examples for the derivation of EOS parameters for polymers by employing atomistic simulations were reported [106, 107] the critical evaluation of the accuracy of the solubility predictions using such a parameterization, in particular for mixtures showing pronounced hydrogen bonding is still lacking.

Chapter 5 focusses on both of the named factors, the accuracy of atomistic simulations for the statistical sampling of the polymer conformations as well as the thermodynamic modeling. First, a simulation procedure is proposed combining MC simulations for generation of polymer structure models with relatively short MD simulations for the sampling of inherent structures. Comprehensive test simulations of the simulation procedure are performed in order to facilitate accurate and reproducible statistical sampling of polymer conformations and the related physico-chemical properties such as CED and pressures. Subsequently, the simulation results are used for parameterization of the FH theory including a correction that considers the change of the intermolecular structure as a function of the composition. In addition, the concept of Hansen solubility parameters is applied for rapid qualitative solubility predictions. Finally, the parameters of the PHSC EOS are derived from atomistic simulations for calculation of the physico-chemical properties of aqueous PEG solutions as test case for strongly hydrogen bonding polymer mixtures.

2   Theory and computational methods

2.1   Modeling of materials properties

2.1.1   Statistical thermodynamics

Predictions of the thermodynamic stability and physico-chemical properties of materials employing atomistic simulations requires the link of calculated microscopic, atomistic states and the macroscopic, observable states and properties. The methods used in this work are based on classical statistical thermodynamics with basic concepts introduced in this section.

Central quantity linking microscopic states and macroscopic, thermodynamic quantities is the canonical partition function Q. For a particular atomic configuration κ, the canonical partition function Q_κ reads [108, 109]:

$$Q_\kappa = \sum_i \exp(-\beta E_i), \tag{2.1}$$

with the energy E_i of microstate i and $\beta = (kT)^{-1}$, where k is the Boltzmann constant and T the temperature. In general, the probability P_i of finding a microstate in the macroscopic system which is in thermal equilibrium with its surrounding (*e.g.*, a heat bath) is given by the Boltzmann distribution [109]:

$$P_i = \frac{1}{Q_\kappa} \exp\left(-\beta E_i\right). \tag{2.2}$$

The partition function can be separated into sums of states of, *e.g.*, i electronic and j vibrational states. This allows (in case of solids) the factorization of Q_κ such that $Q_\kappa = q_{\kappa,\text{el}} q_{\kappa,\text{vib}}$ with the electronic $q_{\kappa,\text{el}} = \sum_i \exp(-\beta E_{i\kappa,\text{el}})$ and vibrational partition function $q_{\kappa,\text{vib}} = \sum_j \exp(-\beta E_{j\kappa,\text{vib}})$ [110]. For molecular systems also the translational and rotational partition functions have to be considered. Since only non-metallic materials are considered in this work, the thermal excitation of higher lying electronic states above the ground state with $E_{0\kappa} = E_{0\kappa,\text{el}}$, which is relevant for the modeling of, *e.g.*, metallic materials (electron gas), is neglected. In other words, the probability of finding configuration κ in an electronic state with $E_{i\kappa,\text{el}} > E_{0\kappa}$ is negligibly small and, consequently, $q_{\kappa,\text{el}} \approx \exp(-\beta E_{0\kappa})$. The vibrational partition function $q_{\kappa,\text{vib}}$ considers atomic displacements around configuration κ by calculating the force constants and vibrational frequencies, *e.g.*, by using phonon calculations along with the harmonic approximation (*cf.* Section 2.2). With knowledge of Q_κ or a reasonable approximation of it, respectively, the Helmholtz free energy A_κ is given as [108]:

$$A_\kappa = -kT \ln(Q_\kappa). \tag{2.3}$$

The factorization of Q_κ implies that A_κ can be separated into additive contributions and written as [10, 111]:

$$A_\kappa(T) = E_{0\kappa} + E_{ZPE} + A_{\kappa,vib}(T), \tag{2.4}$$

with the zero-point vibrational energy $E_{\kappa,ZPE}$ and the temperature dependent vibrational free energy $A_{\kappa,vib}(T) = E_{\kappa,vib}(T) - TS_{\kappa,vib}(T)$. Up to now, only the partition function Q_κ and free energy A_κ for one particular atomic configuration κ, that is one point on the potential energy surface (*cf.* Section 2.2.1) was considered. However, in case of disordered solids, for example substitutional solid solutions or amorphous materials, accurate thermodynamic modeling requires consideration of numerous atomic configurations κ for calculation of the partition function $Q = \sum_\kappa Q_\kappa$ [111, 112]. The corresponding Helmholtz free energy $A(T)$ as a function of temperature T is (equivalent to eq 2.3):

$$A(T) = -kT \ln\left(\sum_\kappa \exp(-\beta A_\kappa)\right). \tag{2.5}$$

Assuming that the vibrational free energy is independent of the atomic configuration κ, that is $A_{\kappa,vib} = A_{vib}$, eq 2.5 reads:

$$A(T) = -kT \ln\left(\sum_\kappa \exp(-\beta E_{0\kappa})\right) + E_{ZPE} + A_{vib}(T). \tag{2.6}$$

Similar to eq 2.2, the probability of the presence of an atomic configuration in the macroscopic system, which is in thermal equilibrium with its surrounding, is given by the Boltzmann distribution [112]:

$$P_\kappa = \frac{1}{Q} \exp(-\beta E_{0\kappa}). \tag{2.7}$$

With knowledge of the energies $E_{0\kappa}$ of all possible configurations κ (or a representative set of configurations) allows the calculation of (an approximated) Q and the average properties $\overline{Y} = \sum_\kappa P_\kappa Y_\kappa$ using the quantities Y_κ of each configuration. For example, for the average energy $\overline{E_0}$ of the electronic ground state applies [112]:

$$\overline{E_0} = \sum_\kappa P_\kappa E_{0\kappa}. \tag{2.8}$$

In addition, the configurational entropy S_{conf} can be calculated using:

$$S_{conf} = -k \sum_\kappa P_\kappa \ln P_\kappa. \tag{2.9}$$

Employing eqs 2.7-2.9 one can rewrite eq 2.6 to yield the expression for $A(T)$, which is used as starting point for modeling phase stability of bulk polymorphs in Chapter 3:

$$A(T) = \overline{E_0} - TS_{conf} + E_{ZPE} + A_{vib}(T). \tag{2.10}$$

This work mainly focusses on the thermodynamic modeling of incompressible phases, that is only small volume changes dV have to be considered. Therefore, the volume work pdV

is negligibly small at moderate pressures p (< 10 MPa) such that the Helmholtz free energy A provides reasonable approximation to the Gibbs energy $G = A + pV$.

Using standard thermodynamic relations one directly obtains the pressure p from the Helmholtz free energy A by using [34, 108]:

$$p = -\left(\frac{\partial A}{\partial V}\right)_T.$$
(2.11)

This relation is of particular importance, since it provides the relation of the observable pressure and the free energy. Obviously, the latter can be calculated by integration of $p(V)$ with respect to the volume at a particular temperature. Therefore, knowledge of the pressure as a function of volume and temperature - obtained either by experiments or simulations - facilitates derivation of thermodynamic models by parameterization of pressure explicit equation of states (EOS) $p = p(T, V)$. Such EOS are frequently expressed by using the dimensionless compressibility factor Z:

$$Z = \frac{p}{\rho kT},$$
(2.12)

along with the number density $\rho = NV^{-1}$ (N - number of particles). In case of the ideal gas the compressibility factor is simply $Z_{\text{id}} = 1$. Many EOS use corrections to Z_{id} for modeling of real gases and liquids in form of the Virial EOS [108]:

$$Z = 1 + \rho B_2(T),$$
(2.13)

where $B_2(T)$ is the second Virial coefficient considering particle pair correlations and interactions. For example, one of the simplest expressions for Z and $B_2(T)$, respectively, is the van der Waals (vdw) EOS for which $B_2(T)$ reads:

$$B_2(T) = b - \frac{a_{\text{vdw}}}{kT}.$$
(2.14)

The vdw EOS considers the excluded volume of two gas particles in contact using the co-volume b as well as attractive (non-bonding) particle pair interactions by the van der Waals perturbation parameter a_{vdw}. More sophisticated approximations for $B_2(T)$ will be introduced in Section 2.1.4 for the thermodynamic modeling of amorphous polymers. In contrast to the EOS for modeling of gases and liquids, EOS for (crystalline) solids such as the Vinet [113, 114] or Birch-Murnaghan EOS [115, 116] are not based on the Virial EOS. They rather describe the volume dependence of p for isotropic solids by using the bulk modulus K as well as its pressure and in some cases also its temperature dependence [25].

Apart from modeling of the free energy, knowledge of the $p - V - T$ relation, *e.g.*, provided by an EOS, allows in principle the calculation of all thermodynamic quantities. In this work, the isochoric thermal pressure coefficient - a measure for the thermally induced pressure at constant volume - is of particular relevance [34, 117, 118]:

$$\left(\frac{\partial p}{\partial T}\right)_V = \alpha K = \gamma \frac{C_V}{V} = \frac{p_{\text{int}} + p}{T}.$$
(2.15)

It provides the link between the thermomechanical properties, namely the thermal expansion α and bulk modulus K, and the ratio of heat capacity C_V to the volume along with the dimensionless (macroscopic) Grüneisen parameter γ. The latter is connected with the vibrational states of solids by the microscopic Grüneisen parameters that quantify the volume dependence of vibrational frequencies. Since C_V, V and K are positive, negative thermal expansion α is related to negative γ and, therefore, the Grüneisen parameter is of central importance for modeling zero thermal expansion materials (*cf.* Section 2.1.3). In addition, the isochoric thermal pressure coefficient is related to the internal pressure p_{int} that equals the partial derivative of the internal (potential) energy with respect to volume at constant temperature [118–120]. This relation allows the calculation of the (residual) energy from pressure explicit EOS used for the thermodynamic modeling of polymers in Section 2.1.4.

2.1.2 Phase stability of bulk polymorphs

Starting point for modeling the phase stability and the phase transition temperature T_{t} of $\text{Ba}_{1-m}\text{Sr}_m\text{Zn}_2\text{Si}_2\text{O}_7$ (BZS) solid solutions is the Helmholtz free energy $A(T)$ as a function of temperature T given in eq 2.10. In this section, model functions for $A(T)$ as a function of the chemical composition (m, n) are derived for prediction of T_{t} by combining simulations at the density functional theory (DFT) level and experimentally observed T_{t}.

Fundamental condition for the transition from the low (LT) to the high temperature (HT) phase at temperature T_{t} is $\Delta A(T_{\text{t}}) = A_{\text{HT}}(T_{\text{t}}) - A_{\text{LT}}(T_{\text{t}}) = 0$. Accordingly, relevant quantities for modeling of the phase stability are the changes of configuration entropy ΔS_{conf} (*cf.* eq 2.9), average lattice energy $\Delta \overline{E_0}$ at 0 K (*cf.* eq 2.8), zero-point vibrational energy ΔE_{ZPE} as well as the temperature dependent vibrational free energy $\Delta A_{\text{vib}}(T)$. Since the accurate calculation of $\Delta \overline{E_0}$ and ΔS_{conf} requires a large set of DFT calculations of all possible atomic configurations for substitution of Ba^{2+} with Sr^{2+} and Zn^{2+} with Mg^{2+}, it is assumed in the following that $\Delta \overline{E_0}$ is well approximated by ΔE_0 of the lowest energy structures obtained (*cf.* Section 2.2.2). Furthermore, it is assumed that the free energy contributions $-T\Delta S_{\text{conf}}$ to $\Delta A(T)$ are negligibly small (*cf.* Section 3.1).

Figure 2.1a shows the Helmholtz free energy $A(T)$ as a function of temperature for $\text{BaZn}_2\text{Si}_2\text{O}_7$ (BaZn) and $\text{BaMg}_2\text{Si}_2\text{O}_7$ (BaMg). If the vibrational free energy $\Delta A_{\text{vib}}(T)$ depends only slightly on the chemical composition, the relative energy at 0 K of the of the HT phase with respect to the LT phase $\Delta E_{0\text{K}} = \Delta E_0 + \Delta E_{\text{ZPE}}$ is the most determining factor for prediction T_{t} as a function of the chemical composition. Therefore, it is expected that the relative lattice energies $E_{0\text{K}}$ correlate with T_{t}. For this purpose, the relative lattice energies ΔE_0 calculated using DFT simulations at several compositions (m, n) (*cf.* Section 2.2.2) were fitted to a quartic polynomial, in order to obtain a continuous functional dependence for ΔE_0 on (m, n). Similarly, a composition dependent model for the vibrational free energy $A_{\text{vib}}(T)$ is derived by using DFT simulations for different (m, n) along with the harmonic approximation (HA) that frequently provides reasonable results at low temperatures [25]. However, at elevated temperatures the inclusion of anharmonic effects is indispensable for accurate thermodynamic modeling [27] of phase transitions (Figure 2.1b), yet requires computationally demanding simulations making predictions for numerous chemical compositions tremendously challenging. Therefore, an empirical correction is applied to the vibrational free energy $A_{\text{vib,HT}}(T)$ of the
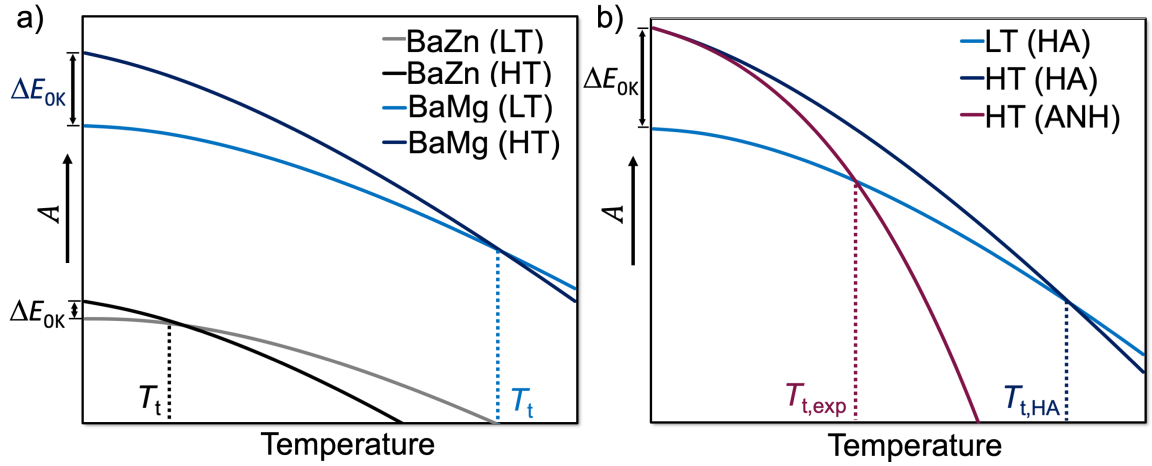
FIGURE 2.1: Helmholtz free energy A as a function of temperature for prediction of phase transition temperature T_t. a) Free energies for $BaZn_2Si_2O_7$ (BaZn) and $BaMg_2Si_2O_7$ (BaMg) along with their relative energies of the high (HT) with respect to the low temperature (LT) phase at 0 K, ΔE_{0K}. b) Empirical correction of the harmonic (HA) free energy of the HT phase (yielding $T_{t,HA}$) using experimentally observed transition temperatures $T_{t,exp}$ for consideration of anharmonic (ANH) effects.

HT phase using available, experimentally determined T_t for $Ba_{1-m}Sr_mZn_2Si_2O_7$ ($n = 0$) and $BaZn_{2-2n}Mg_{2n}Si_2O_7$ solid solutions ($m = 0$) as depicted in 2.1b.

In general, $A_{vib}(T)$ can be calculated from the vibrational entropy S_{vib} using [25, 121]:

$$A_{vib}(T) = -\int_0^T S_{vib}\left(T'\right)dT'. \tag{2.16}$$

Together with the vibrational density of states (VDOS) $g(v)$, S_{vib} of a solid can be calculated using the vibrational entropy of a single harmonic oscillator (Einstein model) and the [25, 121, 122]:

$$S_{vib}(T) = k \int_0^{v_{max}} \left(\frac{u}{\exp(u) - 1} - \ln(1 - \exp(-u))\right) g(v)dv, \tag{2.17}$$

with $u = \beta h v$, the vibrational frequencies v and the Planck constant h. First, the harmonic Debye model for anisotropic solids is applied to find an approximation for $g(v)$ using three different Debye temperatures θ_{i0} [123]:

$$g(v) = 9N \sum_{i=1}^{3} \left(\frac{h}{k\theta_{i0}}\right)^3 v^2. \tag{2.18}$$

Next, a linear dependence of the Debye temperatures $\theta_{i0}(m, n)$ on the chemical composition (m, n) is assumed for both, the LT and the HT phase:

$$\theta_{i0}(m, n) = \Theta_{BaZn,i} + \Theta_1 m + \Theta_2 n. \tag{2.19}$$

The parameters $\Theta_{BaZn,i}$, Θ_1, Θ_2 are fitted to the harmonic vibrational free energies and zero-point vibrational energies calculated for different (m, n) by using phonon calculations at the

DFT level described more detailed in Section 2.2.2. In the HA θ_{i0} and, consequently, the VDOS is independent of T and V. A correction of S_{vib} for consideration of anharmonic effects can be obtained introducing temperature dependent vibrational frequencies, that is, defining a temperature dependent $\theta_i(T)$ [25, 117, 121, 122] using $\theta_{i0}(m, n)$ of the harmonic VDOS:

$$\theta_i(T) = \theta_{i0}(m, n) \exp\left(\tau_{\mathrm{anh}} T\right). \tag{2.20}$$

Similar to $\theta_{i0}(m, n)$, the quantity τ_{anh} is assumed to be linearly dependent on the chemical composition. As mentioned above, this correction is applied to the vibrational free energy of the HT phase by fitting $\Delta A(T_t) = 0$ to experimentally observed phase transition temperature T_t of $\mathrm{Ba_{1-m}Sr_mZn_2Si_2O_7}$ ($n = 0$) and $\mathrm{BaZn_{2-2n}Mg_{2n}Si_2O_7}$ ($m = 0$) solid solution series (*cf.* Fig. 2.1):

$$\tau_{\mathrm{anh}}(m, n) = \tau_{\mathrm{BaZn}} + \tau_1 m + \tau_2 n, \tag{2.21}$$

where τ_{BaZn}, τ_1 and τ_2 are adjustable parameters. Assuming that the vibrational free energy continuously changes with varying chemical composition, the composition dependent model VDOS in eqs 2.18-2.20 can be used for predictions of T_t for the complete composition range of $\mathrm{Ba_{1-m}Sr_mZn_{2-2n}Mg_{2n}Si_2O_7}$ solid solutions.

2.1.3 Anisotropic thermomechanical properties

For BZS glass ceramics with chemical composition that show T_t suitable for application of as zero thermal expansion materials, characterization of the thermomechanical properties, in particular of the thermal expansion α as well as the elastic properties is of fundamental importance. In general, for an isotropic solid α is related to the bulk modulus K, heat capacity C_V, volume V and macroscopic Grüneisen parameter γ as given in eq 2.15. Since the HT phase of BZS solid solutions shows an orthorhombic crystal structure, anisotropic thermal expansion $\boldsymbol{\alpha} = (\alpha_a, \alpha_b, \alpha_c)^{\mathrm{T}}$ for each crystallographic axis a, b, c is considered here. Together with the three corresponding Grüneisen parameters $\boldsymbol{\gamma} = (\gamma_a, \gamma_b, \gamma_c)^{\mathrm{T}}$ and the (3×3) compliance tensor $\mathbf{S} = \mathbf{C}^{-1}$, which is inverse of the stiffness tensor $\mathbf{C}$, and neglecting shearing of the unit cell, eq 2.15 reads [117]:

$$\boldsymbol{\alpha} = \frac{V}{C_V}\mathbf{S}\boldsymbol{\gamma}. \tag{2.22}$$

Here, C_V and $\mathbf{S}$ are calculated by employing DFT simulations (*cf.* Section 2.2.2) and $\boldsymbol{\gamma}$ is obtained by fitting $\boldsymbol{\alpha}$ to experimentally observed as well as DFT calculated cell parameters of the HT phase for $\mathrm{Ba_{1-m}Sr_mZn_2Si_2O_7}$ solid solutions with $m = 0$, 0.25, 0.5 and 0.75. For this purpose, the three adjustable parameters $\gamma_a, \gamma_b, \gamma_c$ and the compliance tensor $\mathbf{S}$ are assumed to be independent of temperature. In addition, by using the DFT calculated $\mathbf{C}$ and $\mathbf{S}$, elastic properties such as bulk modulus K and the linear Young's modulus Y_i along every crystallographic direction $i = a, b, c$ can be obtained [124]. Similarly, the linear compressibilities for each crystallographic direction [25, 125] are calculated with:

$$b_i = \sum_j S_{ij}. \tag{2.23}$$

The average (volumetric) Grüneisen parameter $\overline{\gamma}$, which is also assumed to be independent of temperature, provides the relation between the volumetric thermal expansion α, K and C_V (*cf.* eqn. 2.15) and reads [125]

$$\overline{\gamma} = \frac{b_a \gamma_a + b_b \gamma_b + b_z \gamma_c}{b_a + b_b + b_c}. \tag{2.24}$$

On the other hand, for elucidation of the microscopic origin of the (negative) thermal expansion at the atomic level, the microscopic Grüneisen parameters $\gamma_{\mathbf{k}i}$ for phonon branch i and reciprocal lattice vector $\mathbf{k}$ can be calculated using phonon calculations (*cf.* Section 2.2.2) along with the quasi-harmonic approximation (QHA). They quantify the volume dependence of the vibrational frequencies $\nu_{\mathbf{k}i}$ defined as [25, 117, 125, 126]:

$$\gamma_{\mathbf{k}i} = -\frac{V}{\nu_{\mathbf{k}i}} \frac{\partial \nu_{\mathbf{k}i}}{\partial V}. \tag{2.25}$$

In addition, the DFT calculated $\gamma_{\mathbf{k}i}$ allow the determination of the temperature dependent, macroscopic Grüneisen parameter γ_{DFT} by using [126]:

$$\gamma_{\mathrm{DFT}} = \sum_{\mathbf{k}i} \frac{C_{\mathbf{k}i} \gamma_{\mathbf{k}i}}{C_V}, \tag{2.26}$$

along with the contribution $C_{\mathbf{k}i}$ of each vibrational mode $\mathbf{k}i$ at k-point $\mathbf{k}$ for phonon branch i to the heat capacity $C_V = \sum_{\mathbf{k}i} C_{\mathbf{k}i}$:

$$C_{\mathbf{k}i} = k u^2 \exp(u) (\exp(u) - 1)^{-2}, \tag{2.27}$$

with $u = \beta h \nu_{\mathbf{k}i}$.

2.1.4 Thermodynamic modeling of polymer solubility

The calculation of the thermodynamic driving force for formation of polymer-active mixtures is of vital importance for prediction of the solubility of a low molecular weight compounds (here: solvents) in polymeric nanocarriers. For this purpose, the molar Gibbs energy of mixing Δg_{mix} is the central quantity for determination of the thermodynamic compatibility between the two compounds and, thus, provides a measure how the encapsulation efficiency changes with varying hydrophobicity of the polymer (*cf.* Section 1.4). Here, thermodynamic models are derived from atomistic simulations (*cf.* Section 2.2.4), whereby the cohesive energy density (CED) c_i of component i as well as the pressure as a function of temperature is of central importance. Moreover, the CED is connected with the frequently used Hildebrand solubility parameter δ_i through the relation $c_i = \delta_i^2$ [76, 77]. Please note that every quantity with the indices $i = j = 1$ refers to a polymer (PEG and PLA) whereas for solvents $i = j = 2$ is used in the following.

The CED or the Hildebrand solubility parameter (SP), respectively, which quantify the intermolecular interactions, are connected with the potential energy per particle (segment or molecular unit) e_i through the molar volume $v_i = V N_{\mathrm{s}}^{-1}$ (N_{s} number of segments) by the relation $e_i = -v_i \delta_i^2 = -v_i c_i$ for pure polymers or solvents. In case of mixtures showing the average molar volume $v_m = \sum_i x_i v_i$ and cohesive energy density c_m, the potential energy per segment is $e_m = -v_m c_m$ (or $e_m = -v_m \delta_{\mathrm{m}}^2$). In general, the intermolecular structure and interactions of

liquids or amorphous solids are characterized by the radial distribution function (RDF) $g_{ij}(R)$ and the segment pair potential $\phi_{ij}(R)$. The potential or residual energy with respect to the pure ideal gases e reads [127]:

$$e = \frac{\rho_s}{2} \sum_{i=1}^{l} \sum_{j=1}^{l} x_i x_j \int_0^{R_1} \phi_{ij}(R) \, 4\pi R^2 g_{ij}(R) dR, \tag{2.28}$$

for a system containing l different components with mole fractions x_i, the segment density ρ_s (inverse of v_i) and the center-to-center distance R of two segments with cutoff distance R_1. With knowledge of e_i and e_m, the molar energy of mixing per segment can be calculated with:

$$\Delta e_{\text{mix}} = e_m - x_1 e_1 - x_2 e_2. \tag{2.29}$$

Since the volume change of mixing is small the molar enthalpy of mixing Δh_{mix} is well approximated by Δe_{mix} at moderate pressures considered here. The method for parameterization of the intermolecular pair potential $\phi_{ij}(R)$ by employing atomistic simulations is shown in Figure 2.2. Stating from atomistic model of polymers, active substances and the corresponding mixtures, a coarse graining procedure is applied (implemented in the *Materials Studio* program suite, Version 17.1, Dassault Systèmes BIOVIA) for definition of molecular units. Please note that in case of atomistic and coarse grained models obtained from simulations the term *unit* is used, which refers to a polymer repeating unit or a single solvent/active molecule, while *segment* is used for an arbitrarily defined molecular fragment of the thermodynamic models described below. Nonetheless, the relations described in this section apply to both, molecular units and segments. Next, the intermolecular RDFs of the coarse grained models are calculated. Together with the CED obtained from atomistic simulations, $\phi_{ij}(R)$ can be calculated by assuming a square-well potential (SW) since it contains only one adjustable parameter, the intermolecular interaction energy ω_{ij} (Fig. 2.2b). The SW potential reads:

$$\phi_{ij}(R) = \begin{cases} \infty, & R < R_0 \\ \omega_{ij}, & R_0 \le R \le R_1 \\ 0, & R > R_1, \end{cases} \tag{2.30}$$

along with the the parameters R_0 defined as the onset of the RDF and R_1 chosen as diameter of a sphere with volume v_i (center-to-center distance of two particles). Such a pair potential can be used for thermodynamic modeling of polymer mixtures using the Flory-Huggins (FH) theory described in the next section. In addition, a composition dependent correction of the FH theory (FH$_z$) is applied for consideration of unequal sized segments (Fig. 2.2c).

A more accurate modeling of the intermolecular pair potential can be achieved using the Lennard-Jones (LJ) potential with potential well depth ε that is used for parameterization of the perturbed hard sphere chain (PHSC) equation of state (EOS) [103–105]:

$$\phi_{ij}(r) = \varepsilon_{ij} \left(\left(\frac{\sigma_{ij}}{R} \right)^{12} - 2 \left(\frac{\sigma_{ij}}{R} \right)^6 \right). \tag{2.31}$$

Due to the additional parameter σ quantifying the equilibrium (center-to-center) distance of two units, a second relation is required for parameterization of the LJ potential. For this
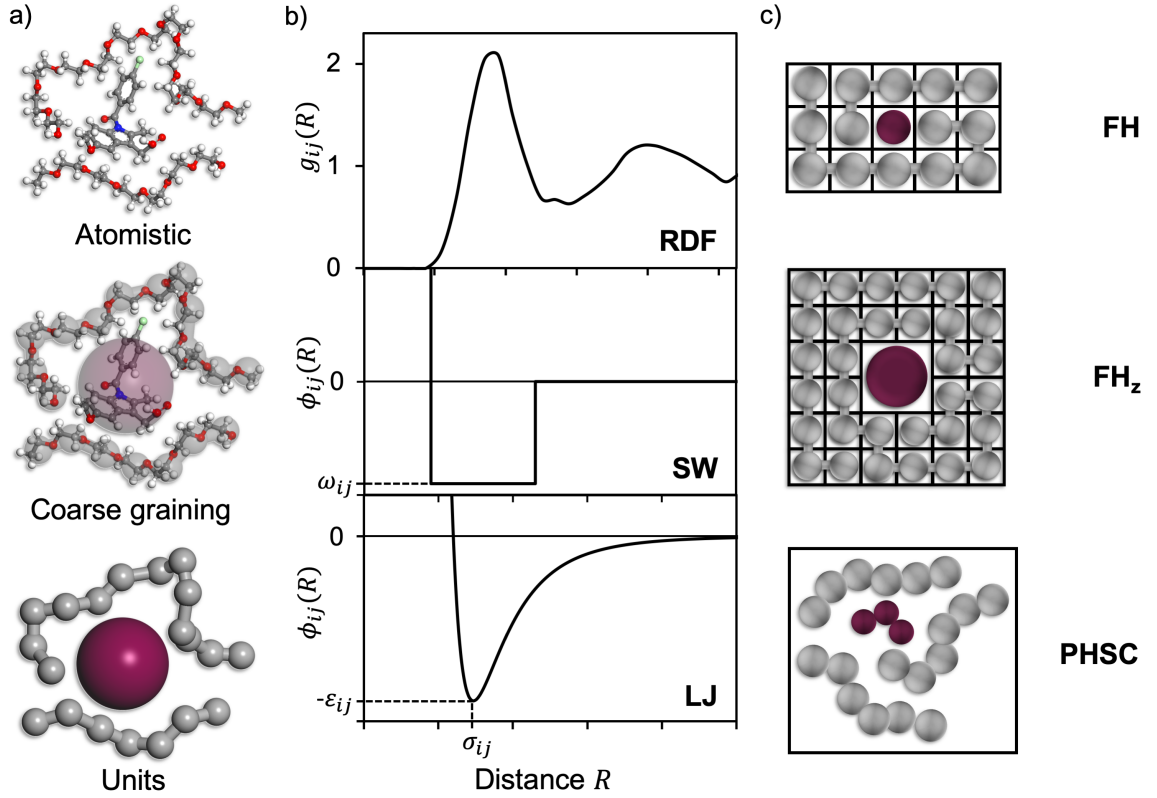
FIGURE 2.2: Thermodynamic models derived from atomistic simulations: a) coarse graining of atomistic models for definition of molecular units along with b) their intermolecular radial distribution functions (RDF) as well as the square-well (SW) and Lennard-Jones (LJ) pair potentials $\phi_{ij}(R)$. c) Representation of the employed thermodynamic models: Flory-Huggins theory (FH) and its correction considering unequally sized segments (FH$_z$) and the perturbed hard sphere chain (PHSC) equation of state.

purpose, the pressure p as a function of temperature T (evaluated at constant volume V) calculated using atomistic simulations (*cf.* Section 2.2.4) is used for calculation of the compressibility factor defined in eq 2.12 [127]:

$$Z = 1 + \frac{\rho_s}{kT} \frac{2\pi}{3} \sum_{i=1}^{l} \sum_{j=1}^{l} x_i x_j \int_0^{R_1} R\phi'_{ij} g_{ij}(R) R^2 dr, \qquad (2.32)$$

where ϕ'_{ij} is the first derivative of the effective LJ potential with respect to the distance R. For parameterization of the LJ potential by employing the CED and pressure as a function of temperature calculated from atomistic simulations, the cutoff distance R_1 in eqs 2.28 and 2.32 was set to 15 Å.

Solubility predictions using the Flory-Huggins (FH) theory

Solubility predictions using the Flory-Huggins (FH) theory [78, 79, 128] are based on the regular solution theory of non-electrolytes [76] by employing a mean-field lattice approach that defines the mixed state by equally sized (arbitrary defined) segments. Here, the average molar

volume of the mixture v_m was chosen as size of one segment. Each of these segments represent molecular fragments of a polymer or solvent molecule, respectively, interacting with an average energy per segment pair ω_{ij}. Therefore, the FH parameter χ_{FH} that determines the energy of mixing per segment $\Delta e_{mix,FH}$ is defined as [129]:

$$\chi_{FH} = \frac{z_{FH}}{RT} \left(\omega_{12} - 0.5 \left(\omega_{11} + \omega_{22} \right) \right), \tag{2.33}$$

where z_{FH} the segment coordination number of the mean-field lattice. Please note that since in FH theory every segment has the same size, the segment mole fractions x_i equal the commonly used volume fractions of the components. For a binary mixture containing segment fractions x_1 and x_2 of polymer and solvent segments, respectively, $\Delta e_{mix,FH}$ reads:

$$\Delta e_{mix,FH} = RT x_1 x_2 \chi_{FH}. \tag{2.34}$$

Since FH assumes an incompressible lattice, the molar enthalpy of mixing $\Delta h_{mix,FH} = \Delta e_{mix,FH}$ as well as $\Delta g_{mix,FH} = \Delta a_{mix,FH}$. Therefore, segment molar Gibbs energy of mixing $\Delta g_{mix,FH} = \Delta e_{mix,FH} - T\Delta S_{mix,FH}$ for polymer and solvent molecules consisting of r_1 and r_2 segments, respectively, is calculated with [129]:

$$\Delta g_{mix,FH} = RT \left(x_1 x_2 \chi_{FH} + \frac{x_1}{r_1} \ln x_1 + \frac{x_2}{r_2} \ln x_2 \right). \tag{2.35}$$

In order to consider changes of the intermolecular structure depending on the mixture composition, a composition dependent FH parameter χ_z based on the segment coordination numbers is derived in the following. This approach is similar to experimental studies that derived composition dependent FH parameters by fitting polynomial functions to experimental data [130]. Assuming the square well potential (eq 2.30), the general definition of the potential energy per segment given in eq 2.28 can be written as:

$$e = \frac{1}{2} \sum_{i=1}^{l} \sum_{j=1}^{l} x_i \omega_{ij} \, \rho_{s,j} \int_{R_0}^{R_1} 4\pi R^2 g_{ij}(R) dR. \tag{2.36}$$

Together with definition of the coordination number z_{ij}, which is the average number of segments j surrounding segments i in a spherical shell ranging from R_0 to R_1 (*cf.* Fig. 2.2):

$$z_{ij} = \rho_{s,j} \int_{R_0}^{R_1} 4\pi R^2 g_{ij}(R) dR, \tag{2.37}$$

eq 2.36 simplifies for a pure (p) amorphous polymer or solvent, respectively, only containing segments i to:

$$e_i = \frac{z_{ii,p}}{2} \omega_{ii}. \tag{2.38}$$

Similarly, the average coordination number $\overline{z}_{12} = x_1 z_{12} + x_2 z_{21}$ between unlike segments i-j in a binary mixture (m), eq 2.36 reads:

$$e_m = \frac{1}{2} \left(x_1 z_{11,m} \omega_{11} + x_2 z_{22,m} \omega_{22} + \overline{z}_{12} \omega_{12} \right). \tag{2.39}$$

Together with the CED ($e_i = -v_i c_i$) and the RDF obtained from atomistic simulations, eqs 2.38 and 2.39 can be used for calculation of ω_{ij} and, thus, χ_{FH} (eq 2.33). Furthermore, inserting eqs 2.38 and 2.39 into the general definition of the segment molar energy of mixing Δe_{mix} (eq 2.29), yields the energy of mixing $\Delta e_{mix,z}$ as a function of the coordination number changes $\Delta z_i = z_{ii,m} - z_{ii,p}$:

$$\Delta e_{mix,z} = \frac{1}{2} \left(x_1 \Delta z_1 \omega_{11} + x_2 \Delta z_2 \omega_{22} + \overline{z}_{12} \omega_{12} \right). \tag{2.40}$$

For the composition dependence of Δz_i and $\overline{z}_{12}$ quadratic polynomials are assumed:

$$\Delta z_i = J_i (1 - x_i)^2 + L_i (1 - x_i), \tag{2.41}$$

as well as:

$$\overline{z}_{12} = 2 J_{12} x_1 x_2. \tag{2.42}$$
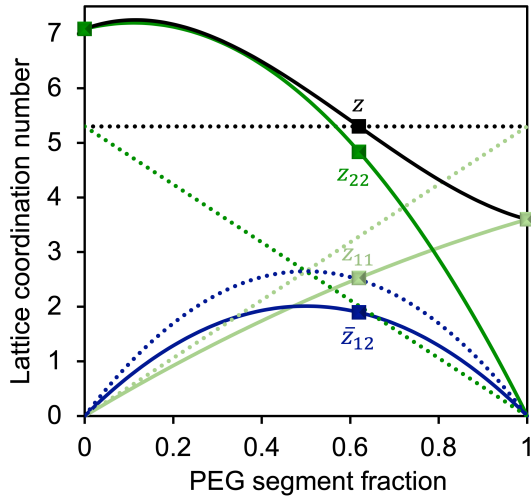
FIGURE 2.3: Coordination numbers z_{ij} and z as a function of the composition for PEG-H_2O mixture. Solid lines: model FH_z using eqs 2.38-2.42, dotted lines: FH theory, squares: values calculated from atomistic simulations.

Figure 2.3 shows the dependence of $z_{ii,m}$ and $\overline{z}_{12}$ on the composition calculated for the mixture containing polyethylene glycol (PEG) and H_2O (solid lines). The parameters J_i and L_i in eqs 2.41 and 2.42 are obtained using three known values of $z_{ii,p}$ and $\overline{z}_{12}$ at $x_i = 0$, $x_i = 1$ as well as the composition used for the atomistic simulations (squares in Fig. 2.3). Obviously, $\overline{z}_{12} = 0$ for compositions close to the pure states. In addition, the total coordination number z for which applies $z = x_1 z_{11,m} + x_2 z_{22,m} + \overline{z}_{12}$ is shown in Fig. 2.3.

In contrast to the FH theory (eq 2.33-2.35) that uses a composition independent lattice coordination number z_{FH}, the model functions eqs 2.41 and 2.42 allow to include the effect of different coordination states of unequal sized segments in the mixture as a function of the composition. Here, z_{FH} is defined as the total coordination number z of the mixture calculated from atomistic simulations. Due to the random FH mean-field lattice, the coordination numbers of the mixture are approximated as $\overline{z}_{12} \approx 2 x_1 x_2 z_{FH}$ and $z_{ii,m} \approx x_i z_{FH}$, respectively. Since the coordination numbers of the pure states are also $z_{ii,p} = z_{FH}$, in the FH theory the coordination number change Δz_i is approximated as linear function of the composition $\Delta z_i \approx z_{FH}(x_i - 1) = -z_{FH} x_j$. Inserting these relations into eq 2.40 results in the known FH expression for the energy of mixing $\Delta e_{mix,FH}$ given in eq 2.34 [129].

Similar to the FH theory, the model FH_z also assumes equally sized segments for the mixed state showing the average molar volume of the mixture v_m. However, the effects of unequal

sized particles on the lattice coordination number as a function the composition are considered by employing the composition dependent χ_z. For this purpose, eq 2.40 is rewritten for calculation χ_z, such that $\Delta e_{\mathrm{mix,z}} = RT x_1 x_2 \chi_z$, yielding:

$$\chi_z = \frac{1}{RT} \left(\frac{\overline{z}_{12}}{2x_1 x_2} \omega_{12} + 0.5 \left(\frac{\Delta z_1}{x_2} \omega_{11} + \frac{\Delta z_2}{x_1} \omega_{22} \right) \right). \tag{2.43}$$

Finally, inserting eqs 2.41 and 2.42 into 2.43, using $x_1 + x_2 = 1$ and defining the functions $F_i(x_i)$:

$$F_i(x_i) = \frac{\Delta z_i}{1 - x_i} = J_i(1 - x_i) + L_i, \tag{2.44}$$

as well as F_{12}:

$$F_{12} = \frac{\overline{z}_{12}}{2x_1 x_2} = J_{12}, \tag{2.45}$$

results in a linear dependence of the FH parameter χ_z on the composition:

$$\chi_z = \frac{1}{RT} \left(F_{12} \omega_{12} + 0.5 \left(F_1(x_1) \omega_{11} + F_2(x_2) \omega_{22} \right) \right). \tag{2.46}$$

In this way, a composition dependent correction of the FH theory can be directly obtained from atomistic simulations. However, it has to be examined if model $\mathrm{FH_z}$ using the simple functions, $F_i(x_i)$ and F_{12}, provides a reasonable modeling of the polymer solubility. This is addressed in Chapter 5.

So far, the atomic structure and CED of polymer, solvent as well as the corresponding mixture was considered. For this purpose, simulations of the pure components as well as the corresponding mixtures are required. However, a simplification of the FH interaction parameter in eq 2.33 provides a potential way for rapid estimation of the thermodynamic compatibility of polymer-active combinations by employing the so called mixing rule. That is approximating the CED of the mixture and, thus, also the intermolecular interaction between unlike lattice segments $i - j$, by the geometric average $c_{\mathrm{m}} = (c_i c_j)^{0.5}$ or accordingly for the SP $\delta_{\mathrm{m}}^2 = \delta_i \delta_j$ [77]. In this way, atomistic simulations of the mixture are not required and the effects of specific interactions such as hydrogen bonding are neglected. By using eqs 2.38 and 2.39 along with the definitions $e_i = -\overline{v}_{\mathrm{s}} \delta_i^2$ as well as $e_{\mathrm{m}} = -\overline{v}_{\mathrm{s}} \delta_{\mathrm{m}}^2$ [76] and assuming an average reference volume for the segments $\overline{v}_{\mathrm{s}}$, the FH parameter in eq 2.34 simplifies to the Hildebrand-Scatchard (HSC) equation by employing $\chi_{\mathrm{FH}} \approx \chi_{\mathrm{HSC}}$:

$$\chi_{\mathrm{HSC}} = \frac{\overline{v}_{\mathrm{s}}}{RT} \left(\delta_i - \delta_j \right)^2. \tag{2.47}$$

The concept of Hansen [80] separates the CED and SP, respectively, into different energy contributions yielding the so called Hansen solubility parameters. Applying this concept to the interatomic potential functions (IP) used in this work [131], the SP calculated by atomistic simulations (*cf.* Section 2.2.4) can be separated into electrostatic contributions (el) $\delta_{i,\mathrm{el}}$ and van der Waals (vdw) $\delta_{i,\mathrm{vdw}}$ contributions. For this purpose, the intermolecular energy is decomposed into the Coulomb (for $\delta_{i,\mathrm{el}}$) and Lennard-Jones (for $\delta_{i,\mathrm{vdw}}$) contributions of the IP such that the (total) Hildebrand SP reads:

$$\delta_i^2 = \delta_{i,\mathrm{el}}^2 + \delta_{i,\mathrm{vdw}}^2. \tag{2.48}$$

Following the concepts of Hansen to separate the SP and applying the mixing rules for both $\delta^2_{m,el} = \delta_{i,el}\delta_{j,el}$ and $\delta^2_{m,vdw} = \delta_{i,vdw}\delta_{j,vdw}$, the FH parameter χ_{HSC} for a polymer ($i, j = 1$) and solvent ($i, j = 2$) reads:

$$\chi_{HSC} = \frac{\overline{v}_s}{RT}\left(\left(\delta_{2,vdw} - \delta_{1,vdw}\right)^2 + \left(\delta_{2,el} - \delta_{1,el}\right)^2\right). \tag{2.49}$$

Here, $\overline{v}_s$ is the molar average volume for the considered set of solvents or active molecules, respectively. In accordance with the theory of Hansen [80], each compound i, j can be assigned to a point in the Cartesian coordinate system using $\delta_{i,el}$ and $\delta_{i,vdw}$ as coordinates. As can be seen from eq 2.49, the FH interaction parameter and, consequently, the energy of mixing increases with increasing differences of the electrostatic and vdw SP of the two compounds i, j, that is the mixture gets more endothermic. Therefore, if the distance between two points $(\delta_{1,vdw}, \delta_{1,el})$ and $(\delta_{2,vdw}, \delta_{2,el})$ exceeds a critical value, the two components become immiscible. In FH theory, the maximum interaction parameter for which two components are still miscible over the whole composition range is given by the critical FH parameter χ_c [129]:

$$\chi_c = \frac{1}{2}\left(\frac{1}{\sqrt{r_1}} + \frac{1}{\sqrt{r_2}}\right). \tag{2.50}$$

Since the segment volume was defined as average molar volume of the considered set of solvents, the number of segments per solvent molecule is $r_2 = 1$. Next, by using the equation of the circle with center defined by the SP of the polymer ($\delta_{1,vdw}, \delta_{1,el}$) one can determine the area around this point in which the polymer and a particular solvent with ($\delta_{2,vdw}, \delta_{2,el}$) are complete soluble over the whole composition range, that is, defining the critical distance R_c:

$$R_c^2 = \left(\delta_{2,vdw} - \delta_{1,vdw}\right)^2 + \left(\delta_{2,el} - \delta_{1,el}\right)^2, \tag{2.51}$$

for which applies $\chi_c = \chi_{HSC} = \overline{v}_s(RT)^{-1}R_c^2$. Rearranging this relation yields for R_c:

$$R_c = \sqrt{\frac{RT}{2\overline{v}_s}\left(1 + \frac{1}{\sqrt{r_1}}\right)}. \tag{2.52}$$

This concept denoted as solubility maps in Chapter 5 potentially provides rapid estimates of the polymer solubility. Central question is whether the SP $\delta_{i,vdw}$ and $\delta_{i,el}$ calculated using the employed IP provide a suitable separation of the intermolecular interactions for their application to the Hansen solubility concept. In this work, the solubility of polyethylene glycol (PEG) in different solvents is used as test case.

Perturbed hard sphere chain equation of state (PHSC EOS)

The parameterization of the FH lattice models described above employs only the CED combined with analytical expression for the ideal entropy of mixing assuming random occupation of an incompressible mean-field lattice. However, the known shortcomings of the FH theory due to assumption of random regular solutions, in particular the inaccurate modeling of mixtures showing pronounced specific interactions makes reliable solubility predictions using this approach difficult. In contrast, equation of state (EOS) theories proved to provide more accurate modeling of polymer solutions [100]. In addition, EOS theories allow to include the effects of hydrogen bonding on the physico-chemical properties of polymer mixtures [101,

102, 132]. Their parameterization most frequently used experimentally determined pressures as a function of the temperature $p(T)$. Here, the perturbed hard sphere chain (PHSC) EOS [103–105] is parameterized by employing temperature dependent CED $c_i(T)$ and pressures $p(T)$ calculated using atomistic simulations.

The starting point for most EOS is the Virial EOS given in eq 2.13, that is correcting the compressibility factor of the ideal gas $Z_{id} = 1$, yet employing more accurate expressions for the second Virial coefficient $B_2(T)$ considering pairwise particle correlations and interactions. In case of the PHSC EOS, the total compressibility factor Z (*cf.* eq 2.12) reads [103–105]:

$$Z = 1 + Z_{HS} + Z_{CB} + Z_{pert}. \tag{2.53}$$
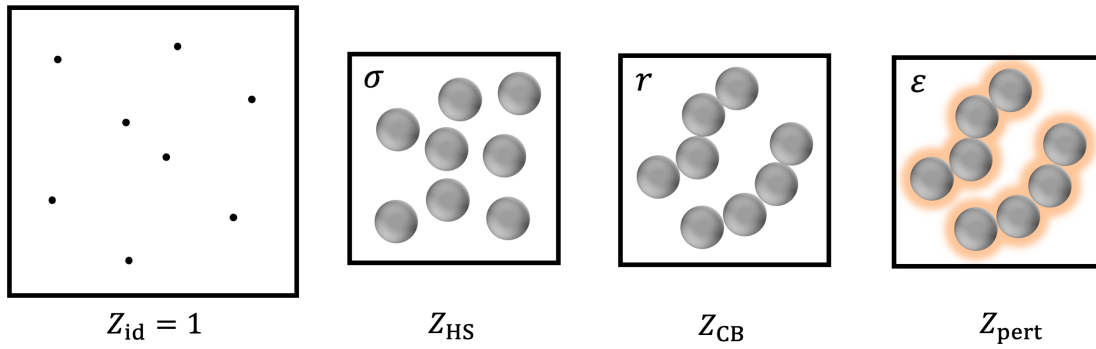
FIGURE 2.4: Simplified representation of the perturbed hard sphere chain equation of state for correction of the compressibility factor Z of the ideal gas (id) using a hard-sphere (HS) with the segment diameter σ, chain bonding (CB) with chain length r as well as a perturbation term (pert) with interaction energy ε.

Figure 2.4 shows a simplified representation of the contributions to Z for the PHSC EOS. It contains the compressibility factor for hard-sphere (HS) in contact, for chain bonding (CB) as well as a perturbation term (pert) considering (non-bonding) interaction energy. For a system with the molecular density ρ containing mole fractions x_i of molecule i showing r_i hard spheres per molecule, the compressibility factor Z_{HS} reads:

$$Z_{HS} = \rho \sum_{i,j}^{l} x_i x_j r_i r_j b_{vdw,ij} g_{ij}\left(\eta, \xi_{ij}\right). \tag{2.54}$$

Similar to the van der Waals (vdw) EOS given in eq 2.14, Z_{HS} takes the excluded volume of hard sphere particles in contact into account by using the vdw covolume $b_{vdw,ij}$. The major difference to the vdw EOS is the contact number $g_{ij}\left(\eta, \xi_{ij}\right)$ representing the radial distribution function (RDF) of HS in a dense liquid. In case of the PHSC EOS the Boublik-Mansoori-Carnahan-Starling (BMCS) equation is used as approximation of $g_{ij}\left(\eta, \xi_{ij}\right)$ for hard-sphere mixtures [133, 134]:

$$g_{ij}\left(\eta, \xi_{ij}\right) = \frac{1}{1-\eta} + \frac{3}{2}\frac{\xi_{ij}}{(1-\eta)^2} + \frac{1}{2}\frac{\xi_{ij}}{(1-\eta)}. \tag{2.55}$$

The packing fraction η, that is the ratio of the excluded volume for contacts of identical particles to the total volume, is defined as:

$$\eta = \frac{\rho}{4} \sum_i^l x_i r_i b_{\mathrm{vdw},i}. \tag{2.56}$$

In addition, the effective packing fraction ξ_{ij} for mixtures of unequally sized hard spheres reads:

$$\xi_{ij} = \frac{\rho}{4} \left(\frac{b_{\mathrm{vdw},i} b_{\mathrm{vdw},j}}{b_{\mathrm{vdw},ij}} \right)^{1/3} \sum_i^l x_i r_i b_{\mathrm{vdw},i}^{2/3}. \tag{2.57}$$

In order to model aspherical, chain like molecules such as polymers, a chain bonding compressibility factor Z_{CB} is added:

$$Z_{\mathrm{CB}} = - \sum_i^l x_i(r_i - 1) \left[g_{ii}(\eta, \xi_{ii}) - 1 \right]. \tag{2.58}$$

Together with $Z_{\mathrm{id}} = 1$, the HS and CB compressibility factors define the reference EOS $Z_{\mathrm{ref}} = 1 + Z_{\mathrm{HS}} + Z_{\mathrm{CB}}$, that is the statistical ensemble of non-interacting hard sphere chains sometimes denoted as the athermal part of the EOS. It includes only the pairwise particle repulsion of the liquid [104] defining the 'structure' of the HS chain liquid. In order to add intermolecular (non-bonding) interactions that do not affect the intermolecular structure, that is the RDF, the vdw perturbation term is added with $a_{\mathrm{vdw},ij}$ (eq 2.14) taking all attractive intermolecular interactions into account:

$$Z_{\mathrm{pert}} = -\frac{\rho}{kT} \sum_{i,j}^l x_i x_j r_i r_j a_{\mathrm{vdw},ij}. \tag{2.59}$$

For the PHSC EOS a temperature dependent vdw perturbation parameter $a_{\mathrm{vdw},ij}$ was derived [104]:

$$a_{\mathrm{vdw},ij} = \left(\frac{2\pi}{3} \right) \sigma_{ij}^3 \varepsilon_{ij} F_a(t). \tag{2.60}$$

Similarly, for the excluded volume (covolume) per particle contact $b_{\mathrm{vdw},ij}$ applies:

$$b_{\mathrm{vdw},ij} = \left(\frac{2\pi}{3} \right) \sigma_{ij}^3 F_b(t). \tag{2.61}$$

The empirically derived functions $F_a(t)$ and $F_b(t)$ depending on the reduced temperature $t = kT\varepsilon^{-1}$ are given as [135]:

$$F_a(t) = 1.8681 \exp(-0.0619\,t) + 0.6715 \exp\left(-1.7317\,t^{3/2}\right), \tag{2.62}$$

for the perturbation parameter and for the covolumina $F_b(t)$ reads:

$$F_b(t) = 0.7303 \exp\left(-0.1649\,t^{1/2}\right) + 0.2697 \exp\left(-2.3973\,t^{3/2}\right). \tag{2.63}$$

For parameterization of the PHSC EOS, three adjustable parameters determine the $p-V-T$ relation given by the compressibility factor Z in eqs 2.53-2.61. First, the diameter of a hard sphere segment σ_{ij} that corresponds to equilibrium (center-to-center) distance of, *e.g.*, the LJ potential (*cf.* Fig. 2.2). Second, the number of HS r_{ij} per molecular unit (polymer repeating unit or solvent/active molecule) that considers together with σ_{ij} the asphericity of the unit. Since the chain length depends on the degree of polymerization, that is the number of repeating units per polymer molecule N_{un}, the value $r^* = r_{ij}N_{un}^{-1}$ is used as characteristic quantity for a polymer in Chapter 5. And finally the parameter ε_{ij} quantifies the intermolecular interaction energy at the equilibrium HS distance σ_{ij} that corresponds, *e.g.*, to the minimum value of the LJ potential (*cf.* Fig. 2.2). If the CED and pressures for the mixture is available an additional parameter λ_{ij} can be used correcting the average particle (center-to-center) distance between unlike HS segments:

$$\sigma_{ij} = \frac{1}{2}\left(\sigma_i + \sigma_j\right)\cdot(1 - \lambda_{ij}). \tag{2.64}$$

Similar expression can be used for ε_{ij} of unlike segments, however, in this work ε_{ij} of unlike $i-j$ contacts was an additional adjustable parameter.

The PHSC EOS fails to describe strongly hydrogen bonding systems, that is it does not consider specific, directional interactions between the HS segments. As a consequence, lower critical solutions temperatures (LCST) or closed-loop phase diagrams as for aqueous PEG solutions [136] can not be described by this approach. A straightforward way to include the effects of specific interactions on the physico-chemical properties in EOS as well as lattice fluid (*e.g.*, FH) theories is to define temperature dependent interaction parameters. A simple model for the temperature dependence of ε_{ij} is to define two potentials for the intersegment interaction, one considering specific (directional) $\varepsilon_{s,ij}$ and one for non-specific $\varepsilon_{ns,ij}$ interactions [105, 136–138]. The actual interaction energy of the segments at temperature T is given by the average interaction parameter $\varepsilon_{ij}(T)$:

$$\varepsilon_{ij}(T) = \varepsilon_{ns,ij} + f_{ij}\delta\varepsilon_{ij}, \tag{2.65}$$

along with the fraction of specific interactions f_{ij}. This fraction is calculated by using the ratio of the probabilities that the segments interact in a non-specific manner (f_{ij}) to that for specific interactions ($1-f_{ij}$) assuming the Boltzmann distribution (*cf.* eq 2.2 with $E_i = -\varepsilon$) yielding [105, 136]:

$$f_{ij} = \left(1 + q_{ij}\exp\left(\frac{-\delta\varepsilon_{ij}}{kT}\right)\right)^{-1}, \tag{2.66}$$

along with the difference $\delta\varepsilon_{ij} = \varepsilon_{s,ij} - \varepsilon_{ns,ij} > 0$ and the ratio q_{ij} of degeneracy of non-specific to that of specific interactions. This leads to a modification of the temperature dependence of $a_{vdw,ij}$ in eq 2.60. At low temperatures the segments interact only via specific, directional interactions, while at elevated temperatures the probability of specific interactions decreases due to thermal excitation of, *e.g.*, rotational degrees of freedom leading to less pronounced directional interactions [137]. Such an approach has been successfully applied to the modeling of closed-loop phase diagrams as in case of PEG-H_2O mixtures by employing lattice fluid models [136]. Here, this model is also applied to the calculation of the FH parameter χ and χ_z

(eqs 2.33 and 2.46), which is similar to the definition of a temperature dependent FH parameter frequently used for modeling of LCST [129]. Please note that due to the definition of the interaction parameter of the square well potential ω_{ij}, eq 2.65 uses opposite sign (*cf.* Fig. 2.2).

With knowledge of the required parameters of the PHSC EOS, one obtains from the compressibility factor Z the pressure as function of temperature and number density $p(T, \rho)$, which allows calculation of all thermodynamic quantities. The (residual) internal energy e_{EOS} (here per molecule) with respect to the pure ideal gases of a liquid at temperature T, number density ρ_0 and containing mole fractions x_i of molecules of type i calculated from a pressure explicit EOS is given as [108]:

$$e_{\text{EOS}}(T, \rho_0, x_i) = \int_0^{\rho_0} \left(p - T \left(\frac{\partial p}{\partial T} \right)_\rho \right) \frac{d\rho}{\rho^2}. \tag{2.67}$$

Similar to the potential energy calculated from the effective LJ potential derived from the atomistic simulations (*cf.* eq 2.28), the potential energy e_{EOS} is connected with the CED $c_i = -\rho e_{\text{EOS}}$ (ρ is the inverse of ν_i used above) [76]. Similarly, the (residual) Helmholtz free energy a_{EOS} with respect to the pure ideal gases can be calculated using [108]:

$$a_{\text{EOS}}(T, \rho_0, x_i) = kT \int_0^{\rho_0} \left(\frac{p}{\rho kT} - 1 \right) \frac{d\rho}{\rho} + kT \sum_i^l x_i \ln \left(\frac{x_i \rho_0 kT}{p_0} \right). \tag{2.68}$$

In this work, e_{EOS} and a_{EOS} are numerically calculated for the corresponding T, ρ_0 and x_i. In addition, the enthalpy $h_{\text{EOS}} = e_{\text{EOS}} + pV$ as well as the Gibbs energies $g_{\text{EOS}} = a_{\text{EOS}} + pV$ are determined. Finally, this allows calculation of the chemical potential μ_i of component i, defined as partial derivative of the free energy with respect to the particle number N_i. In order to test the accuracy of the PHSC EOS derived from simulations, the physico-chemical properties of PEG and water as well as the corresponding phase diagram are calculated (*cf.* Chapter 5). Please note that as mentioned above the considered volume change of mixing and, thus, the volume work pdV at moderate pressures (below 200 bar) is negligibly small in case of the phase diagram calculations of PEG-H$_2$O. In addition, since the volume of incompressible phases such as solids and liquids changes only slightly with pressure, the vapor pressure of pure water was taken for calculation of the phase PEG-H$_2$O phase diagrams at all mixture compositions. All phase equilibrium calculations used the conditions of the mechanical $p'(T, \rho) = p''(T, \rho)$ and the chemical equilibrium $\mu_i' = \mu_i''$ of the phases $'$ and $''$.

In contrast to the FH theory, the segment size σ_{ij} or the number of segments r_i per molecule, respectively, are not arbitrarily defined but rather adjustable parameter for parameterization of the PHSC EOS to reproduce CED and pressures obtained from simulations. For derivation of the required parameters σ_{ij}, r_i, $\varepsilon_{\text{ns},ij}$, $\delta\varepsilon_{ij}$ and q_{ij}, the LJ potential derived from atomistic simulations is separated using the Weeks Chandler Anderson decomposition [139], which was also applied for derivation of the PHSC EOS [104], by splitting ϕ_{ij} into a repulsive:

$$\phi_{ij,\text{rep}}(R) = \begin{cases} \phi_{ij}(R) + \varepsilon_{ij} & R < \sigma_{ij} \\ 0 & R > \sigma_{ij} \end{cases}, \tag{2.69}$$

as well as an attractive part:

$$\phi_{ij,\text{att}}(R) = \begin{cases} -\varepsilon_{ij} & R < \sigma_{ij} \\ \phi_{ij}(R) & R > \sigma_{ij} \end{cases}, \tag{2.70}$$

such that $\phi_{ij} = \phi_{ij,\text{rep}} + \phi_{ij,\text{att}}$. As mentioned above, the reference EOS $Z_{\text{ref}} = 1 + Z_{\text{HS}} + Z_{\text{CB}}$ is only dependent on the repulsive potential $\phi_{ij,\text{rep}}$, while Z_{pert} contains only attractive inter-molecular interactions $\phi_{ij,\text{att}}$ [104]. Consequently, the pressure can be split into repulsive and attractive parts p_{att} (using Z_{pert}) and p_{rep} (using Z_{ref}). Similarly, the (residual) potential energy e_{EOS} (eq 2.67) and, thus, the CED can be split in the same way c_{att} and c_{rep}. This allows the targeted parameterization of the reference part of the PHSC EOS Z_{ref} for non-interacting hard sphere chains and the perturbation part Z_{pert} containing all attractive interactions. Therefore, the same separation of the CED and pressures is applied by employing the effective LJ potential obtained from simulations along with eqs 2.28 and 2.32. This procedure was used for derivation of the PHSC EOS parameters for PEG and H_2O by least square fitting of p_{att} and p_{rep} as well as c_{att} and c_{rep} for temperatures ranging from 300 to 550 K. Since the CED for PEG is considerably overestimated by the PHSC EOS (*cf.* Chapter 5), only the pressures p_{att} and p_{rep} were used for fitting of the parameters of unlike segments (λ_{12}, q_{12}, $\varepsilon_{\text{ns},12}$, $\delta\varepsilon_{12}$) in case of the PEG-H_2O mixture.

2.2   Structure and properties from atomistic simulations

As described in the Section 2.1, prerequisite for modeling the thermodynamic stability and materials properties under operating conditions by employing atomistic simulations is local-ization and sampling of appropriate atomistic structure model. In this section, the general concepts of computational methods employed are described, in particular the representation and sampling of the *potential energy surface* (PES). Subsequently, the atomistic simulations used in this work are described in more detail.

2.2.1   Potential energy surface (PES)

As shown in the Section 2.1.1, the key quantities for modeling of thermodynamic stability and materials properties from atomistic simulations are the energy of the electronic ground state $E_{0\kappa}$ of an atomic configuration κ and the canonical partition function $Q = \sum_{\kappa} Q_{\kappa}$ along with the probability P_{κ} of finding κ in the macroscopic state (*cf.* eq 2.7). First, the determination of a suitable approximation for Q_{κ} is required by calculation of $E_{0\kappa}$ and the energies of the vibra-tional states (*cf.* eq 2.1).

The problems addressed in this work, as for many other materials science related ques-tions, are connected with the (non-relativistic) electronic ground state and its energy $E_{0\kappa}$. How-ever, for the systems investigated here, the exact quantum mechanical description by solving the Schrödinger is impossible due to its high dimensionality. Therefore, a number of approxi-mations are needed, including the Born Oppenheimer approximation [140], which is the start-ing point for all subsequent considerations. Due to the large mass difference between elec-trons and nuclei, the electrons show considerably higher velocity compared to the nuclei in the system. Therefore, the electronic and nuclear motion can be decoupled from each other. This

allows separation of the molecular wave function into a wave function of the electrons and nuclei, respectively. Consequently, the (fixed) nuclear coordinates $\mathbf{X}$ of an atomic configuration κ are only parameters in the wave function of the electrons. The solution of the Schrödinger equation of the electrons for the electronic ground state yields the (potential) energy $E_{0\kappa}$ representing one point of the *potential energy surface* $E_{0\kappa}(\mathbf{X})$ (PES). In case of molecules or gas phase clusters containing N atoms, the PES is a function of the $3N$ dimensional vector $\mathbf{X}$. For solids the PES is also a function of the unit cell volume V or the lattice parameters.

However, solving the Schrödinger equation of the electrons even by using approximated wave function based methods is for the questions addressed here still computationally too demanding. Therefore, the quantum mechanical simulations used in this work are performed at the Kohn-Sham (KS) density functional theory (DFT) level [141–143]. Central quantity in DFT for calculation of $E_{0\kappa}$ is not the $3N_{\mathrm{el}}$ dimensional electronic wave function (for N_{el} electrons) but the electron density as a function of the 3 dimensional position vector. The potential energy is expressed as functional of the electron density. This functional with unknown exact expression can be separated into functionals of different energy contributions. Among them are the (classical) Coulomb interactions between electrons among each other as well as between electrons and nuclei, which can be computed exactly. In addition, the functional for the kinetic energy of the electrons is computed for a fictitious reference system of non-interacting electrons (*i.e.*, no explicit electron-electron interaction) moving in an effective potential and showing same electron density as the real (interacting) system. Since the KS DFT assumes such a fictitious reference system of N_{el} non-interacting electrons the functional of the kinetic energy can be computed exactly as well. The remaining contributions to the potential energy that cannot be treated exactly are summarized in the exchange-correlation (XC) functional. This functional takes everything unknown (not exactly calculable) into account, that is, the non-classical electron-electron interactions as well as the difference of the kinetic energy between the reference system of non-interacting electrons and the real interacting system. Different approximations are available for the XC-functional such as the generalized gradient approximation (GGA), *e.g.*, the PBEsol [144, 145] XC-functional used in Chapter 3.

Due to the assumption of non-interacting electrons in KS DFT, the many body problem of N_{el} electrons is expressed as set of N_{el} one-electron Schrödinger equations (Kohn-Sham equations). Solution of the KS equations provides the orbitals (one-electron wave functions) and the corresponding energy eigenvalues (orbital energies). The orbitals are represented by a set of basis functions. For molecular systems as in Chapter 4 Gaussian type orbitals (GTO) are employed, while for solids as in Chapter 3 plane wave basis sets are frequently used. The electron density is calculated from the square of the absolute value of every occupied orbital. Since the Hamiltonian of the one-electron Schrödinger equations also depends on the electron density, the ground state electron density that minimizes the potential energy is calculated by an iterative procedure (self-consistent field method) yielding $E_{0\kappa}$.

However, for simulations of structure and properties of materials that require structure models containing several thousand atoms as well as for simulation times in the ns scale calculations at DFT level are computationally too demanding. Therefore, simplified expressions for the PES $E_{0\kappa}(\mathbf{X})$ using interatomic functions (IP) are applied in this work to facilitate simulations at larger time and space scales. Such IP can be derived either by employing quantum mechanical simulations (*e.g.*, at the DFT level) or experimental data. In Chapter 4 tailored IP

for accurate and computationally efficient simulations of Fe_2O_3 are used, which were previously derived in the author's master thesis [68] and ref. [XI] by employing DFT simulations. They assume the functional form of the Born Mayer Huggins pair potential for ionic solids [146]. In contrast, the IP used for atomistic simulations of polymers in Chapter 5, the IP contain not only pair potentials but also three (bonding angles) and four-body (torsion angles) terms for an accurate modeling of polymer conformations [131].
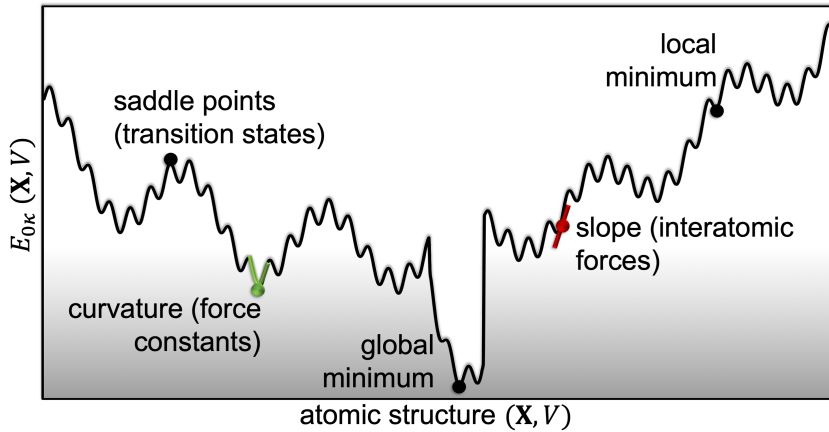
FIGURE 2.5: Simplified representation of the $3N + 1$ dimensional potential energy surface (PES) as potential energy $E_{0\kappa}$ (*cf.* eq 2.4) as a function of the ($3N$ dimensional) nuclear coordinates $\mathbf{X}$ and unit cell volume V (in case of solids).

Figure 2.5 depicts a simplified representation of the PES $E_{0\kappa}$ as a function of the nuclear coordinates $\mathbf{X}$ and, in case of solids of the volume V, which can be calculated with the methods described above. It contains all information required in this work for modeling the thermodynamic quantities and related materials properties. It shows one global as well as numerous local minima representing stress and force free atomic structures that are at $T = 0$ K stable and metastable, respectively. The first derivative of $E_{0\kappa}$ with respect to the nuclear coordinates $\mathbf{X}$ correspond to the interatomic forces, while the second derivative (curvature) with respect to $\mathbf{X}$ at the minima provides the force constants, which can be evaluated numerically, *e.g.*, by using finite differences approach [126]. That is, the forces acting on the atoms are calculated for two small displacement per atom and direction in space. This allows the calculation of the dynamical matrix from the obtained force constants and by applying the harmonic approximation the vibrational frequencies and the related thermodynamic quantities [9, 126, 147] required in the Sections 2.1.2 and 2.1.3 for modeling of the BZS solid solutions. In addition, applying this approach to different unit cell volumes facilitates the calculation of the volume dependence of vibrational frequencies (quasi-harmonic approximation) yielding the microscopic Grüneisen parameter (Section 2.1.3). Similarly, the second derivative (curvature) with respect to the unit cell volume V at the minima obtained from, *e.g.*, numerical differentiation by evaluation of stress tensor for a set of unit cell deformations (elongation and shearing) yields together with the stress-strain relation (Hookes law) the elastic constants also required in Section 2.1.3 [148]. Furthermore, the saddle points of the PES correspond to transition structures, *e.g.*, of chemical reactions or phase transitions. They are not explicitly considered in this work.

Sampling of the PES

So far, the calculation of the (approximated) partition function Q_κ of a particular atomic structure κ characterizing the microstate of κ was considered. Now, for determination of a sufficiently good approximation of the partition function $Q = \sum_\kappa Q_\kappa$ and its related thermodynamic quantities (*cf.* eq 2.5), sampling of the PES $E_{0\kappa}(\mathbf{X})$ of numerous atomic configurations is required. Central task is the calculation of the ensemble average of atomic configurations and the corresponding properties for the adequately accurate modeling of the macroscopic materials properties.

One computational method to achieve this is the Monte-Carlo (MC) algorithm [109] that facilitates the calculation of the ensemble average by randomly sampling points of the configuration space and the PES. However, the exact value for the partition function Q is most frequently not available for high dimensional PES considered in this work. Therefore, Metropolis et. al. [149] proposed an efficient sampling scheme for generation of a random walk through configuration space avoiding the direct calculation of Q. Starting from an initial structures $\kappa 1$, random displacements (trial moves) are applied yielding a new structure $\kappa 2$. If $E_{0\kappa 2} < E_{0\kappa 1}$ this random move is accepted and the next random displacement is applied to $\kappa 2$. In case of $E_{0\kappa 2} > E_{0\kappa 1}$, the ratio of the Boltzmann probabilities of both structures $\kappa 1$ and $\kappa 2$ is calculated for a certain sampling temperature T given according to eq 2.7. Therefore, partition function cancels yielding the transition probability π from $\kappa 1$ to $\kappa 2$ that reads $\pi = \exp(-\beta(E_{0\kappa 2} - E_{0\kappa 1}))$. The value of π is then compared with a random number in the interval $[0, 1]$ drawn from a uniform distribution. If π is larger than the obtained random number, the trial move is accepted otherwise it is rejected. Every property Y_κ of the atomic structures sampled is then used for calculation of the ensemble average $\overline{Y}$ using the arithmetic average to obtain an approximation for the corresponding macroscopic properties [109].

Another possibility for sampling of the PES are molecular dynamics (MD) simulations. Starting from an initial structure along with random initial velocities, the time evolution of the system is calculated by numerical integration of the Newton equations of motion with respect to the time using predefined (finite) time steps. Among the finite difference methods for integration of the equations of motion is, *e.g.*, the Verlet algorithm [150]. These approaches are based on the calculation of the interatomic forces (*cf.* Fig. 2.5) yielding the accelerations, velocities and the positions (trajectory) of the atoms at every time step until a predefined total number of time steps is reached. In the first stage of MD simulations, the initial configuration is equilibrated until the properties of interest such as energy, pressure, temperature, etc. reach a steady (equilibrium) state. In the following second stage - the production phase - the properties fluctuate around their average equilibrium values. The fundamental hypothesis for calculation of the ensemble average and the related properties for characterization of the macroscopic state is the ergodic hypothesis [109]. It states the arithmetic average of the microstates over time obtained from MD trajectories equals ensemble average. That is, during the production phase of the MD simulation, the most relevant points in phase space (atomic configurations κ and momenta) are sampled (quasi-ergodicity). A straightforward test whether an atomistic simulation procedure is (quasi-)ergodic can be performed by repeating the same procedure starting from different initial conditions, that is, using distinct points in configuration space and initial velocities [151]. However, in case of MD simulations of, *e.g.*,

amorphous materials at temperatures below or slightly above the glass transition temperature, the sampling of the PES (and phase space) is confined to a subset of points on the PES (basin) yielding broken ergodicity [151–153]. The sampling of atomic structures and properties for amorphous materials such as polymers are described in more detail in Section 2.2.4.

Both, MC and MD simulations sample microstates in a particular statistical ensemble. The most important are the microcanonical NVE (constant particle number, volume, total energy), the canonical NVT (constant particle number, volume, temperature) and the isothermal-isobaric NPT ensemble (constant particle number, pressure, temperature). The latter two require control of pressure and temperature, respectively. In case of MD simulations, pressure and temperature control is achieved by employing thermostats such as the Nosé-Hoover thermostat [154, 155] as well as barostats for pressure control using, *e.g.*, the Berendsen [156] or Parrinello-Rahman [157] barostat. In this work, statistical sampling of microstates using the canonical (NVT) along with the Nosé-Hoover thermostat is of particular importance. For this purpose, the Newton equations of motion are modified to control particle velocities such that the system is effectively coupled to a heat bath showing the desired target temperature. After proper equilibration, the system fluctuates in thermal equilibrium with the fictitious heat bath, and therefore, the probability of obtaining a microstate with energy $E_{0\kappa}$ corresponds to the Boltzmann distribution P_κ given in eq 2.7. This is a necessary condition to ensure an (quasi-)ergodic sampling of the phase space.

One crucial prerequisite for calculation of materials properties as well as proper sampling of the PES and phase space by employing MD and MC simulations, respectively, is the initial structure model chosen. In some cases a reasonable initial guess of the atomic structure can be obtained from experiments, *e.g.*, crystal structures determined by X-ray diffraction. However, in case of substitutional solid solutions (*cf.* Section 2.1.2) exact atomic structure models would require tremendously large unit cells due to numerous possible configurations of the substitutional atoms (configurational entropy). Instead, the average properties can be calculated by generation of various atomic configurations starting from experimentally determined crystal structures [112] described more detailed in Section 2.2.2. In addition, the experimental characterization of the detailed atomic of nanoparticulate materials and small gas phase is very challenging. Therefore, simulation procedures for structure predictions finding low lying or even the global energy minimum of the PES, that is localization structures with high probability P_κ, is indispensable for an accurate modeling of the materials properties. One procedure frequently used for localization of low-energy structures by employing MC [109]) or MD simulations (*e.g.*, ref. [158]) is the simulated annealing. Starting from an initial structure model, an equilibration at sufficiently high temperature is applied such that enough kinetic energy is available to leave the initial, local minimum and to overcome (high lying) energy barriers of the PES (*cf.* Fig. 2.5). Subsequently, this equilibrated 'molten' state is gradually cooled to obtain atomic configurations that correspond to a low lying local or even the global minimum of the PES.

Another simulation procedure used this work for global structure optimizations is the genetic algorithm (GA) - a search heuristic inspired by concepts of biological evolution [8]. The GA is initialized using a set (population) of randomly generated structures that are subsequently optimized to a close lying local energy minimum. For the optimized structures, the

quality or 'fitness' is calculated using an objective function (here $E_{0\kappa}$), which has to be minimized. The fitness of an atomic configuration determines the probability that a structure is selected from the population as 'parent' for creation of the next generation. Then, random fragments of two parents are combined by means of crossover operations into an offspring whose structure is optimized as well. The fundamental assumption of the GA is that energetically favorable structural features of the two parent structures are combined in a new, energetically lower lying structure. If the offspring is indeed a new low energy structure, it will be added to the GA population while a structure higher in energy is removed such that the total population size remains constant. Due to this 'natural selection' the GA is guided in direction of the global minimum. In order to avoid premature convergence of the algorithm into a local minimum and to ensure high structural diversity of the GA population, mutations (random structural changes) are applied to randomly chosen structures. In addition, before adding a new structure to the population, it is compared with every member of the GA population by means of a similarity detection procedure [159] in order to avoid filing of the population with almost identical structures. Such a GA is applied to the elucidation of stable (metastable) Fe_2O_3 gas phase clusters described in Chapter 4.

2.2.2 DFT simulations of zero thermal expansion glass ceramics

As mentioned in the previous section, starting point for accurate modeling of materials properties and thermodynamic phase stability are suitable atomic structure models. While the crystal structure for the low (LT) and high temperature phase (HT) of $BaZn_2Si_2O_7$ (BaZn) is known from X-ray diffraction experiments [20], the exact atomic positions of substitutional ions (Sr^{2+}, Mg^{2+}) in $Ba_{1-m}Sr_mZn_{2-2n}Mg_{2n}Si_2O_7$ (BZS) solid solutions cannot be determined experimentally. Due to the configurational entropy, the macroscopic state of BZS solid solutions is expected to show rather a large set of possible atomic configurations that cannot be represented using a single unit cell. Therefore, a sampling of the configuration space for different possible substitutions is indispensable for modeling the atomic structure and related properties. For this purpose, simulations at the density functional theory level were applied to the LT and HT phase of BZS solid solutions for 25 chemical compositions ranging from BaZn ($m, n = 0$) to SrZn ($m=1$, $n=0$), BaMg ($m=0$, $n=1$) as well as SrMg ($m=1$, $n=1$). The structure models generated in 0.25 steps for m and n for the intermediate compositions are denoted as Sr($100m$)Mg($100n$), *e.g.*, Sr50Zn and Sr50Mg25 refer to the chemical compositions ($m = 0.5$, $n = 0$) and ($m = 0.5$, $n = 0.25$), respectively.

Starting from the crystal structure of BaZn (LT and HT phase) [20], initial structure models for BaMg, SrZn and SrMg were constructed by simply replacing the corresponding ions on their lattice positions. In order to locate the lowest energy structures of $Ba_{1-m}Sr_mZn_2Si_2O_7$ ($n = 0$) and $BaZn_{2-2n}Mg_{2n}Si_2O_7$ ($m = 0$) solid solutions, initial structure models were generated by employing the crystal structure of the LT and HT phase of BaZn along with the side order-disorder (SOD) program [112]. It generates structure models using the crystal symmetry of BaZn LT and HT phase, that is, $C2/c$ (No. 15) for LT and $Cmcm$ (No. 63) for HT, and replaces Ba^{2+} and Zn^{2+} on every symmetry inequivalent lattice side with Sr^{2+} and Mg^{2+}, respectively. Next, single point calculations of $E_{0\kappa}$ were applied to every structure model obtained. In this way, the probability of every configuration P_κ (eq 2.7) and the configurational entropy S_{conf} (eq

2.9) can be calculated. Then, all structures of the HT phase were geometrically optimized using constant (zero) pressure conditions. Due to the high number of structure models in case of the LT phase (up to 1742 for BaMg50), the configurations were grouped into sets of structure models having the same crystal symmetry (space group). Then, (constant zero pressure) geometry optimizations were applied to structure models selected from each set with relative energies of less than 1 kJ/mol with respect to the lowest energy structure in the corresponding set (about 40 optimizations per composition).

Finally, the initial structure models for $Ba_{1-m}Sr_mZn_{2-2n}Mg_{2n}Si_2O_7$ with both $m > 0$ and $n > 0$, were generated by using the combination of the Ba^{2+}/Sr^{2+} and Zn^{2+}/Mg^{2+} positions of the lowest energy structures obtained for the solid solutions ($m = 0$, $n > 0$) as well as ($m > 0$, $n = 0$).

All DFT calculations employed the *Vienna ab initio Simulation Package* (VASP) [160, 161]. The PBEsol exchange correlation functional [144, 145] in combination with the empirical dispersion correction of Grimme et al. [162] was used along with the Projector Augmented Wave (PAW) method [163, 164]. Calculations under constant pressure and constant volume conditions were performed with an energy cutoff of 900 and 400 eV for the plane wave basis sets, respectively. Integration of the first Brillouin zone used Monkhorst-Pack [165] grids with a linear k-point density of about 13 Å for each lattice vector. Finally, calculation of the vibrational density of states (VDOS) for the lowest energy structures of BaZn, Sr50Zn, SrZn, BaMg50 and BaMg were performed by employing the finite difference (frozen-phonon) approach implemented in Phonopy [126]. For this purpose, 2×1×1 and 2×1×2 supercells for the LT and HT phase were used, respectively. Thermodynamic quantities such as heat capacity and vibrational free energy required for the models described in Section 2.1.2 and 2.1.3 are calculated from the phonon frequencies [9, 126] by employing Monkhorst-Pack grids with a linear k-point density of about 140 Å for each lattice vector.

For determination of the thermomechanical properties of the HT phase for BaZn, Sr25Zn, Sr50Zn and Sr75Zn (*cf.* Section 2.1.3), the elastic constants of the stiffness tensor **C** are obtained using the stress tensor calculated for six unit cell deformations and the stress-strain relation (Hookes law) as implemented in VASP [148]. In order to shed a light on the microscopic origin of zero thermal expansion of the Sr50Zn HT phase, the microscopic Grüneisen parameters $\gamma_{\mathbf{k}i}$ (eq 2.25) were obtained by employing phonon calculations along with the quasi-harmonic approximation [126] for isotropically deformed unit cells with a volume expansion and contraction of -3% and +3%, respectively.

2.2.3 Structure prediction of Fe_2O_3 cluster and nanoparticles

For elucidation of the atomic structure of Fe_2O_3 gas phase cluster and nanoparticles (NP), global structure optimizations and molecular dynamics simulations are applied, that is, numerous calculations of $E_{0\kappa}$ for a large set of configurations κ are required. Due to the complex electronic structure connected with the magnetic (spin) states of Fe_2O_3 makes calculations at the DFT level very challenging for such simulation procedures. Therefore, *ab initio* derived interatomic potential functions (IP-Fe_2O_3) are the main computational tool used in the present study. As mentioned in Section 2.2.1 they were derived using simulations at the DFT level (refs. [68] and [XI]) in order to accurately reproduce the structure and relative lattice energies of the bulk Fe_2O_3 polymorphs. The employed methodology for the structure predictions described

here was previously published in *Nanoscale* (RSC Publishing) [XI] from which parts of section are adapted from.

The determination of global minimum structures of $(Fe_2O_3)_n$ nanoclusters with n = 6-10 used a two stage procedure. First, for each cluster size global structure optimizations employing the genetic algorithm [8] described in Section 2.2.1 in combination with the IP-Fe_2O_3 were performed. At least two independent GA runs with up to 4000 local optimizations in each case (80 generations, 50 structures per population) were performed yielding identical low energy isomers. Next, the structures of the 50 most stable isomers were refined at the DFT level. Since the geometric structure and relative energies of different isomers of larger $(Fe_2O_3)_n$ clusters are only weakly dependent on the precise magnetization (spin) state [XII], ferromagnetic states are assumed for geometry optimizations of clusters with n > 6. The DFT calculations were performed using the TURBOMOLE program package [166–168] along with the B3-LYP exchange-correlation functional [169–171] and triple-zeta valence plus polarization (TZVP) basis sets for all atoms[172]. The multipole accelerated resolution of the identity (MARI-J) method [173] for the Coulomb term employing the corresponding auxiliary basis sets [174] was applied to accelerate the calculations. The binding energies ΔE_b of the clusters with respect to the ground state isomer of Fe_2O_3 were computed as energies of the reaction:

$$(Fe_2O_3)_n \rightarrow nFe_2O_3 \tag{2.71}$$

Molecular dynamics simulations of larger $(Fe_2O_3)_n$ NP were performed employing the Large-scale Atomic/Molecular Massively Parallel Simulator (LAMMPS) [175] along with the IP-Fe_2O_3. Initial configurations were constructed as spherical cutouts from α-Fe_2O_3 (Hematite) [176, 177] with diameters of 1 (n = 80, **NP1**), 3 (n = 282, **NP3**) and 5 nm (n = 1328, **NP5**). The simulated crystallization used the following procedure. First, the initial structures were equilibrated at 2000 K for 1 ns. Next, for each NP size six different models of the molten NP taken from the second half of the equilibration phase were cooled down from 2000 to 300 K and subsequently optimized. The cooling procedure applied linear velocity scaling for 1 ns in the temperature ranges of 2000-1500 K and 1000-300 K. Between 1500 and 1000 K velocity scaling was applied for 10 ns. All MD simulations were carried out using a time step of 2 fs and without periodic boundary conditions. To verify the independence of the final NP structures from the initial configuration a second 5 nm large $(Fe_2O_3)_n$ NP model was constructed as a spherical cutout from γ-Fe_2O_3 [178] and subsequently annealed applying the same procedure.

For determination of the melting point depression of the Fe_2O_3 NP, the melting temperature of bulk α-Fe_2O_3 was calculated by employing a series of independent MD simulations at increasing temperatures between 1800-2200 K with a step of 50 K. At each temperature, a 3D periodic 3×5×2 supercell of α-Fe_2O_3 (orthogonal unit cell) was equilibrated for 1 ns employing the isothermal-isobaric (NPT) ensemble. The Nosé-Hoover thermostat and barostat were used following the equations of motion of Shinoda *et al.*[179, 180] along with a target pressure of 1 atm and a time step of 2 fs. The average potential energy of the system was evaluated for the last 200 ps.

2.2.4   Atomistic simulations of amorphous polymers

The major challenge of atomistic modeling of bulk amorphous materials is the lack of long range order since atomistic structure models of bulk systems require periodic boundary conditions that inherently assume long range order. Therefore, in order to provide an adequate statistical sampling of the configuration space and the PES, the unit cells have to include a sufficiently large number of atoms (degrees of freedom). This means for polymers that the sampling of the PES and calculation of the required properties such as cohesive energy densities (CED) has to include enough conformations of macromolecules.

To achieve this, a computational procedure for calculation of structure and properties of amorphous materials is applied, which is based on the concepts initially proposed by Stillinger and Weber [88–90]. It employs MD simulations of the equilibrated liquid state, that is at T above the glass transition temperature T_{g} such that the atoms have sufficient kinetic energy to overcome barriers of the PES. Structure optimizations of the obtained MD trajectories yield the so called inherent structures (IS) along with the distribution of their potential energies (per atom) e_{IS}. This distribution corresponds to the probability distribution $P(e_{\mathrm{IS}})$ that an atomic configuration extracted from the equilibrated liquid state is represented by the IS with energy e_{IS}. In addition, the partition function Q can be separated into non-overlapping basins [89], which are characterized by the IS representing a particular basin of the PES. If the MD simulations at $T > T_{\mathrm{g}}$ provide (quasi-)ergodic sampling, the probability distribution $P(e_{\mathrm{IS}})$ obtained is related to the Boltzmann distribution and the canonical partition function Q (*cf.* P_{κ} in eq 2.7) [91, 92]. Therefore, this approach can be used not only for predictions of the atomic structures, but also for calculations of thermodynamic quantities of glass forming liquids at temperatures above T_{g}. However, for temperatures close to T_{g} and below, the kinetic energy is too low to overcome higher lying energy barriers of the PES yielding broken ergodicity [152]. That is, not all configurations that can be present in the macroscopic state are accessible within the course of one single MD simulation and the sampling is restricted to a particular basin of the PES providing local (internal) ergodicity [153]. In case of polymers, such a sampling of IS even above T_{g} would require long equilibration times (upto microseconds [84, 85]) of the MD simulations due to the relatively slow relaxation of polymer backbone conformations. This makes calculations of thermodynamic quantities by sampling of IS using MD simulations very challenging. However, it potentially provides an efficient way for predictions of the atomic structure and properties such as CED and pressures of amorphous polymers required for parameterization of the thermodynamic models described in Section 2.1.4.

The simulation procedure applied in this work combines MC and MD simulations for an efficient sampling of the PES, denoted here as inherent structure sampling (ISS). A simplified representation of this approach is depicted in Fig. 2.6. First, atomistic structure models of the bulk polymer showing distinct polymer conformations (**MC1**-**MC3**) are generated by employing a configuration biased MC algorithm [87]. Subsequently, comparatively short MD simulations (less than 1 ns) are performed for every MC constructed structure model. As mentioned above, by applying structure optimizations to the calculated MD trajectories the IS along with their potential energy per atom e_{IS} are obtained. Since the MD simulations use short simulation times and moderate temperatures close to T_{g}, the ISS is restricted to the basins of the PES corresponding to the polymer conformations **MC1**-**MC3** as indicated by the colored areas in Fig. 2.6. However, assuming local (internal) ergodicity within the PES basins the ISS yields
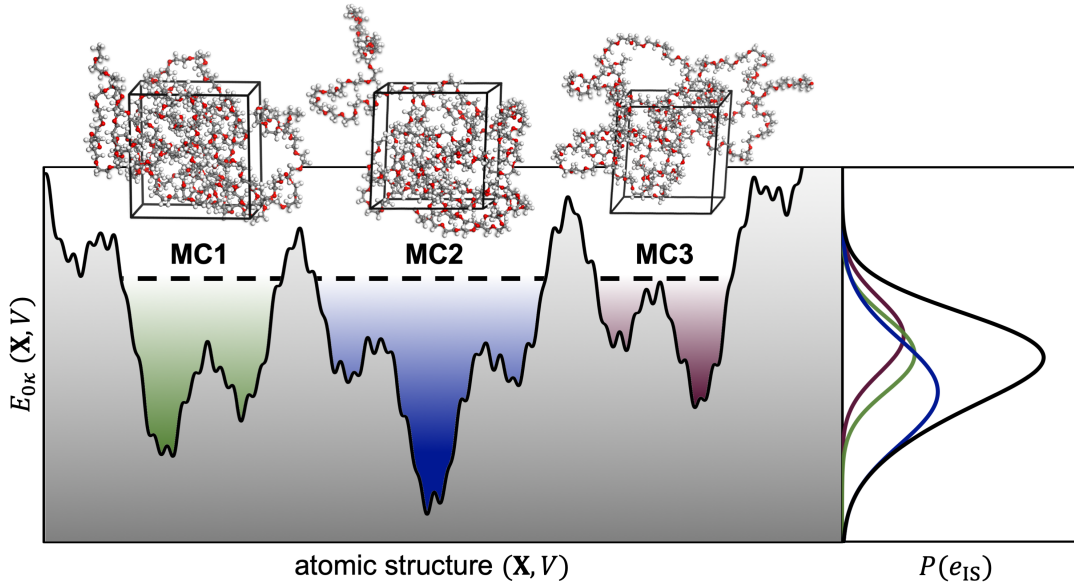
FIGURE 2.6: Sampling of the potential energy surface $E_{0\kappa}$ by applying structure optimizations to MD trajectories of different polymer conformations (**MC1**-**MC3**) yielding inherent structure (IS) energies e_{IS}. Colored areas indicate accessible values for e_{IS} during the sampling yielding the probability distributions $P_i(e_{IS})$ (colored curves) used for calculation of the total distribution function $P(e_{IS})$ (black curve, eq 2.72).

for a certain polymer conformation i (*e.g.* **MC1**) the distribution $P_i(e_{IS})$. The total (average) probability distribution $P(e_{IS})$ that an IS with energy e_{IS} characterizes the macroscopic state is calculated for n_{MC} polymer conformations sampled by the ISS:

$$P(e_{IS}) = \sum_{i=0}^{n_{MC}} w_i P_i(e_{IS}),\qquad(2.72)$$

using the Boltzmann weights $w_i = \exp(-\beta\overline{e_{IS,i}})\Pi^{-1}$ along with $\Pi = \sum_i^{n_{MC}} \exp(-\beta\overline{e_{IS,i}})$ and the average IS energy $\overline{e_{IS,i}}$ of conformation i. Average quantities $\overline{Y}$, such as CED or pressure, are calculated with $\overline{Y} = \sum_i^{n_{MC}} w_i Y_i$ employing w_i and average properties Y_i calculated from MD simulations. The average intermolecular RDF of the molecular units $g(R) = \sum_i^N P_i g_i(R)$ is calculated using the RDFs of the coarse-grained models $g_i(R)$ of the N IS obtained. Major advantage of the ISS is the simple yet efficient parallelization by using n_{MC} independent MD samplings of the polymer conformations and related properties. Here, systematic test simulations for this procedure were performed, in particular for the evaluation of the required n_{MC} (up to 10 in this work) by using the model polymer polyethylene glycol (PEG) with chain length 50 as well as its mixture with water. The unit cells contain 3 and 500 molecules in case of the structure models for pure PEG and water, respectively. In case of the PEG-H_2O mixture 3 PEG and 92 water molecules were used, which corresponds to a PEG weight fraction of about 80 wt.%.

As an alternative to the ISS, sampling of distinct polymer conformations can also be achieved using one single MD simulation of structure models containing a sufficiently high number of polymer molecules, here denoted as direct sampling (DS). For this purpose, the same MC procedure for generation of the amorphous structures was used followed by an equilibration

employing MD simulations. To test the reproducibility of the DS for calculation of the CED, the procedure was repeated 10 times for the model polymers PEG (chain length 25 and 50) as well as polylactic acid (PLA) with chain length 25 using structure models containing 1 up to 30 molecules. In addition, in order to test the accuracy of the employed interatomic potential functions, the DS was also applied to several commonly used solvents listed in Table 5.1 (Section 5.1.1) using structure models with 800 molecules. The simulations for the DS were performed in collaboration with Mr. Mingzhe Chi [181].

Both simulation procedures described above, the ISS and DS, were performed by using software from Dassault Systèmes BIOVIA implemented in the Materials Studio (Version 17.1) program suite along with the COMPASSII force field [131]. Construction of amorphous, three dimensional unit cells used the configuration biased Monte Carlo procedure implemented in the *Amorphous Cell* module, which is based on the algorithm of Theodorou and Suter [86, 87]. In case of low molecular weight compounds such as solvents or actives, the molecules are placed randomly in the unit cell. In contrast, macromolecular compounds are divided into segments and 'grown' into the unit cell by placing each segment one by one. First, rotatable bonds of the polymer backbone are assigned defining the torsional degrees of freedom of the molecule. After placing the first segment of every chain molecule, M trial conformation (10 in this work) for the second segment of each molecule are generated providing a scan of the torsion angles of the polymer backbone. For every trial conformation $\kappa = 1, ..., M$, the potential energies $E_{0\kappa}$ and the corresponding Boltzmann weights $w_\kappa = \exp(-\beta E_{0\kappa})$ are calculated. Next, the probability P_κ (*cf.* eq 2.7) is determined, but instead of the partition function Q simply the sum of the Boltzmann weights of every trial configuration is used. Subsequently, the cumulative probability for the arbitrarily sorted set of trail conformations $\Pi_\kappa = \sum_{j=1}^{\kappa} P_j$ is calculated for each of the generated structures, that is $\Pi_0 = 0$ and $\Pi_M = 1$. Similar to the Monte Carlo Metropolis algorithm described in Section 2.2.1, Π_κ is compared with a random number between 0 and 1 drawn from a uniform distribution. Finally, if this random number lies between $\Pi_{\kappa-1}$ and Π_κ, the trial conformation is placed into the unit cell. This procedure is repeated until all segments of the polymer molecules are placed in the unit cell.

The constructed structure models were geometrically optimized followed by a simulated annealing procedure to refine the MC generated structures, that is finding lower energy structures showing higher probability P_κ. For this purpose, all structure models were equilibrated at $T = 300$ K using MD simulations along with the canonical (NVT) ensemble. Subsequently, the temperature was stepwise increased up to 1000 K and a later decreased back to 300 K. In each step, the temperature was increased (decreased) by 100 K followed by an equilibration for 5 ps. Next, the refined structure models were equilibrated for 100 ps using the isothermal-isobaric (NPT) ensemble at zero target pressure and $T = 300$ K by employing the Berendsen barostat and a further simulation using the Parrinello-Rahman barostat with a duration of 300 ps. Average cell parameters were evaluated for the last 200 ps of the NPT simulations. Finally, the unit cells were scaled to the average cell parameters obtained from NPT simulations and the structure models were again equilibrated for 250 ps employing the NVT ensemble with a target temperature of 300 K. Average properties such as CED were calculated from the last 200 ps of the NVT simulations. All MD simulations employed the module *Forcite* along with the Nosé-Hoover thermostat and a time step of 1 fs.

In case of the ISS for PEG, water as well as their mixture additional MD simulations for

temperatures ranging from 350 to 550 in 50 K steps were performed with a duration of 200 ps. For this purpose, NVT ensemble was used along with unit cell volume obtained from the NPT simulations at 300 K. The sampling of inherent structures was performed by applying structure optimizations every ps of the MD trajectories obtained for 400 K. This temperature is above T_g of PEG (250 K) [182]. The CED and pressures as a function of the temperature as well as the radial distribution functions of the coarse grained models calculated from the ISS are then used for parameterization of the thermodynamic models described in Section 2.1.4.

3   Atomic structure and properties of zero thermal expansion glass ceramics

Tuning the physico-chemical properties of $Ba_{1-m}Sr_mZn_{2-2n}Mg_{2n}Si_2O_7$ (BZS) solid solutions by simple variation of the chemical composition (m, n) allows straightforward tailoring of the materials properties of these glass ceramics. As mentioned in Section 1.2, the martensitic phase transition from the low (LT) to the high temperature (HT) phase and the thermomechanical properties are of particular importance for exploitation of BZS solid solutions as zero thermal expansion (ZTE) materials. First, prediction of the phase transition temperature T_t is addressed in Section 3.1 for localization of those chemical compositions at which the desired HT phase showing negative thermal expansion (NTE) along the crystallographic a-axis is thermodynamically stable at operation conditions. Subsequently, for chemical compositions showing sufficient thermodynamic stabilization of HT phase, the highly anisotroic, thermomechanical properties are characterized in order to facilitate the *in silico* optimization of the microstructure of BZS glass ceramics (Section 3.2).

3.1   Tunable martensitic phase transition temperature

As described in Chapter 2, the starting point for modeling physico-chemical properties are accurate atomistic structure models representing the (ensemble) average of the macroscopic structure and properties. In case of the BZS substitutional solid solutions, the exact position of substitutional ions, *e.g.*, of Sr^{2+} on the lattice sites of Ba^{2+} cannot be determined experimentally. This is connected with the configurational entropy S_{conf} leading to a macroscopic state showing an average of numerous possible atomic configurations, which in principle cannot be modeled using periodic boundary conditions [112]. Therefore, DFT calculations were applied to a set of atomic configurations using the experimentally determined crystal structure of the LT and HT phase of $BaZn_2Si_2O_7$ (BaZn) for evaluation how structure and thermodynamic properties depend on the atomic configuration and change with chemical composition (*cf.* Section 2.2.2). Of particular importance is the relative energy $\Delta E_0 = E_{0,HT} - E_{0,LT}$ or its configurational average $\Delta\overline{E_0}$, respectively, as central quantity for the thermodynamic modeling of the phase stability as a function of the chemical composition as described in Section 2.1.2. Please note that the chemical compositions are abbreviated as BaZn (m, $n = 0$), SrZn ($m = 1$, $n = 0$), BaMg ($m = 0$, $n = 1$) as well as SrMg ($m = 1$, $n = 1$) and the structure models for intermediate compositions are denoted as Sr($100m$)Mg($100n$) such that, *e.g.*, Sr50Zn and Sr50Mg25 refer to the chemical compositions ($m = 0.5$, $n = 0$) and ($m = 0.5$, $n = 0.25$), respectively.

Figure 3.1 shows the obtained lowest energy structures for the LT and HT phases of $Ba_{0.5}Sr_{0.5}Zn_2Si_2O_7$ (Sr50Zn) and $BaZnMgSi_2O_7$ (BaMg50). Comparison of cell parameters and relative energies ΔE_0 are summarized in Table 3.1. In addition, the change of the cell parameters a and c for $Ba_{1-m}Sr_mZn_2Si_2O_7$ as a function of the chemical composition obtained from

DFT simulations and experiments [22] are depicted in Fig. 3.2a. For all chemical compositions, a monoclinic crystal structure for the LT phase showing lower symmetry compared to the orthorhombic HT phase.
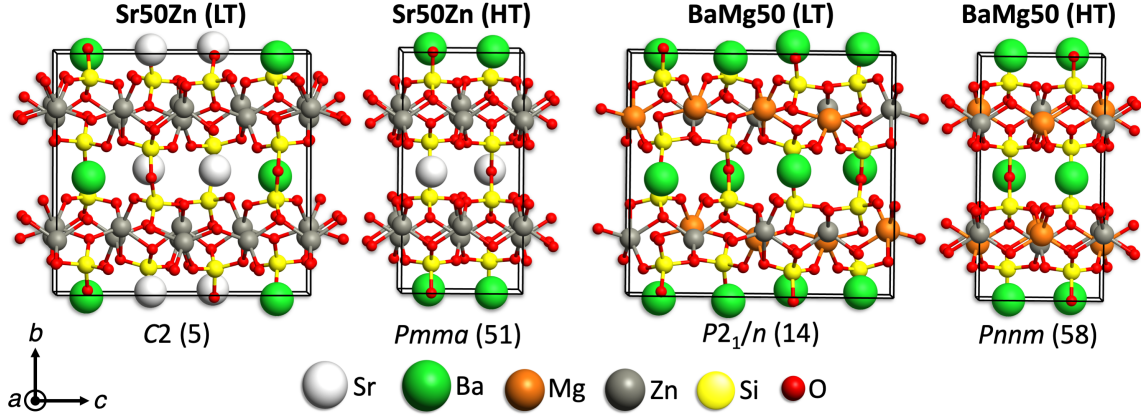

FIGURE 3.1: Lowest energy structures of the low (LT) and high temperature (HT) phase for $Ba_{0.5}Sr_{0.5}Zn_2Si_2O_7$ (Sr50) and $BaZnMgSi_2O_7$ (Mg50) obtained from DFT simulations.

The fundamental assumption for construction of the atomistic models is the formation of solid solutions, that is the basic crystal structure of $BaZn_2Si_2O_7$ (BaZn) remains unchanged by substitution of Ba^{2+} with Sr^{2+} and Zn^{2+} with Mg^{2+} (Fig. 3.1), respectively. Except from the crystallographic c-axis of the LT phase for $BaZn_{2-2n}Mg_{2n}Si_2O_7$ solid solutions, the lattice parameters change only slightly with the chemical composition. In addition, the cell parameters a and c vary almost linearly for the HT phase of $Ba_{1-m}Sr_mZn_2Si_2O_7$ in good agreement with experimental observations (Fig. 3.2a). For SrZn ($m = 1$, $n = 0$), no experimental values available since neither the LT nor the HT phase was obtained from glass crystallization [22]. The same trend was obtained for $BaZn_{2-2n}Mg_{2n}Si_2O_7$ solid solutions from both, DFT simulations and experiment [19, 21]. The almost linear change of lattice parameters of BaZn caused by substitution of Ba^{2+} and Zn^{2+} supports, according to Vegard's law [183], the assumption that indeed solid solutions as depicted in Fig. 3.1 are formed.

TABLE 3.1: Change of lattice parameters with respect to BaZn, space groups and relative energies at 0 K, ΔE_0 [kJ/mol], calculated using DFT simulations for BaZn, BaMg50 and Sr50Zn.

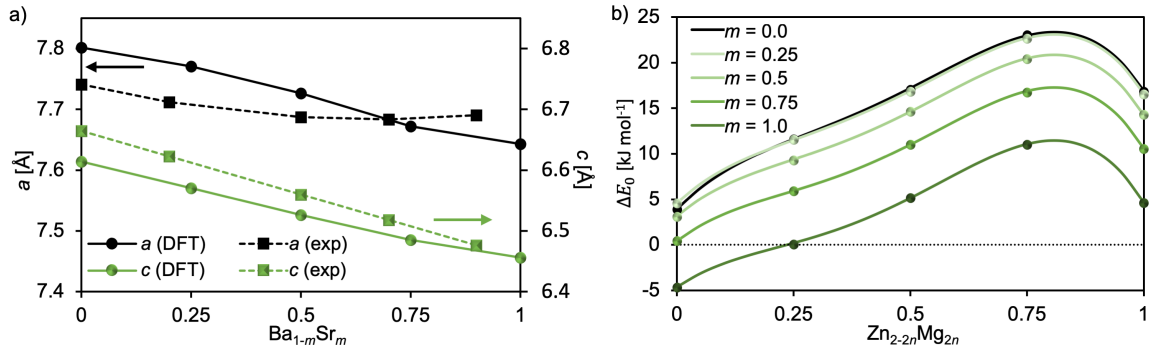| Model		Lattice parameters			Space group	ΔE_0
		a[Å]	b[Å]	c[Å]		
BaZn	LT	7.181	12.691	13.680	$C2/c$ (15)	3.9
	HT	7.812	12.956	6.614	$Cmcm$ (63)	
BaMg50	LT	-0.035	-0.088	0.087	$P2_1/c$ (14)	17.0
	HT	-0.052	0.025	0.027	$Pnnm$ (58)	
Sr50Zn	LT	-0.051	0.036	-0.257	$C2$ (5)	3.1
	HT	-0.095	-0.018	-0.086	$Pmma$ (51)	
Sr50Mg50	LT	-0.081	-0.090	-0.162	$P2_1$ (4)	14.7
	HT	-0.103	-0.005	-0.073	Pm (6)	

FIGURE 3.2: Change of a) lattice parameters a and c of the HT phase for $Ba_{1-m}Sr_mZn_2Si_2O_7$ calculated using DFT simulations in comparison with experimental (exp) values [22] and b) fit of the relative energies ΔE_0 of HT with respect to LT as a function of chemical composition (m, n).

In case of the $Ba_{1-m}Sr_mZn_2Si_2O_7$ solid solutions, all structure models constructed were geometrically optimized. This allows the calculation of the average cell parameters as well as the average relative energy $\Delta\overline{E_0}$ (*cf.* eq2.8). The differences between the average cell parameters and the ones calculate for the lowest energy structures are lower than 0.03 Å. Similarly, the deviation between ΔE_0 of the lowest energy configurations of the LT and HT phase and $\Delta\overline{E_0}$ are lower in 1 kJ/mol in all cases. These minor deviations support the assumption that ΔE_0 can be used for the thermodynamic modeling of T_t as a function of the chemical composition of BZS solid solutions. Due to the high number of possible atomic configurations for the LT phase of $BaZn_{2-2n}Mg_{2n}Si_2O_7$ solid solutions, geometry optimizations were only applied to a subset of structure models. Therefore, in order to estimate the difference of configurational entropy $\Delta S_{conf} = S_{conf,HT} - S_{conf,LT}$, the lattice energies obtained from single point calculations of the generated structure models were used (*cf.* eq 2.9). Since the LT and HT phase differ only in crystal symmetry (space groups, *cf.* Tab. 3.1), the free energy contributions $-T\Delta S_{conf}$ are only -1 kJ/mol (per formula unit) for $Ba_{1-m}Sr_mZn_2Si_2O_7$ and 2 kJ/mol for $BaZn_{2-2n}Mg_{2n}Si_2O_7$ solid solutions, respectively, assuming a glass crystallization temperature of 1200 K [184]. Such small free energy contributions, which are virtually independent of the actual values for m and n, can be assumed to be lower than DFT accuracy for calculation of ΔE_0. Consequently, ΔS_{conf} is assumed to be zero. Furthermore, the empirical correction of the harmonic vibrational free energy considers not only the effects anharmonic lattice vibrations on T_t but also includes the DFT error of ΔE_0 as well as the neglect of ΔS_{conf}.

The fit of relative energies ΔE_0 as a function of (m, n) to a quartic polynomial is depicted in Figure 3.2b showing very good agreement with DFT calculated values along with a mean absolute error (MAE) of 0.1 kJ/mol. For $\Delta E_0 \leq 0$ the HT phase is predicted to be thermodynamically stable for all temperatures and, thus, T_t is set to 0 K. For Sr^{2+} concentrations between $m = 0$ and 0.25, ΔE_0 remains virtually unchanged, yet considerably decreases for larger m. In contrast, ΔE_0 increases with increasing Mg^{2+} concentration n, except for the maximum at $n = 0.75$, which is about 6 kJ/mol higher compared to $n = 1$ and probably connected with the inaccuracy of DFT. Nonetheless, there is an obvious qualitative correlation of ΔE_0 with experimentally observed T_t [19, 21, 22], indicating that the calculation of ΔE_0 for other chemical compositions can indeed be used for prediction of T_t.

TABLE 3.2: Model parameters of composition dependent Debye temperatures $\Theta_{\mathrm{BaZn},i}$, Θ_1, Θ_2 [K] (*cf.* eqs 2.19) as well as anharmonicity parameter τ_{BaZn}, τ_1, τ_2 [K^{-1}] and (*cf.* eqs 2.20 and 2.21).

	$\Theta_{\mathrm{BaZn},1}$	$\Theta_{\mathrm{BaZn},2}$	$\Theta_{\mathrm{BaZn},3}$	Θ_1	Θ_2	τ_{BaZn}	τ_1	τ_2
LT	216.0	734.7	1399.2	56.14	8.88	-	-	-
HT	198.9	837.2	1328.0	54.15	10.50	-1.356 10^{-4}	4.192 10^{-5}	-6.456 10^{-4}

The obtained parameters for modeling of the composition dependent Debye temperatures $\theta_{i0}(m, n)$ (eq 2.19, $i = 1$-3) and the composition dependent anharmonicity parameter $\tau_{\mathrm{anh}}(m, n)$ (eqs 2.20 and 2.21) are shown in Table 3.2. In addition, Fig. 3.3a compares the harmonic vibrational density of states (VDOS) determined using phonon calculations at the DFT level with the approximated Debye VDOS (*cf.* eq 2.18) for the HT phase of BaZn and BaMg. The three Debye temperatures of the LT and HT phase, respectively, were determined by fitting the harmonic free energies calculated using the Debye VDOS to the values obtained from DFT simulations for BaZn, BaMg50, BaMg, Sr50Zn and SrZn. In all cases, the vibrational free energies calculated using the Debye model are in very good agreement with the DFT results along with a MAE of 1.3 kJ/mol. However, the corresponding T_{t} predicted by employing the harmonic approximation (HA) is, *e.g.*, for BaZn and BaMg 2070 and 1830 K, respectively, that disagree even qualitatively with the experimentally observed values of 553 and 1207 K [21]. Therefore, consideration of the effects of anharmonic lattice vibrations on the vibrational free energy A_{vib} is indispensable for reliable predictions of T_{t} of BZS solid solutions over a wide composition range.

The parameters of the empirical correction of the harmonic Debye model by using $\tau_{\mathrm{anh}}(m, n)$ (eqs 2.20 and 2.21) is determined by fitting the vibrational free energy of the HT phase $A_{\mathrm{vib,HT}}$ to experimentally observed T_{t} of the BZS solid solution series with $m = 0$ and $n = 0$. Figure 3.3b shows the resulting model calculations for T_{t} for obtained in comparison with experimentally determined values. In case of the substitution of Ba^{2+} by Sr^{2+} ($m > 0$, $n = 0$), only two close lying experimental are available for $m = 0.02$ and $m = 0.06$ with $T_{\mathrm{t}} = 543$ K and 473 K, respectively. For the latter, a mixture of the LT and HT phase was obtained from glass crystallization, while for higher Sr^{2+} concentrations ($m > 0.1$) only the HT phase evolves during crystallization and, consequently, no T_{t} could be observed [22]. An atomistic model for such low Sr^{2+} concentrations would require large unit cells and a vast number of calculations for localization of the lowest energy structure rendering simulations at the DFT level tremendously challenging. Therefore, values for of the polynomial fit of ΔE_0 (*cf.* Fig. 3.2) was used for the fit of anharmonic model for $A_{\mathrm{vib,HT}}$ in this case. In contrast, five experimentally determined T_{t} were used for the ($m = 0$, $n > 0$) solid solution series [21].

Largest deviation of T_{t} calculated using the derived model from experimental values are at $n = 0.75$ of about 100 K due to DFT error of ΔE_0 (see also Table 3.3). In order to estimate the uncertainty of model predictions, a fit of only two observed T_{t} for the ($m = 0$, $n > 0$) solution series was performed and represented as a shaded area in 3.3b corresponding to a value of ± 100 K. For comparison, an error in ΔE_0 of only 0.8 kJ/mol, which is assumed to be lower than the DFT accuracy, translates into a deviation of a polymorphous phase transition temperature of about 90 K with respect to the experimentally obtained value [24]. That is, even if only two T_{t} is experimentally available for calculation of the empirical correction, the deviation of the model predictions is in the same order of magnitude as the DFT accuracy. Therefore, the
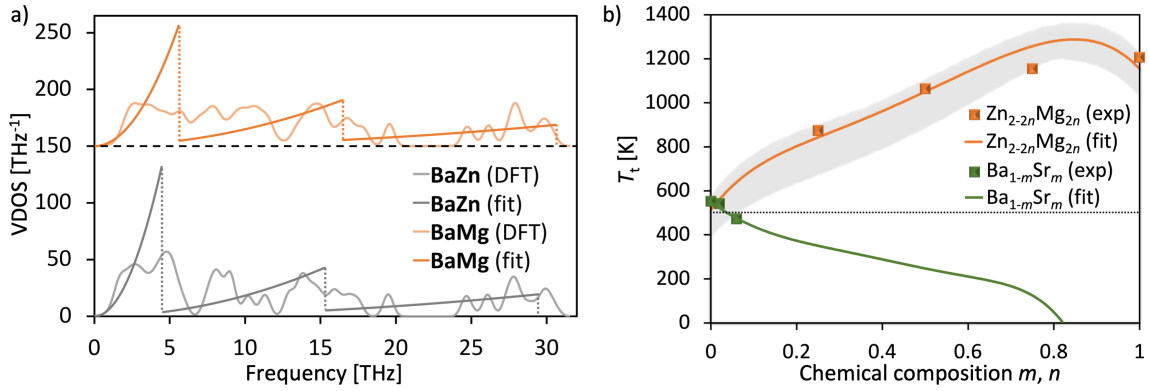
FIGURE 3.3: Modeling of a) the composition dependent vibrational density of states (VDOS) using the derived Debye model (eqs 2.18 and 2.19) of the HT phase for BaZn and BaMg compared to the DFT calculated VDOS and b) the phase transition temperatures (T_t) as a function of the chemical composition (m, n) along with experimentally observed T_t [21, 22] used for the model parameterization. The shaded area indicates the uncertainty of model predictions (see text). Below T_t of approximately 500 K (dotted line) only the HT phase was obtained from glass crystallization.

proposed procedure appears to be an efficient way to combine computationally inexpensive phonon calculations employing the HA with two experimental values for T_t to include the effects of anharmonic lattice vibrations, instead of performing computationally more demanding calculations such as *ab initio* molecular dynamics simulations. Moreover, as mentioned above for solid solutions with $m > 0.1$ and $n = 0$ only the HT phase emerges during glass crystallization and persists during cooling down to room temperature, which corresponds to a calculated T_t of about 500 K indicated by the dashed line in Fig. 3.3b. Therefore, it can be expected that for predicted T_t below 500 K only the HT phase is obtained from glass crystallization, while for $T_t > 500$ K only the LT phase should be present in the crystallized samples.

Table 3.3 summarizes calculated and experimentally observed T_t used for model parameterization [19, 22] as well as T_t for chemical compositions, which were not included in the least square fitting of the empirical correction of the harmonic $A_{vib,HT}$, namely Sr25Mg50, Sr50Mg50, Sr25Mg75 and Sr50Mg75 (provided by C. Thieme, K. Thieme and C. Rüssel). In addition, Figure 3.4a shows the results of model predictions for T_t as a function of the chemical composition of BZS solid solutions with m, n between 0 and 1. They range from 0 K at compositions close to SrZn upto 1283 K at $m = 0$ and $n = 0.82$. The latter is overestimated due to error in ΔE_0 (*cf.* Fig. 3.2). For Sr50Mg50 and for Sr25Mg75, the predicted T_t show very good agreement with the experimentally determined ones with differences of about 120 and 40 K, respectively. These deviations are approximately the same as the estimated uncertainty of ±100 K of the model predictions and in the same order of magnitude of the expected inaccuracy of DFT simulations. This indicates that the assumption of linear composition dependencies of $\theta_{i0}(m, n)$ and $\tau_{anh}(m, n)$ provide a good approximation for modeling of A_{vib} of BZS solid solutions.

Furthermore, a second phase was observed for Sr25Mg75 at 1114 K. In case of Sr50Mg75, only one phase transition at 1079 K was observed. For Sr25Mg50 no phase transition was detected, neither by employing DSC nor dilatometry. Since the derived thermodynamic model for A_{vib} assumes the formation of substitutional solid solutions, it considers only the continuous, linear dependence of the harmonic VDOS as well as of T_t of the previously known

TABLE 3.3: Comparison of phase transition temperatures T_t [K] obtained by theory (theo) and experiment (exp) for different chemical compositions (m, n) of $Ba_{1-m}Sr_mZn_{2-2n}Mg_{2n}Si_2O_7$.

Model	T_t (exp)	T_t (theo)
BaZn	550[a]	495
BaMg25	875[a]	840
BaMg50	1065[a]	1048
BaMg75	1156[a]	1253
BaMg	1207[a]	1142
Sr25Mg50	-[b]	707
Sr50Mg50	665 (DSC)[c]	547
Sr25Mg75	861 (Dil)[c]	821
	1114 (Dil)[c]	
Sr50Mg75	1079 (Dil)[c]	638

[a]Taken from ref. [21]

[b]No phase transition detected

[c]Provided by C. Thieme, K. Thieme and C. Rüssel

martensitic phase transition on the chemical composition. In addition, the model derivation included only the the solid solution series for substitutions of either Ba^{2+} by Sr^{2+} ($m > 0$, $n = 0$) or Zn^{2+} by Mg^{2+} ($m = 0, n > 0$). That is, neither a second phase transition at higher temperatures nor the effects of Sr^{2+}/Mg^{2+} cosubstitutions apart from the assumed linear composition dependence was considered in the model that could potentially lead to suppression of the phase transition in case of Sr25Mg50. Moreover, glass crystallization of BZS solid solutions yields defect containing crystallites showing local residual stresses and highly anisotropic microstructures [185] leading to the formation cracks that also influence the macroscopic properties of the glass ceramics [184]. In contrast, the employed thermodynamic model assumed perfect, single crystalline and stress free BZS solid solutions. Therefore, the employed procedure provides predictions of the martensitic phase transition temperature with an uncertainty of about ±100 K only if the influence of lattice defects and the microstructure on T_t is not too pronounced, which could also rationalize the hinderance of the phase transition in case of Sr25Mg50.

The corresponding contour plot of Fig. 3.4a is shown in 3.4b along with the chemical composition at which the LT (orange dots), HT (blue triangles) or mixtures of both phases (orange triangles) were obtained from glass crystallization, respectively. The empirical value for T_t of 500 K under which solely the HT crystallizes from glasses (dashed line in Fig. 3.3b) is also highlighted in Fig. 3.4b. Determination of the crystal phases used X-ray diffraction experiments provided by C. Thieme, K. Thieme and C. Rüssel and taken from previous studies [19, 22] (*cf.* Table 3.3). As mentioned above, for chemical compositions ($m > 0.1$, $n = 0$) only the HT phase is present in the crystallized glass samples, while a mixture of HT and LT was observed at ($m = 0.06$, $n = 0$). For the BZS solid solution series with $m = 0.5$ and $n > 0$, the crystallized samples contained only the HT phase upto $n = 0.25$. At $n = 0.35$ a mixture of LT and HT was observed along with a predicted T_t of approximately 500 K. If the Mg^{2+} concentration n is further increased only the LT phase crystallizes during the crystallization process. This applies also to

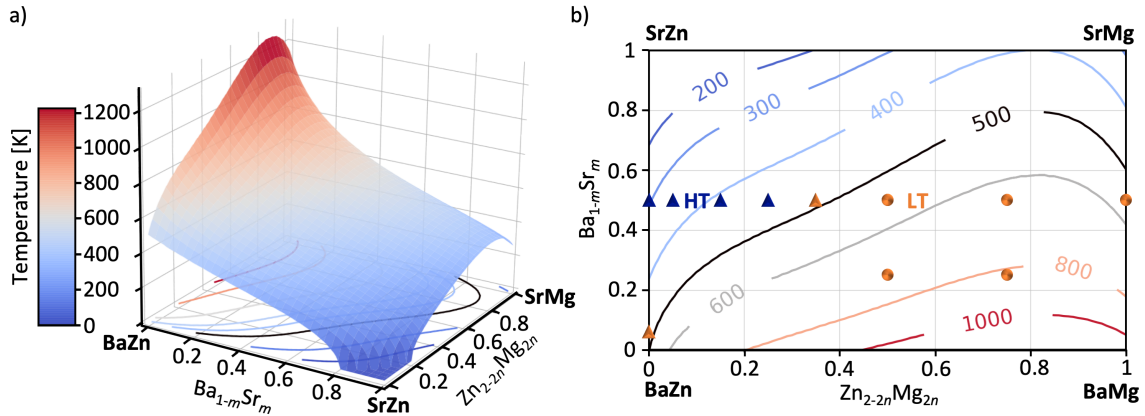the chemical compositions Sr25Mg50 and Sr25Mg75.

FIGURE 3.4: a) Plot of predicted phase transition temperatures as a function of the chemical composition. b) Contour lines of (a) along with compositions at which only the high temperature (HT) phase (blue triangles), only the low temperature (LT) phase (orange dots) and mixtures of both phases (orange triangle) were obtained by glass crystallization [19, 22].

The considerable decrease of both, the calculated ΔE_0 using DFT simulations and the experimentally observed T_t, with increasing Sr^{2+} concentration m clearly indicates that the HT is thermodynamically stabilized by substitution of Ba^{2+} with Sr^{2+}. Most likely, the HT phase emerges from glass crystallization at higher temperatures and transforms into the LT phase during cooling of the samples. For chemical compositions with predicted T_t below 500 K, the martensitic phase transition is probably kinetically hindered such that only the HT phase is observed at room temperature. For both samples with predicted T_t of about 500 K show a mixtures of the LT and HT phase. This is probably connected with small, local fluctuations of the chemical composition such that only a certain fraction of the HT crystallites transform into the LT phase during cooling of the sample. This allows the rapid localization of those chemical compositions at which the desired HT phase showing NTE can be obtained from glass crystallization as well as, despite certain limitations mentioned above, the rapid prediction of the corresponding phase transition temperature. In this way, promising chemical compositions can be determined for further experimental characterization and more demanding simulations, such as *ab initio* MD simulations or phonon calculations using the quasi-harmonic approximation, in order to provide a deeper understanding of the structure-property relations of this ZTE glass ceramics.

3.2 Anisotropic thermomechanical properties

For those chemical compositions at which the desired HT phase of BZS solid solutions is obtained from glass crystallization, the characterization of the thermomechanical properties is of fundamental importance for the targeted design of the glass ceramic microstructure. Since the substitution of Ba^{2+} by Sr^{2+} leads to considerable thermodynamic stabilization of the HT phase, the $Ba_{1-m}Sr_mZn_2Si_2O_7$ solid solution series was chosen along with $m = 0, 0.25, 0.5$ and 0.75 for investigation of the composition dependence of the thermomechanical properties.

TABLE 3.4: Elements of the elastic stiffness **C** [GPa] and compliance **S** [TPa^{-1}] tensor calculated using DFT simulations.

Model	C_{aa}	C_{bb}	C_{cc}	C_{ab}	C_{ac}	C_{bc}	S_{aa}	S_{bb}	S_{cc}	S_{ab}	S_{ac}	S_{bc}
BaZn	91	176	134	82	81	91	28	10	17	-6	-12	-3
Sr25Zn	88	177	137	81	81	91	30	10	17	-7	-13	-3
Sr50Zn	91	180	141	83	82	92	27	10	15	-7	-12	-3
Sr75Zn	83	183	145	81	81	92	33	10	15	-8	-13	-2

The composition SrZn ($m = 1$) is not considered here since neither the LT nor the HT BZS phase was obtained from glass crystallization [22].

The elements of the stiffness **C** as well as compliance **S** = **C**$^{-1}$ tensor are summarized in Table 3.4. In addition, Table 3.5 shows the corresponding elastic properties calculated using DFT simulations, namely the (Reuss) average bulk modulus K, Young's modulus Y_i and the linear compressibilities b_i along the crystallographic axes ($i = a, b, c$) [124]. For all chemical compositions highly anisotropic elastic properties were obtained, which are only weakly dependent on the chemical composition. While the crystallographic a axis shows the highest compressibility (**S** and b_i) or lowest stiffness (**C** and Y_i), respectively, the b axis is the least compressible one. With the exception of S_{bb} and S_{cc}, the compliance tensor **S** (and also **C**) shows no systematic change for $m = 0$, 0.25 and 0.5. Such small changes are expected to lie within the accuracy of the employed DFT simulations. This applies also the the bulk modulus K. However, for Sr75Zn ($m = 0.75$) a slightly higher value for S_{aa} was obtained yielding higher compressibility b_a of the crystallographic a axis showing NTE. In contrast, the b and c axis show a systematic decrease of the compressibility with increasing m.

Together with the heat capacity at constant volume C_V calculated using phonon calculations along with the harmonic approximation, the compliance tensor **S** shown in Table 3.4 and experimentally observed cell parameters are used for determination of the anisotropic thermal expansion $\alpha = (\alpha_a, \alpha_b, \alpha_c)^{\mathrm{T}}$ (*cf.* Section 2.1.3). Figure 3.5 shows the experimentally determined lattice parameters [19, 21, 22] along with DFT the calculated values ($T = 0$ K, crosses). Values for 103, 173 and 293 K were measured using X-ray diffraction experiments conducted by C. Thieme, K. Thieme and C. Rüssel. Due to the martensitic phase transition (*cf.* previous section), experimentally determined cell parameters are only above 550 K available in case of BaZn ($m = 0$).

TABLE 3.5: Bulk modulus (Reuss), Young's modulus [GPa] and linear compressibility [TPa^{-1}] calculated using DFT simulations.

Model	K	Y_a	Y_b	Y_c	b_a	b_b	b_c
BaZn	89	36	97	59	8.9	0.8	1.6
Sr25Zn	87	34	99	59	9.7	0.6	1.1
Sr50Zn	89	37	101	65	9.1	0.7	1.4
Sr75Zn	83	30	101	65	11.7	0.1	0.3

TABLE 3.6: Linear (γ_a, γ_b, γ_c) and average $\overline{\gamma}$ Grüneisen parameter obtained from least square fitting of α (eq 2.22) using the temperature dependent cell parameters of $Ba_{1-m}Sr_mZn_2Si_2O_7$ (Fig. 3.5).

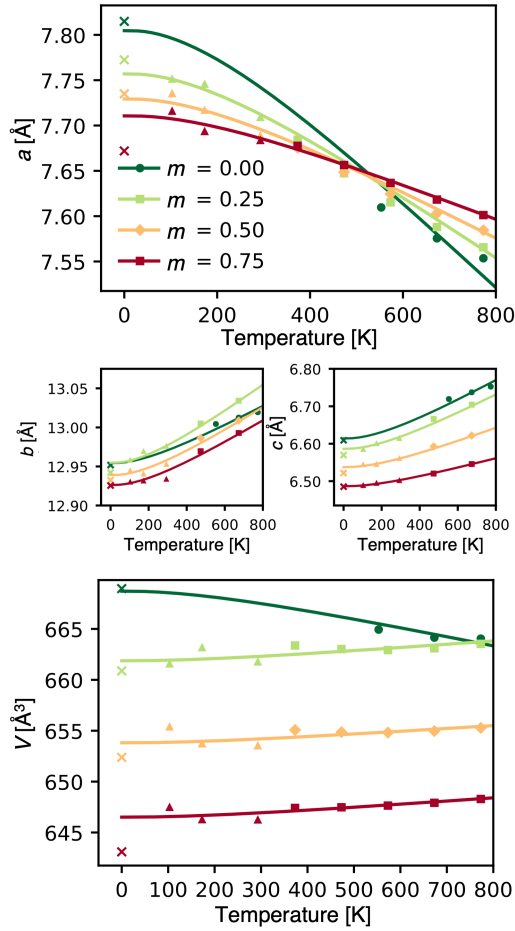| Model	γ_a	γ_b	γ_c	$\overline{\gamma}$
BaZn	-0.16	0.02	0.10	-0.11
Sr25Zn	0.01	0.18	0.23	0.04
Sr50Zn	0.01	0.15	0.18	0.03
Sr75Zn	0.03	0.15	0.15	0.04

FIGURE 3.5: Fit of the anisotropic thermal expansion α (eq 2.22) to DFT calculated cell parameters (T = 0 K, crosses) and experimentally determined lattice parameters as a function of temperature of $Ba_{1-m}Sr_mZn_2Si_2O_7$ solid solutions (triangles: provided by C. Thieme, K. Thieme, C. Rüssel; dots: ref. [21]; squares: ref. [22]; diamonds: ref. [19]).

The NTE of the crystallographic *a* axis lowers with increasing Sr^{2+} concentration *m*. The thermal expansion α_a at 300 K increases from -34×10^{-6}/K for Sr25Zn (-32×10^{-6}/K for BaZn) upto -19×10^{-6}/K for Sr75Zn. In contrast, the *c* axis shows pronounced positive thermal expansion that considerably deceases with increasing Sr^{2+} content. That is, α_c at 300 K is halved from 30×10^{-6}/K for BaZn to 15×10^{-6}/K for Sr75Zn. In contrast, α_b is virtually independent of the chemical composition with values ranging from 7 to 10×10^{-6}/K. The large anisotropy of both, elastic properties and thermal expansion, can lead to cracks and residual stresses in the microstructure of the glass ceramics depending on orientation of the crystallites. For example, in case of surface crystallization highly directional crystallite orientations were observed leading to undesired crack formation perpendicular to the *c* axis [185]. Therefore, knowledge of the anistropic elastic properties (Tab. 3.5) and the thermal expansion α as well as their dependence on the chemical composition provide vital input for continuum mechanics simulations, *e.g.*, using the finite element method [186, 187] for the targeted design of suitable microstructures to facilitate ZTE in the desired temperature range.

The fit of α to the cell parameters (Fig. 3.5) provides the linear Grüneisen parameters γ_i that are the adjustable parameters of the model (*cf.* Section 2.1.3). Table 3.6 shows the resulting linear and average Grüneisen parameters $\overline{\gamma}$, which are assumed to be independent of temperature. The average (macroscopic) Grüneisen parameter $\overline{\gamma}$ provides the relation between the volumetric thermal expansion, the bulk modulus K and the heat capacity C_V (*cf.* eq 2.15). The Grüneisen parameters for BaZn show no

clear correlation with the remaining ones, since the cell parameters of HT phase are only available for temperatures above 550 K resulting in erroneous Grüneisen parameters that are assumed to be temperature independent. For $m = 0.25$, 0.5 and 0.75, $\overline{\gamma}$ and γ_a are almost zero. On the other hand, γ_c is 0.23 for Sr25Zn and decreases with increasing Sr^{2+} concentration to 0.15 (Sr75Zn), while γ_b is slightly lower or equal to γ_c. Due to the small differences between γ_b and γ_c, the considerably lower thermal expansion of the b compared to the c axis is connected with its lower linear compressibility b_b. As can be seen from eq 2.22, the NTE in direction of the a axis is $\alpha_a \propto (\gamma_a S_{aa} + \gamma_b S_{ab} + \gamma_c S_{ac})$. Since the compliances S_{ij} (Tab. 3.4) show no significant change with chemical composition, the decrease of γ_b and γ_c with increasing m leads to the reduction of NTE of the crystallographic a axis. This indicates that the change NTE along the a axis is connected with, unlike b and c, the variation of vibrational states of the HT phase by substitution of Ba^{2+} with Sr^{2+}.

Figure 3.6 shows the harmonic vibrational density of states (VDOS) along with the partial VDOS for all elements of BaZn. In addition, the VDOS for Sr^{2+} and Ba^{2+} are shown for Sr25Zn, Sr50Zn and Sr75Zn. The partial VDOS of Ba^{2+} and Sr^{2+}, respectively, range from 0 to 7 THz in each case. While the Ba^{2+} VDOS shows its maximum at about 1.5 THz, the maximum value of the Sr^{2+} VDOS is approximately at 3 THz. Due to the lower mass of Sr^{2+} the VDOS is clearly shifted towards towards higher frequencies with increasing Sr^{2+} concentration m. In contrast, the remaining partial VDOS are almost independent of chemical compositions showing only smaller shifts to higher frequencies due to substitution of Ba^{2+} by Sr^{2+}.
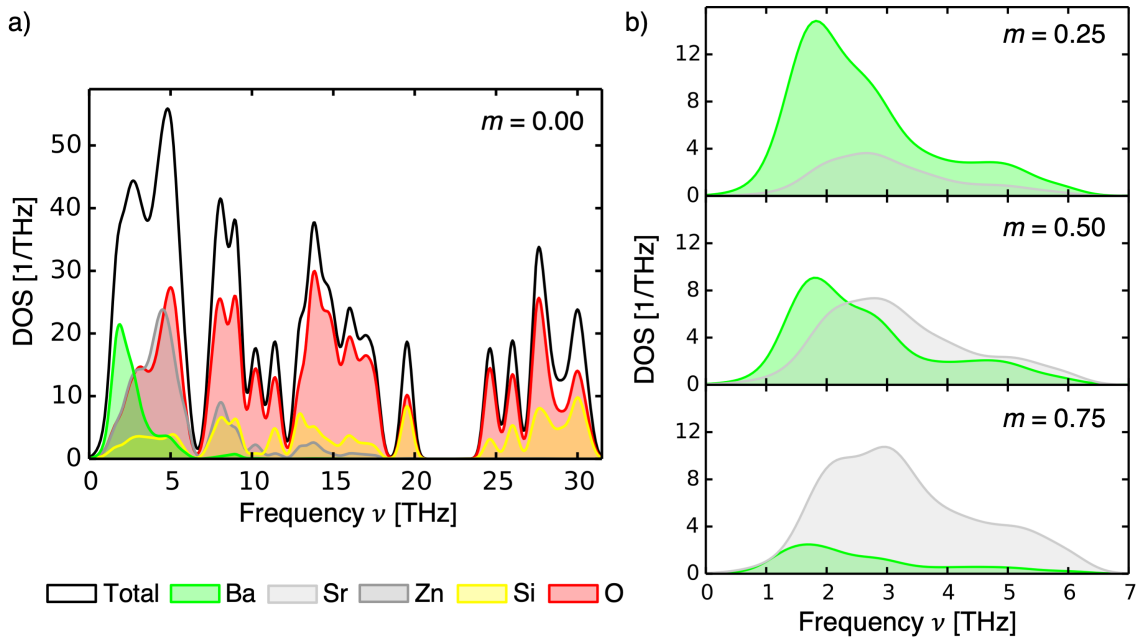
FIGURE 3.6: Total and partial vibrational density of states (VDOS) of $Ba_{1-m}Sr_mZn_2Si_2O_7$ solid solution for a) BaZn ($m = 0$) and b) partial VDOS of Ba^{2+} and Sr^{2+} as a function of the chemical composition.

In order to shed a light on the microscopic mechanisms of the NTE, additional phonon calculations using the quasi-harmonic approximation are applied to Sr50Zn. This provides the microscopic (mode) Grüneisen parameters $\gamma_{\mathbf{k}i}$ for each branch i at reciprocal lattice vector $\mathbf{k}$. Figure 3.7a depicts the temperature dependence of the corresponding average (macroscopic)

Grüneisen parameter weighted by the contribution of each vibrational mode to the heat capacity (eq 2.26). Up to 240 K the average (macroscopic) Grüneisen parameter γ_{DFT} is negative indicating volumetric contraction (*cf.* eq 2.15). Indeed, the experimentally observed cell volume of Sr50Zn reduces between 107 and 293 K (*cf.* Fig. 3.5). At 300 K γ_{DFT} is about 0.05 close to the averaged, temperature independent Grüneisen parameter $\bar{\gamma}$ of 0.03 obtained from the fit of α to the experimentally determined cell parameters (*cf.* Table 3.6). In the limiting case of high temperatures γ_{DFT} corresponds to the arithmetic average of all vibrational frequencies (*cf.* eq 2.26) yielding a value of 0.21 (dashed line in Fig. 3.7a).

Furthermore, the distribution of the average (macroscopic) γ_{DFT} calculated for frequency intervals of 1 THz at 300 K as well as number density $g\,(\gamma_{\mathbf{k}i})$ of the mode Grüneisen parameter $\gamma_{\mathbf{k}i}$ is shown in Figure 3.7b. Negative (average) γ_{DFT} were obtained at low frequencies between 0 to 5 THz along with a minimum value of -2.4 at 1.5 THz, that is the corresponding vibrational modes contribute most to the NTE. In the same frequency range lie the main contributions of the Ba^{2+} VDOS (maximum at about 1.5 THz) to the total VDOS, which is shifted towards higher frequencies when Ba^{2+} is replaced by Sr^{2+} (Fig. 3.6). For higher frequencies, γ_{DFT} is positive or close to zero. This rationalizes the reduction of the NTE along *a* direction with increasing Sr^{2+} concentration (Fig. 3.5). The majority the mode vibrational modes show positive Grüneisen parameter $\gamma_{\mathbf{k}i}$ as can be seen from $g\,(\gamma_{\mathbf{k}i})$ whose maximum value is at 0.5. Therefore, γ_{DFT} is negative at low temperatures turning positive due to thermal excitation of higher frequency modes with increasing temperature showing mostly positive $\gamma_{\mathbf{k}i}$.
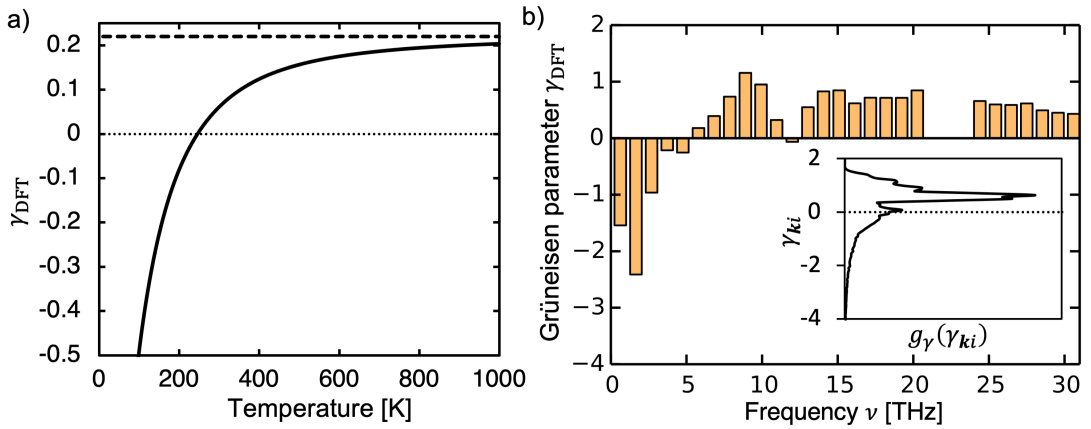
FIGURE 3.7: Average mode Grüneisen parameter of BaZn γ_{DFT} a) as a function of temperature and b) its distribution as a function of vibrational frequency ν calculated using frequency intervals of 1 THz and $T = 300$ K. The inset shows the number density of the mode Grüneisen parameter $\gamma_{\mathbf{k}i}$.

Atomic displacements along the polarization vector of the vibrational mode showing the most negative Grüneisen parameter $\gamma_{\mathbf{k}i}$ of -12.2 at a frequency of 1.3 THz is displayed in Figure 3.8a. A simplified sketch of the displacements of Si^{4+} and Zn^{2+} is depicted in 3.8b. Basic building blocks of the crystal structure of the HT phase are SiO_4 and ZnO_4 tetrahedra. They from two membered OSi–O–ZnO (**SOZ**) rings, which in turn form two sheets aligned in parallel to the *a-c* plane (see also Fig. 3.1). Two bridging oxygen ions connect both sheets by Si–O–Si bridges, while Ba^{2+} and Sr^{2+} ions are located between the sheets. The vibrational mode shows an oscillation in direction of the *b* axis in case of Ba^{2+} and Sr^{2+}, respectively, as well as a rocking

movement of the rigid Si–O–Si bridges within the *a*-*b* plane. The latter leads to deformation of the **SOZ** rings yielding contraction of the *a* axis (*cf.* Fig. 3.8b). Similarly, previous experimental studies using high temperature X-ray diffraction also concluded that the deformations of ZnO_4 and SiO_4 tetrahedra lead to the NTE of the *a* axis [188].

In order to qualitatively evaluate the effect of this vibrational mode on the crystal lattice, the stress tensor of the turning point **+1** with (arbitrarily chosen) atomic displacements of about 2 Å along its polarization vector at constant (zero pressure) cell volume was calculated. This yielded negative normal stress in *a* direction of about -2.8 GPa indicating that this mode clearly contributes to NTE along the *a* axis. In contrast, in *b* and *c* direction a normal stress of -0.02 and 2.4 GPa was obtained, respectively, showing that the vibrational mode has almost no effect on the *b* axis and contributes to the relatively large thermal expansion α_c.
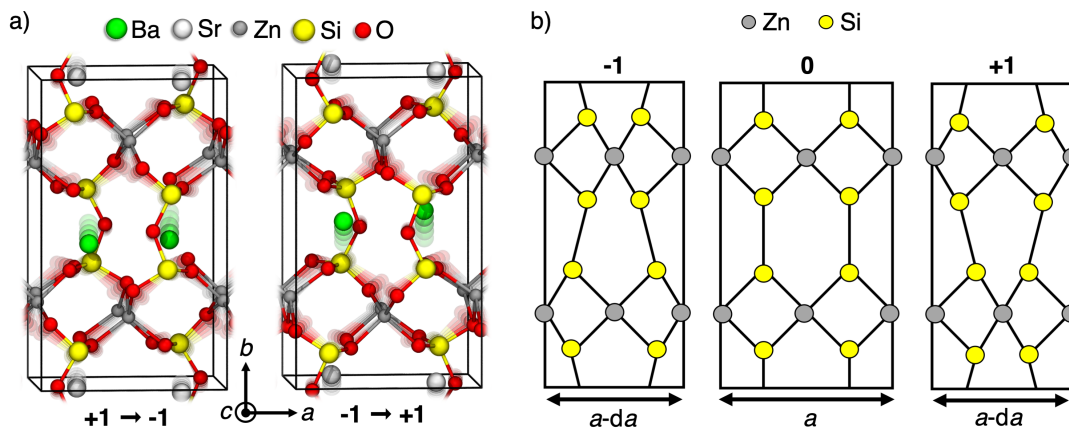

FIGURE 3.8: Representation of the vibrational mode showing the most negative mode Grüneisen parameter. a) Atomic displacements along its polarization vector between the turning points **-1** and **+1** and (b) simplified representation of the displacements of Zn and Si compared to their equilibrium position (**0**).

4 Structure prediction of Fe_2O_3 cluster and nanoparticles

In contrast to the BZS solid solutions described in the previous Chapter, for which experimentally determined structures were used as starting point, no previous knowledge of the precise atomic structure of small Fe_2O_3 gas phase clusters and nanoparticles is available from experiments. Therefore, prediction of the exact atomic structure using no assumptions except for constant chemical composition of stoichiometric Fe_2O_3 is the fundamental prerequisite for modeling of the formation processes and materials properties of Fe_2O_3 nanopowders. The results presented in this section were previously published in *Nanoscale* (RSC Publishing) [XI] and parts of the computational results and discussion of [XI] are adapted in this section.

4.1 Gas phase cluster by global structure optimization

Elucidation of atomic structures showing highest probability of being present in the macroscopic, gaseous state requires the localization of those atomic configurations κ showing lowest potential energy $E_{0\kappa}$ (*cf.* eq 2.7). For this purpose, the genetic algorithm [8] described in Section 2.2.1 was employed to find not only the global energy minimum but also several low lying local energy minima. Figure 4.1 shows the obtained global energy minima of $(Fe_2O_3)_n$ clusters with n = 1-10. It includes also structures with relative energies of less than 1 kJ/(mol Fe_2O_3) with respect to the global minimum and at least the two most stable ones. The cluster structures for n = 1-5 are taken from a previous publication [XII] and are included here for the sake of completeness. For these structure models with n = 1-5, additional DFT simulations were performed for calculation of the magnetic ground state (GS) [XII]. It was shown that the atomic structure and relative energies of the clusters isomers are virtually independent of the magnetic state and, therefore, DFT calculations of larger gas phase clusters assumed ferromagnetic (FM) states.

The two most stable isomers of Fe_2O_3 consist of a two-membered Fe-O ring and a terminal O atom. The planar, C_{2v} symmetric **1A** with its $^1B_1$ ground state is the global minimum. This structure has been reported as the most stable for Fe_2O_3 [59, 60] and $Fe_2O_3^-$ [55]. The second most stable isomer is the angled **1B** with the $^3A''$ GS, similar to the most stable configuration of the quartet GS of $Fe_2O_3^+$ [56]. The global minimum **2A** of $(Fe_2O_3)_2$ with its antiferromagnetic (AF) $^1A_2$ GS assumes the adamantane-like C_{2v} symmetric structure. The open sheet-like, C_2 symmetric **2B** with the ^{11}B GS consists of five fused two-membered Fe-O rings and is 30.6 kJ/(mol Fe_2O_3) higher in energy. Both **2A** and **2B** have been reported as the most and the second most stable structure of $(Fe_2O_3)_2$, respectively [61, 62]. However, these studies predicted either a ferrimagnetic, C_{3v} symmetric [61] or a FM, T_d symmetric $^{21}A_1$ GS [62] for **2A** and a FM, C_{2h} symmetric $^{21}B_g$ GS for **2B**. For $(Fe_2O_3)_2^-$ an AF state of **2A** was reported as the most stable spin configuration [54].

1A $^1B_1$ (C_{2v}) **1B** $^3A''$ (C_s) **2A** $^1A_2$ (C_{2v}) **2B** ^{11}B (C_2)   **3A** ^1A (C_1) **3B** $^1A'$ (C_s)   **4A** ^1A (C_1) **4B** ^1A (C_1)
            (+18.0)   (+30.6)   (+15.1)   (+4.0)

5A ^1A (C_1) **5B** ^{11}A (C_1)   **6A** $^{61}A_g$ (C_{2h}) **6B** ^{61}A (C_1)   **7A** $^{71}A''$ (C_s) **7B** ^{71}A (C_1)
            (+7.3)   (+0.4)   (+0.7)

8A ^{81}A (C_2) **8B** ^{81}A (C_1) **8C** $^{81}A'$ (C_s) **8D** ^{81}A (C_1)   **9A** $^{91}B_2$ (C_{2v}) **9B** $^{91}A'$ (C_s)
                (+0.4)   (+0.5)   (+0.7)   (+5.2)

10A ^{101}A (C_1) **10B** ^{101}A (C_1) **10C** ^{101}A (C_1) **10D** $^{101}A'$ (C_s)
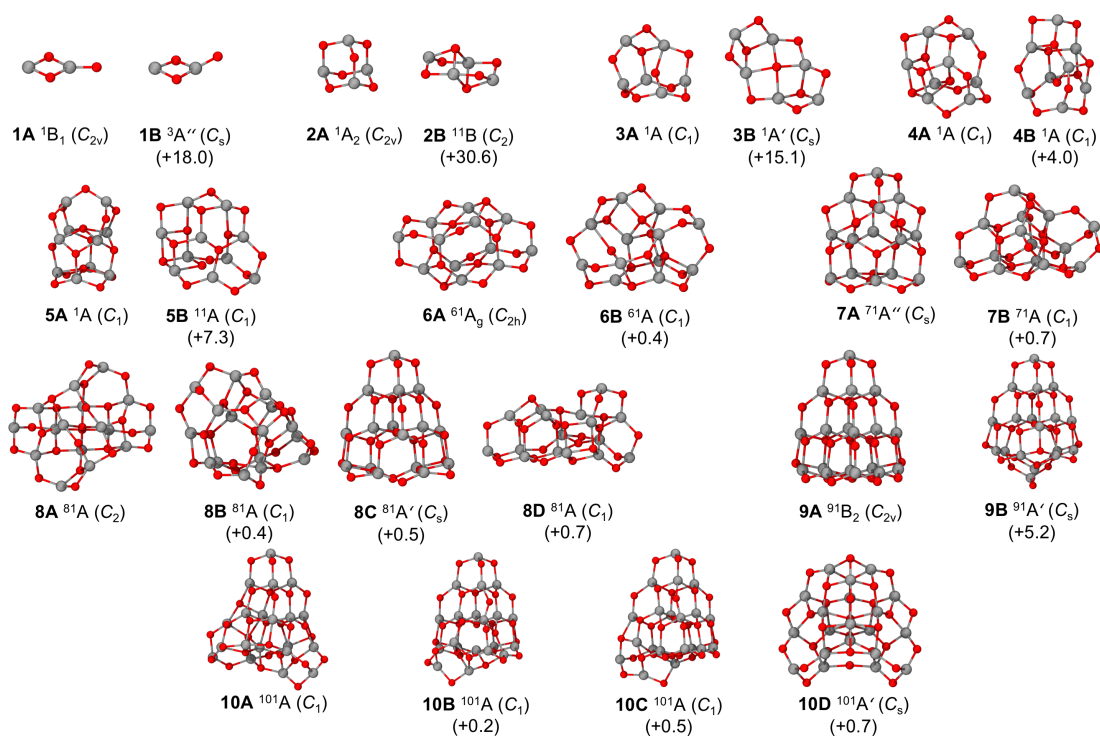   (+0.2)   (+0.5)   (+0.7)

FIGURE 4.1: Low-energy structures of $(Fe_2O_3)_n$ clusters with $n = 1$-10. Relative energies with respect to the global minimum are given in parentheses [kJ/(mol Fe_2O_3)] [XI]. Fe grey, O red.

The global minimum of $(Fe_2O_3)_3$ is the compact, C_1 symmetric **3A** with the AF GS. The second most stable C_s symmetric **3B** with the ^1A GS is an open, sheet-like structure containing exclusively two-membered Fe-O rings. It is 15.1 kJ/(mol Fe_2O_3) less stable than the global minimum. The two most stable isomers **4A** and **4B** of $(Fe_2O_3)_4$ are compact, C_1 symmetric structures with the AF GS and relative energy difference of only 4 kJ/(mol Fe_2O_3). For $(Fe_2O_3)_5$ the tower-like **5A** with the AF GS is the global minimum. The second most stable compact **5B** with its ferrimagnetic ^{11}A GS is 7.3 kJ/(mol Fe_2O_3) higher in energy.

Starting from $n = 6$ all $(Fe_2O_3)_n$ clusters contain the tetrahedral adamantane-like (TAL) structural element similar to **2A**. The global minimum of $(Fe_2O_3)_6$ is the C_{2h} symmetric **6A** build up of a central cage unit fused with two TAL units. The next most stable C_1 symmetric, compact **6B** is only 0.4 kJ/(mol Fe_2O_3) less stable than **6A**. Similarly, $(Fe_2O_3)_7$ shows two low energy isomers **7A** and **7B** that are separated by only 0.7 kJ/(mol Fe_2O_3). The global minimum **7A** of $(Fe_2O_3)_7$ is C_s symmetric and consists mainly of two- and three-membered Fe–O rings, with two of the three-membered rings bridged by one O atom. **7B** is a compact structure with no symmetry elements.

For $(Fe_2O_3)_8$ the global structure optimization procedure yields four isomers with relative energies within less than 1 kJ/(mol Fe_2O_3). The C_2 symmetric **8A** is the most stable structure. Among the higher energy isomers **8C** exhibits C_s symmetry and resembles the structure of **7A**. **8B** and **8D** have no symmetry elements.

In contrast to $(Fe_2O_3)_8$ the two most stable isomers **9A** and **9B** of $(Fe_2O_3)_9$ are energetically well separated with a relative energy difference of 5.2 kJ/(mol Fe_2O_3). The TAL unit can be considered as the main building block of both clusters. **9A** belongs to the symmetry point

group C_{2v} and has nearly tetrahedral structure. This structure bears a resemblance to **7A** and **8C**. The next most stable **9B** shows a lower C_s symmetry but very similar structure. In case of $(Fe_2O_3)_{10}$ the global optimization procedure yields four structures with relative energies below 1.0 kJ/(mol Fe_2O_3), all consisting mainly of the TAL building units.
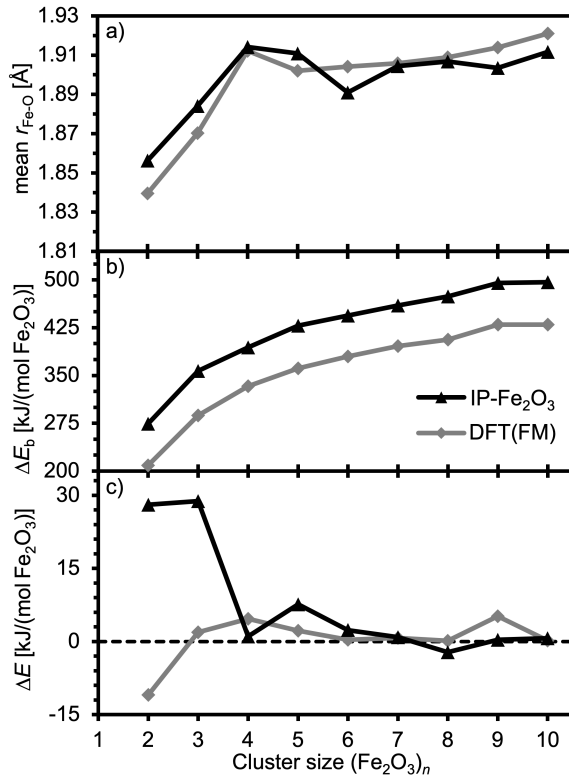

As a general feature the most stable $(Fe_2O_3)_n$ clusters assume compact structures with little or no symmetry. One exception is the nearly T_d symmetric TAL unit of **2A**. For n = 2-5 the clusters contain mainly two and three-membered Fe-O rings. Some isomers, in particular those with no symmetry elements contain also larger Fe-O rings, *e.g.*, **3A**. Starting from n = 5 the clusters start to assume increasingly tetrahedral shape with TAL unit as the main building block. However, the small energy differences between different isomers of the same cluster size make precise structural assignment for larger $(Fe_2O_3)_n$ clusters difficult. In addition, only the potential energy minima of the gas phase clusters were considered here so far. For evaluation of the thermodynamic stability of the obtained isomers at elevated temperatures, also vibrational, translational as well as rotational free energy contributions have to be considered (*cf.* Section 2.1.1). The located low energy structures provide the basis for such simulations as well as for modeling of their physico-chemical properties.

Figure 4.2: Comparison of IP-Fe2O3 and DFT results for ferromagnetic (FM) states for $(Fe_2O_3)_n$ clusters with n = 2-10: (a) average Fe-O bond lengths, r_{Fe-O}, (b) binding energies, ΔE_b, of the most stable clusters and (c) relative stability, ΔE, of the two lowest energy isomers (nA and nB, *cf.* Fig. 4.1) [XI].

Essential factor that determines the reliability of the structure predictions is the accuracy of the employed interatomic potential functions IP-Fe$_2$O$_3$, which were derived from simulations of the bulk Fe$_2$O$_3$ polymorphs at the DFT level (refs. [68] and [XI]). Even though the IP-Fe$_2$O$_3$ proved to accurately describe structure, relative phase stability and mechanical properties of the bulk Fe$_2$O$_3$ polymorphs, further evaluation of their accuracy for description of the atomic structure and properties of small clusters is indispensable for proper structure predictions. Figure 4.2 summarizes the main IP-Fe$_2$O$_3$ and DFT results for $(Fe_2O_3)_n$ clusters with n = 2-10: mean Fe–O bond lengths, binding energies of global minimum structures and relative stability of the two lowest energy isomers (nA and nB, *cf.* Fig. 4.1) for each cluster size. For the sake of completeness DFT results for the FM state of $(Fe_2O_3)_n$ clusters with n = 2–5 are included taken from [XII].

The transferability and reliability of the IP-Fe$_2$O$_3$ is demonstrated by the very good agreement of structural parameters with those obtained at the DFT level. For $(Fe_2O_3)_n$ clusters with

n = 2-5 the mean Fe–O bond lengths deviate less than 0.02 Å (Fig. 4.2a) between IP-Fe$_2$O$_3$ and the DFT results. In addition, the general trend of increasing Fe–O bond distances with increasing cluster size is very well reproduced by IP-Fe$_2$O$_3$.

Figure 4.2b shows the cluster size dependence of binding energy, ΔE_b, for the lowest-energy structures. It shows only small variation with the cluster size. The IP-Fe$_2$O$_3$ results are in a good agreement with the DFT values and show a constant shift of about 75 kJ/(mol Fe$_2$O$_3$) towards higher binding energies. IP-Fe$_2$O$_3$ also properly reproduces the monotonic increase of ΔE_b with increasing cluster size.

Figure 4.2c compares the relative energies ΔE of the two most stable (Fe$_2$O$_3$)$_n$ isomers calculated using IP-Fe$_2$O$_3$ and DFT. In case of n = 2 and 3 large deviations between IP-Fe$_2$O$_3$ and the DFT results for FM states were obtained. However, for the calculated magnetic GS the deviation is less than 15 kJ/(mol Fe$_2$O$_3$) [XII]. Such deviations for small clusters are not unexpected since the training set of IP-Fe$_2$O$_3$ contains only bulk structures. However, the agreement between IP-Fe$_2$O$_3$ and DFT is very good, within 5 kJ/(mol Fe$_2$O$_3$), for cluster sizes n > 3. In addition, as mentioned above, the relative energies are almost independent of the precise spin state for gas phase clusters with n > 3 [XII]. This supports our approach for determination of low-energy cluster structures employing GA in combination with IP-Fe$_2$O$_3$ followed by structure refinement at the DFT level assuming FM states.

These findings demonstrate that IP-Fe$_2$O$_3$ can accurately describe the structures and relative stabilities of both small (Fe$_2$O$_3$)$_n$ clusters and bulk Fe$_2$O$_3$ [68]. Therefore, one can expect that IP-Fe$_2$O$_3$ is also well suited for simulations of larger (Fe$_2$O$_3$)$_n$ NP at an intermediate length scale between clusters and bulk material.

4.2 Nanoparticles: crystallization and atomic structure

Due to the vast number of energetically close lying local minima of larger gas phase cluster and nanoparticles makes the localization of the actual global minimum by employing the genetic algorithm meaningless. Instead, predictions of the precise atomic structure of larger Fe$_2$O$_3$ nanoparticles (NP) can be achieved by using MD simulations combined with the simulated annealing procedure (*cf.* Section 2.2.1), that is, by the simulated crystallization of the NP starting from an equilibrated molten state. This procedure was applied to (Fe$_2$O$_3$)$_n$ structures with n = 80, 282 and 1328, which correspond to NP with diameters of 1 (**NP1**), 3 (**NP3**) and 5 nm (**NP5**), respectively.

The results of the simulated crystallization for **NP5** are depicted in Figure 4.3 including temperature dependence of potential energy ΔE_{0kappa} and coordination number (CN) distributions of Fe and O atoms. During the phase transition from the liquid to solid state the corresponding latent heat is released from the system. This can be seen as a sudden drop of potential energy of **NP5** between 1235 and 1215 K (Fig. 4.3a), yielding the melting temperature of about 1225 K. This value is significantly lower than the melting and decomposition point of bulk Fe$_2$O$_3$ (1835 K). This size-dependent melting point depression of nanoparticulate materials connected to their large specific surface area is a well-know phenomenon [189]. Using the calculated α-Fe$_2$O$_3$ melting temperature of 2025 K the melting point depression for **NP5** is about 800 K. This value is probably somewhat overestimated due to high cooling and heating rates of **NP5** and bulk α-Fe$_2$O$_3$, respectively, during our MD simulations.
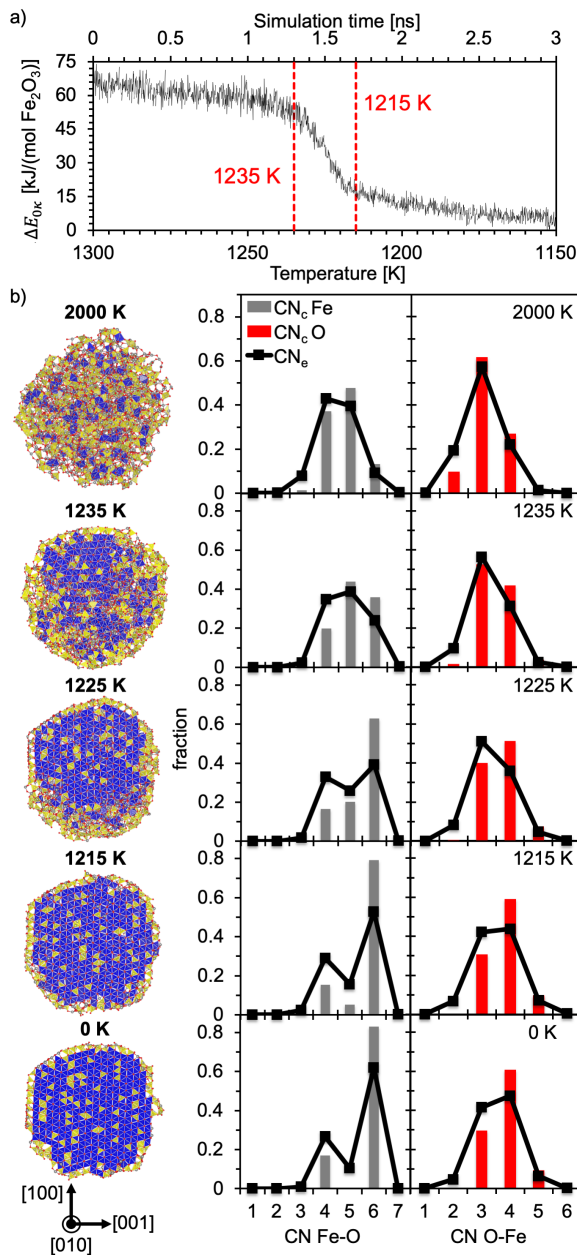
FIGURE 4.3: MD simulation of the crystallization process of **NP5**: (a) change of the potential energy ($\Delta E_{0\kappa}$) at the melting point and (b) coordination number (CN) distribution of Fe and O atoms, respectively, as a function of temperature. CN distributions are calculated for the core (CN_c) and the entire **NP5** (CN_e). For each temperature cross-sections ((010) plane of the final ϵ-Fe_2O_3 crystallite) are shown highlighting Fe atoms with octahedral (blue) and tetrahedral (yellow) coordination [XI].

The structural evolution of **NP5** during crystallization is shown in Figure 4.3b along with its cross-sections along [010] direction of the final ϵ-Fe_2O_3 crystal and temperature dependence of the coordination number distribution for Fe and O atoms. To facilitate comparison with bulk Fe_2O_3 polymorphs and discern structure differences between the inner and surface parts of **NP5** the CN distribution is evaluated separately for the core part (4 nm in diameter) and the whole **NP5**, denoted as CN_c and CN_e, respectively. In general, CN_e is shifted towards lower values due to a larger number of low-coordinated surface atoms. Equilibration of the initial spherical cuts of bulk Fe_2O_3 for 1 ns at 2000 K is sufficient to generate melted configurations that are independent of the initial structure, which was verified by two independent simulated annealing procedures starting from spherical cutouts of α- and γ-Fe_2O_3 yielding virtually the same results [XI]. At the starting temperature of 2000 K, the CN distribution shows mainly four- and five-fold coordinated Fe as well as three-fold coordinated O atoms. Decreasing temperature increases the mean CN_e from 3.9 and 3.0 at 2000 K to 5.3 and 3.6 at 0 K for Fe and O atoms, respectively. At 1235 K the corresponding NP cross-sections indicate beginning of crystallization with a nucleation center forming close to the NP surface. Compared to 2000 K both CN_e and CN_c distributions show an increased fraction of six-fold coordinated Fe and four-fold coordinated O atoms. In the temperature range from 1235 to 1225 K advancing crystallization transforms five-fold coordinated Fe atoms to six-fold coordinated ones and three-fold coordinated O atoms into four-fold coordinated ones. For temperatures between 1225 and 1215 K CN distributions show a significant reduction of five-fold coordinated Fe and emergence of five-fold coordinated O atoms. In contrast, the fraction of four-fold coordinated Fe atoms

remains virtually constant. The CN histograms for temperatures below 1215 K show no significant structural changes indicating complete crystallization. The somewhat irregular distribution of four-fold coordinated Fe atoms seen in the cross-section at 0 K arises from the presence of defect sites within the NP core.

Comparison of structural characteristics of the final **NP5** with bulk Fe_2O_3 polymorphs indicates that it consists of a single, albeit imperfect ϵ-Fe_2O_3 crystal. Analysis of CN_c yields 0.17 and 0.83 as fractions of Fe atoms with tetrahedral and octahedral coordination, respectively (*cf.* Fig. 4.3b, 0 K). These values are close to the fractions of four- (0.25) and six-fold (0.75) coordinated Fe atoms in bulk ϵ-Fe_2O_3. In contrast, γ-Fe_2O_3 contains a considerably higher fraction (0.375) of Fe atoms in tetrahedral coordination and α- as well as β-Fe_2O_3 contain exclusively six-fold coordinated iron. Furthermore, CN_c distribution shows presence of five-fold coordinated O atoms which are a unique structural feature of ϵ-Fe_2O_3. Deviations from the ideal CN distribution of ϵ-Fe_2O_3 are related to lattice defects present in **NP5** such as vacancies and dislocations. Similar deviations of CN fractions due to lattice disorders within nanoparticulate ϵ-Fe_2O_3 were also reported in experimental studies [190].
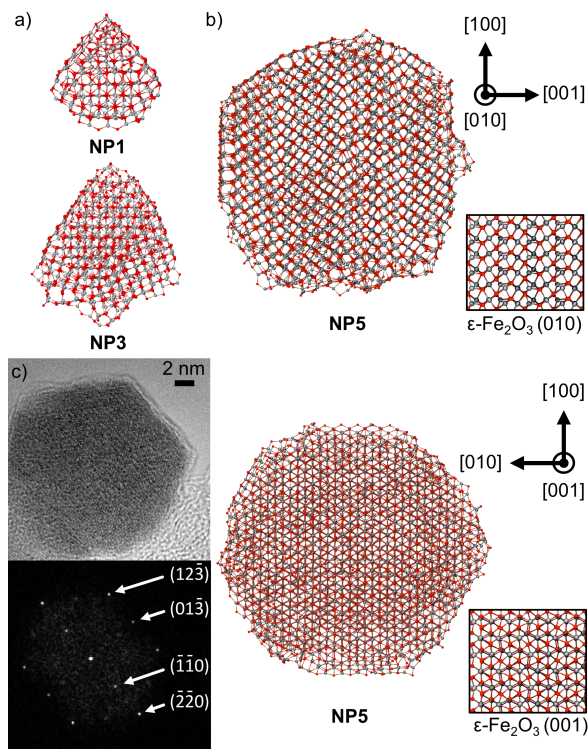
FIGURE 4.4: Structure of $(Fe_2O_3)_n$ nanoparticles: (a) **NP1** ($n = 80$) and **NP3** ($n = 282$), (b) comparison of **NP5** ($n = 1328$) with two different lattice planes of ϵ-Fe_2O_3 and (c) high-resolution TEM micrograph of a LAVA synthesized ϵ-Fe_2O_3 NP and its indexed Fourier transform (ϵ-Fe_2O_3, zonal axis $[\bar{3}31]$). The coordinate systems refer to the NP orientation [XI]. Fe grey, O red.

The most stable structures of **NP1**, **NP3** and **NP5** determined by the simulated crystallization procedure are depicted in Figure 4.4. For **NP5**, two orientations are shown along with two lattice planes of ϵ-Fe_2O_3 (Fig. 4.4b). Figure 4.4c shows a high-resolution transmission electron microscopy (TEM) micrograph of a 18 nm Fe_2O_3 NP prepared by laser vaporization (LAVA) of Fe_2O_3 raw powders [191] (results provided by H.-D. Kurland, J. Grabow and F. A. Müller).

The most stable configurations of Fe_2O_3 NP with 1 (**NP1**) and 3 nm (**NP3**) diameter show tetrahedral, wedge-like morphology (Fig. 4.4a) also present in smaller $(Fe_2O_3)_n$ clusters, such as **7A**, **8C**, **9A**, **9B** and **10A** (*cf.* Fig. 4.1). This particular shape can be rationalized by the presence of a large number of the TAL $(Fe_2O_3)_2$ building blocks forming a surface layer and a high surface-to-volume ratio of **NP1** and **NP3**. This is different in case of **NP5** that consists of a single crystalline, hexagonally shaped domain. In order to investigate the reproducibility of the crystallization process of **NP5** we repeated the procedure for several independent initial configurations. In all cases similar NP structures were obtained that are in a narrow energy window, less than 9 kJ/(mol Fe_2O_3) compared to **NP5**.

The final confirmation comes from the comparison of **NP5** with Fe_2O_3 nanoparticles synthesized in the LAVA process. Figure 4.4c displays a high-resolution TEM micrograph of such an NP with a diameter of about 18 nm showing the typical hexagonal morphology as well as the corresponding Fourier transform (FT). The lattice planes are visible throughout the whole particle, suggesting a single crystalline structure although the presence of defects cannot be ruled out. The FT of the lattice fringes was indexed according to the structural model of Tronc *et al.* [190] and identifies the NP as ϵ-Fe_2O_3 aligned along its $[\bar{3}31]$ axis. Our earlier study shows that larger Fe_2O_3 NP with diameters in the range of 50 nm can also display octagonal morphology [191]. The hexagonal shape of the LAVA synthesized Fe_2O_3 NP is very well reproduced by the results of simulated crystallization of **NP5** (Fig. 4.4b). Apart from the NP morphology, the simulated annealing procedure applied along with IP-Fe_2O_3 provide detailed insights into the atomic structure of Fe_2O_3 NP, which can be used for future theoretical studies of the thermodynamic and magnetic properties of these NP.

An earlier study of LAVA synthesized Fe_2O_3 nanopowders reported formation of different ratios of ϵ-Fe_2O_3 and γ-Fe_2O_3, depending on oxygen concentration in the condensation atmosphere [191]. The formation of the two phases is connected with their very similar stability as indicated by the small differences of the lattice energies between ϵ-Fe_2O_3 and γ-Fe_2O_3 of less than 1 kJ/mol calculated at the DFT level [XI]. In addition, the condensation of both phases was attributed to differences in the nucleation kinetics due to the presence of remarkably stable iron-ozone complexes. They act as precursors for octahedrally coordinated Fe sites upon rapid condensation and solidification of nanoparticles. Therefore, higher concentration of ozone in oxygen-rich condensation gas leads to an increased amount of ϵ-Fe_2O_3 with a larger number of octahedrally coordinated Fe atoms. In contrast, oxygen-poor atmosphere results in formation of a higher fraction of γ-Fe_2O_3 containing significantly less octahedral Fe sites. Strong dependence of ϵ-Fe_2O_3 content on experimental condition was also reported for other synthetic routes [41]. The appearance of only ϵ-Fe_2O_3 phase during simulated crystallization of **NP5** can be rationalized by the absence of kinetic factors influencing the nucleation process. All simulated crystallizations were performed for stoichiometric Fe_2O_3 systems starting from a well equilibrated, molten state. In contrast, NP formation by the rapid condensation of LAVA generated plasma is a non-equilibrium process that involves different non-stoichiometric gas phase species present during nucleation. This can result in formation of thermodynamically metastable phases [191]. However, in the present case the very good agreement between results of simulated crystallization of **NP5** and structure analysis of LAVA generated Fe_2O_3 NP provides the first direct indication that ϵ-Fe_2O_3 may be thermodynamically the most stable phase in this size range. The significant melting point depression of 800 K found in this study provides explanation for thermal instability of small ϵ-Fe_2O_3 NP observed by several authors [41] due to sintering and formation of larger agglomerates favoring conversion to α-Fe_2O_3. Indeed, it has been reported [41] that restricting growth of Fe_2O_3 NP by isolation in a SiO_2 matrix [192] or special synthesis conditions [43] significantly enhances stability of the ϵ-Fe_2O_3 phase.

5 Polymer solubility predictions by atomistic simulations

5.1 Prediction of atomic structure and properties

For reliable predictions the thermodynamic compatibility of low-molecular weight compounds based on the calculation of the free energy of mixing two prerequisites have to be fulfilled. First, sufficiently accurate calculations of the physico-chemical properties are needed, such as cohesive energy density c_i (CED) and pressures from atomistic simulations. The second requirement is the parameterization of appropriate thermodynamic models by employing the calculated CED and pressures, respectively. Two models presented in Section 2.1.4 are applied, the Flory-Huggins (FH) theory using constant and composition dependent interaction parameters as well as the perturbed hard sphere chain (PHSC) equation of state (EOS). Please note that in the following the indices $i, j = 1$ refer to the polymers PEG and PLA, respectively, while $i, j = 2$ are used for low molecular weight compounds such as solvents.

5.1.1 Accuracy of atomistic simulations

As described in Section 2.2.1 and 2.2.4, a sufficiently large set of points in phase space (atomic configurations and momenta) has to be sampled by atomistic simulations in order to obtain reproducible values of the macroscopic, thermodynamic quantities. For this purpose, a combination of Monte-Carlo (MC) and molecular dynamics (MD) simulations is applied using two different sampling procedures, denoted here as direct sampling (DS) and inherent structure sampling (ISS). While MC simulations are used for generation of polymer conformations, the sampling of the physico-chemical properties is achieved by employing MD simulations for a particular set of conformations constructed. In case of the DS, the ensemble average of the polymer conformations is calculated using sufficiently large unit cells, that is containing enough molecular units (polymer repeating units or solvent molecules). In order to find the best compromise of computational effort and accuracy of the simulation procedure, the reproducibility of the sampling of CED or Hildebrand solubility parameters (SP) $\delta_i = \sqrt{c_i}$, respectively, was tested by repeating the DS for 10 different MC generated unit cells using different system sizes (No. of polymer repeating units per unit cell). This was done for the model polymers PEG (chain length 25 and 50) and PLA (chain length 25) in collaboration with Mr. Mingzhe Chi [181]. The resulting SP as a function of the system size are shown in Figure 5.1a.

For both, PEG and PLA, the SP show large fluctuations (standard deviations) for repeated simulations of unit cells containing less than 150 polymer repeating units. In contrast, for system sizes of 500 repeating units the SP for PEG are 21.5 (DP 25) and 20.5 (DP 50) as well as for PLA 19.4 MPa$^{0.5}$ along with standard deviations of less than 0.2 MPa$^{0.5}$. In addition, the SP are
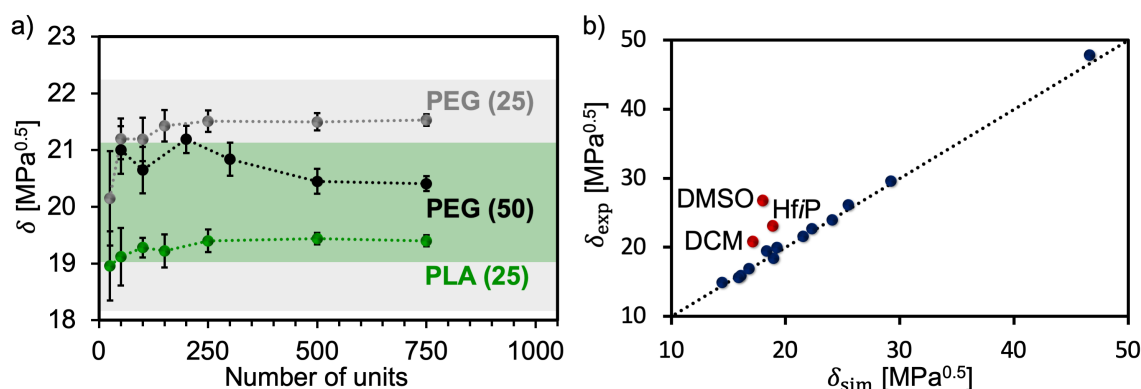
FIGURE 5.1: Hildebrand solubility parameters δ_i for a) PEG (chain lengths 25 and 50) and PLA (chain length 25) as a function of the number of repeating units in the unit cells (shaded areas indicate range of exp. values [193], PEG: gray, PLA: green) and b) for solvents listed in Table 5.1. Blue dots in b) correspond to compounds containing only C, H, N and O.

are almost identical with those calculated for unit cells comprising 750 repeating units confirming that a sufficient statistical sampling of polymer conformations is achieved by using 500 units per unit cell providing reproducible values for δ_i. These lie in the range of experimentally determined δ_i from 18.2-22.2 and 19.0-21.2 MPa$^{0.5}$ for PEG and PLA, respectively, showing that the employed simulation procedure not only provides realistic atomic structures but also indicates reliable quality of the used interatomic potential functions [131] for calculation of SP.

To further verify the accuracy of the used interatomic potential functions (IP), the DS is applied to various commonly used solvents for calculation of the SP. Comparison of the resulting SP with the corresponding experimentally determined values [80] is depicted in Figure 5.1b. In addition, Table 5.1 summarizes the total (Hildebrand) δ_i obtained from simulations and experiment as well as the calculated van der Waals $\delta_{i,\text{vdw}}$ and electrostatic $\delta_{i,\text{el}}$ SP. For compounds containing only C, N, O and H the calculated SP show a very good agreement with experimental observations. For this set of solvents (blue dots in Fig. 5.1b) the mean absolute error (MAE) is about 0.6 MPa$^{0.5}$ and 30 J/cm^3 for the SP and CED, respectively. However, considerable deviations of 4.2, 3.7 and 8.7 MPa$^{0.5}$ from the experimental values were obtained in case of the halogen containing solvents hexafluoro-2-propanol (HfiP) and dichloromethane (DCM) as well as the sulfur compound dimethyl sulfoxide (DMSO), respectively. Therefore, reliable solubility predictions using the IP employed in this work are only possible for polymers and active substances consisting of C, N, H, O, which is sufficient in most pharmaceutical and biomedical applications. Please note, for water a van der Waals CED of -564 J/cm3 was obtained, that is repulsive contributions of the Lennard-Jones term of the IP to the intermolecular energy in this case. Therefore, $\delta_{i,\text{vdw}}$ is undefined and in the following it is assumed that the intermolecular interactions between water molecules are purely electrostatic with $\delta_{i,\text{el}} = \delta_i = 46.59$ MPa$^{0.5}$ such that $\delta_{i,\text{vdw}} = 0$.

TABLE 5.1: Comparison of total δ_i, electrostatic $\delta_{i,\mathrm{el}}$ and van der Waals solubilty parameters $\delta_{i,\mathrm{vdw}}$ [MPa$^{0.5}$] determined using atomistic simulations (sim) and experiments (exp) [80].

Solvent	sim			exp[a]
	δ_{tot}	δ_{el}	δ_{vdw}	δ_{tot}
acetone	19.26	9.30	16.87	19.94
acetonitrile	23.86	16.69	17.05	24.40
benzene	18.96	5.74	18.07	18.51
n-dodecane	16.11	0.51	16.10	16.00
dichloromethane (DCM)	17.88	6.15	16.79	20.20
diethyl ether (DEE)	15.27	3.35	14.90	15.64
dimethyl acetamid (DMAc)	22.30	10.53	19.66	22.77
dimethyl formamide (DMF)	24.08	13.15	20.17	24.86
dimethyl sulfoxide (DMSO)	18.04	9.48	15.34	26.68
ethanol	25.50	22.40	12.19	26.52
n-hexane	14.44	0.45	14.43	14.90
hexafluoro-2-propanol (HfiP)	18.91	12.85	13.87	23.07
methanol	29.23	26.86	11.53	29.61
tetrahydrofuran (THF)	18.33	4.85	17.68	19.46
water	46.59	52.30	-[a]	47.81

[a] Van der Waal cohesive energy density of water is -564 J/cm^3

5.1.2 Inherent structure sampling

As shown in the previous section, by using unit cells containing at least 500 polymer repeating units facilitates sufficient sampling of polymer conformations to provide reproducible results for the CED and the Hildebrand SP, respectively. However, sampling of the intermolecular interactions of complex, amorphous polymer-active mixtures can be very challenging since even larger unit cells are required to ensure the reliable sampling of all relevant molecular configurations. Here, the inherent structure sampling (ISS) described in Section 2.2.4 is applied as potential, computationally more efficient alternative to the DS. It employs a set of considerably smaller MC constructed unit cells, *e.g.*, containing 150 instead of 500 PEG repeating units, and allows a parallelized, hence, computationally efficient sampling of the generated unit cells by MD simulations.

Figure 5.2 depicts the total probability densities $P(e_{\mathrm{IS}})$ (eq 2.72) of the inherent structures (IS) as a function of their potential energy (per atom) e_{IS} relative to the lowest energy structure calculated for pure PEG and water as well as the corresponding mixture. In addition, the weighted distributions $w_i P_i(e_{\mathrm{IS}})$ for each MC generated unit cell is shown. In case of pure water, every MD sampling of the MC constructed unit cells cover virtually the whole range of the relative IS energies e_{IS} with almost identical mean e_{IS} values for each sampling. Despite a sampling temperature of 400 K was chosen for the ISS that is clearly above the glass transition temperature of PEG (about 250 K) [182], mean value and sampled range of e_{IS} depend, albeit slightly, on the initial conformation constructed. This is connected with the far longer relaxation times of macromolecular compound compared to low molecular weight molecules in the liquid state [194]. Therefore, not all relevant conformations of the configuration space can
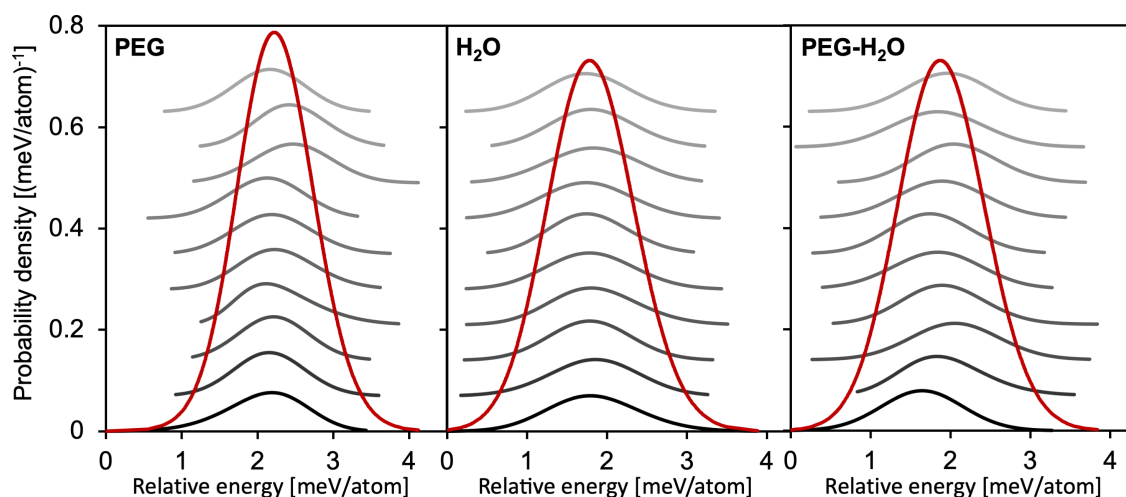
FIGURE 5.2: Total probability density $P(e_{IS})$ (red lines, eq 2.72) as a function of the relative potential energy (per atom) e_{IS} (w.r.t. the lowest energy structure) of the sampled inherent structures (IS) along with the weighted distributions $w_i P_i(e_{IS})$ (gray lines) calculated for individual MC generated unit cells for PEG, H_2O as well as the corresponding mixture.

be sampled during one single MD simulation using simulation times of less than 1 ns. However, assuming local (internal) ergodicity of MD simulations [153], the employed ISS samples the basin of the PES represented by particular chain conformations of the 3 PEG molecules (each with 50 repeating units) within the MC constructed unit cells.
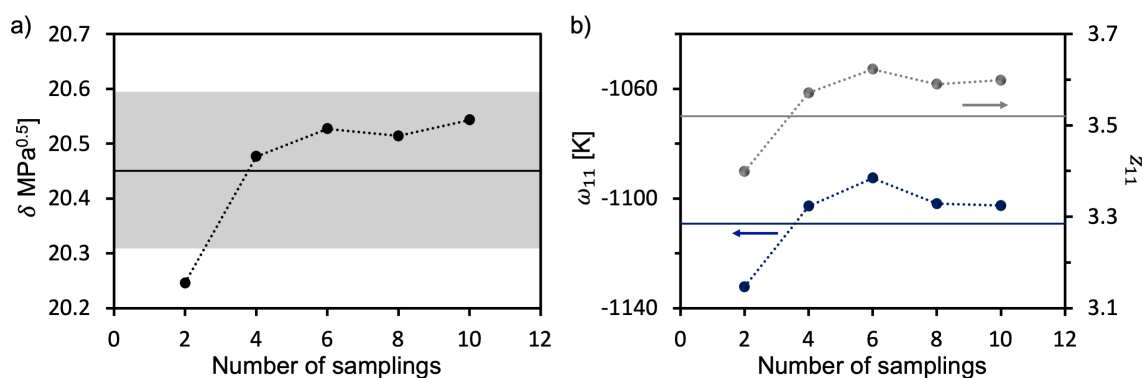
FIGURE 5.3: Results of inherent structure sampling (ISS) of PEG using different numbers of MC generated unit cells: a) Hildebrand solubility parameter δ as well as b) interaction parameter ω_{11} of the square well potential (eq 2.30) and coordination number z_{11} (eq 2.37). The lines indicate the results of the direct sampling (DS) using 500 units per unit cell. The shaded area in (a) corresponds to the standard deviation of δ obtained from DS.

For calculation of the macroscopic properties, the DS employs large unit cells for sampling of a sufficiently large number of polymer conformations. In contrast, the calculation of $P(e_{IS})$ by the ISS allows to combine separate MD samplings of different smaller structure models. Figure 5.3 shows the Hildebrand SP δ_1, coordination number z_{11} (eq 2.37) and the interaction parameter ω_{11} of the square well potential (eq 2.30) for PEG calculated using the ISS along with

different numbers of MC generated unit cells n_{MC} (samplings) in comparison with the results of the DS. Starting from $n_{MC} = 4$, the SP of PEG shows very good agreement with the value obtained from DS. Moreover, it changes only within the standard deviation of δ_1 calculated using DS (shaded area in Fig. 5.3a) when n_{MC} is further increased. Similarly, the coordination number $z_1 1$ quantifying the intermolecular structure of the first coordination shell of the PEG repeating units agrees well with the results of the DS. Thus, the interaction parameter ω_{11} of the intermolecular (square well) potential required for the thermodynamic modeling described in the next section shows the same trend. Consequently, the ISS using $n_{MC} = 10$ provides statistically relevant sampling of both, the intermolecular structure and interactions, with same accuracy as the DS.
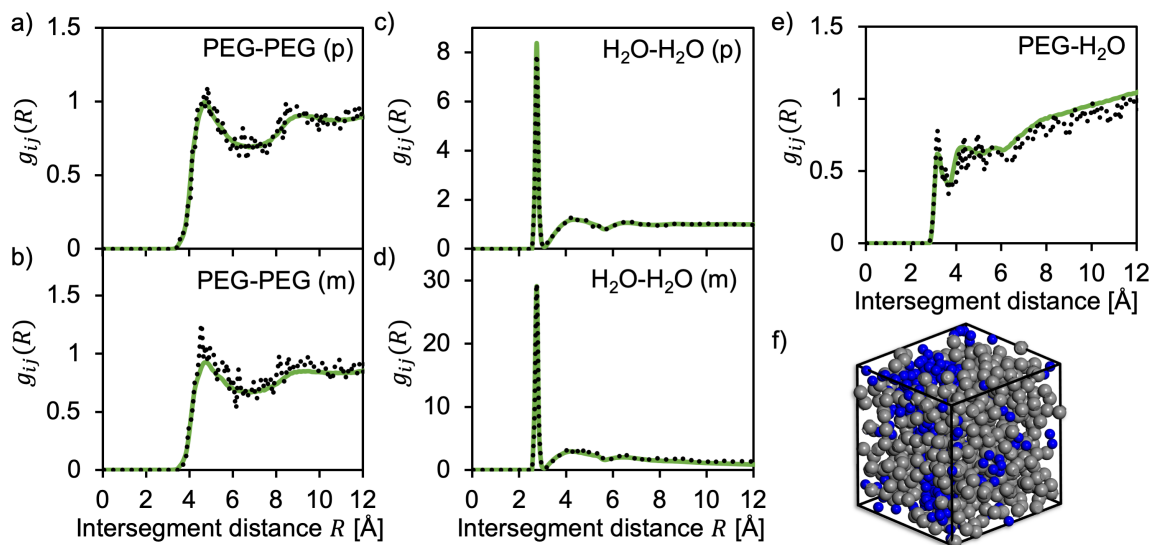
FIGURE 5.4: Radial distribution functions $g_{ij}(R)$ of PEG repeating units and H_2O molecules in the pure (p) and mixed (m) state (a-e) calculated using direct sampling (black dots) and inherent structures sampling (ISS) with 10 MC generated unit cells (green lines). In addition, a structure model of the mixture containing PEG (gray segments) and H_2O (blue) is shown (f).

More detailed comparison ISS and DS for the intermolecular structure is shown in Figure 5.4 using the radial distribution functions (RDF) $g_{ij}(R)$ of PEG repeating units and H_2O molecules in the pure (p) and mixed (m) state. Very good agreement of ISS and DS results are obtained in each case, while the ISS provides higher resolution of the RDF indicating a more accurate sampling of the intermolecular structure if 10 MC generated unit cells are sampled by MD simulations. As can be seen from PEG-H_2O RDF and the structure model shown in Fig. 5.4f, PEG and H_2O are not randomly mixed but rather show partial demixing at the molecular level. Such incomplete mixing at the molecular scale was observed for strongly hydrogen bonding mixtures such as concentrated alcohol-H_2O mixtures [96], yet this molecular level phase separation can also be connected with the periodic boundary conditions employed for both ISS and DS. However, in this work an intermolecular potential is derived from atomistic simulations and applied to parameterization of thermodynamic models that assume random mixing. Therefore, exact long-range intermolecular structure is not of major importance for the solubility predictions in this work rather than the nearest neighbor interactions determined by the short and medium-range order. This implies the lower limit of the unit cell size,

which can be used for the ISS. Due to the periodic boundary conditions, the unit cells have to be large enough to include at least the first or for modeling of the medium-range order, the second coordination shell of the intermolecular structure. Therefore, the length of each lattice vector has to be twice as large as the range of the RDF used for calculation of the pair potential. In case of PEG and H_2O as well as their mixture, the lengths of the lattice vectors of the equilibrated structure models are at least 21 Å such that the RDF captures structural information at least upto 10 Å. As shown in Fig. 5.4, this includes the first and second coordination shell in each case.

5.2 Polymer solubility models

5.2.1 Qualitative solubility predictions

As shown in Section 2.1.4, the simplest approximation of the FH interaction parameter $\chi_{FH} \approx \chi_{HSC}$ using the Hildebrand-Scatchard (HSC) equation 2.47 assuming that the intermolecular interaction between unlike lattice segments $i - j$ is approximated by the geometric average of the CED [77]. Applying this mixing rule to the concept of the Hansen solubility parameters [80], the contributions of $i - j$ contacts to the CED are approximated as $\delta^2_{ij,el} = \delta_{i,el}\delta_{j,el}$ and $\delta^2_{ij,vdw} = \delta_{i,vdw}\delta_{j,vdw}$ for the electrostatic (el) and van der Waals (vdw) interactions, respectively, calculated with the interatomic potential functions used.

   Figure 5.5 shows the plot of $\delta_{i,el}$ and $\delta_{i,vdw}$ for PEG and different solvents listed in Table 5.1, denoted here as solubility maps in which each compound is assigned to a point $(\delta_{i,vdw}, \delta_{i,el})$. Since the distance between two points is proportional to the (positive) energy of mixing $\Delta e_{mix,FH}$ (*cf.* eqs 2.34 and 2.49), one can define a critical distance R_c (eq 2.52) of two points upto both compounds are soluble in each other. Assuming a segment volume of the FH mean-field lattice of $\overline{\nu_s} = 75.4$ cm^3/mol (average molar volume of solvents listed in Table 5.1) and a PEG chain length of 50, R_c is 4.6 MPa$^{0.5}$. Therefore, a circle can be defined around PEG ($\delta_{ij,el} = 18.5$, $\delta_{ij,vdw} = 7.9$ MPa$^{0.5}$) enclosing all solvents that are predicted to solubilize PEG for every solution composition.

   As can be seen in Figure 5.5, this qualitative solubility predictions show good agreement with experiments [193] if $\delta_{2,el}$ of the solvents are lower than approximately 15 MPa$^{0.5}$. However, the solubility predictions fail for solvents with higher $\delta_{2,el}$, in particular in case of water ($\delta_{2,el} = 46.59$ MPa$^{0.5}$) and ethanol ($\delta_{2,el} = 22.4$ MPa$^{0.5}$). This is connected with the formation of hydrogen bonds in solution and, consequently, the mixing rule assumed above does not apply to $\delta_{ij,el}$. However, for sufficiently low $\delta_{i,el}$, solubility maps as shown in Fig. 5.5 allow rapid qualitative solubility predictions, since no atomistic simulations of the actual mixture are required. In this way, the thermodynamic compatibility between numerous polymers and biologically active compounds can be qualitatively evaluated facilitating rapid prescreening of, *e.g.*, promising polymer-drug combinations showing high encapsulation efficiency. In addition, $\delta_{i,el}$ can be potentially used as measure for specific interactions in order to evaluate which polymer-active combination requires further simulations of the corresponding mixture to achieve a more accurate modeling of the thermodynamic compatibility. However, more simulations of different (bio-)polymers, solvents and active substances are required to test this hypothesis.
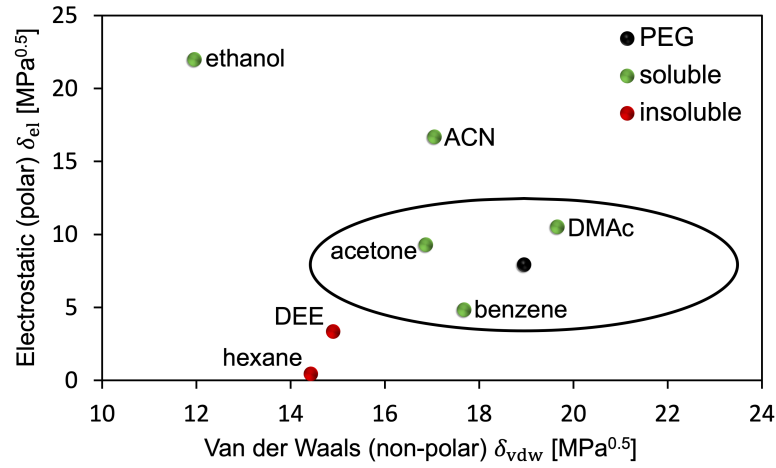
FIGURE 5.5: Qualitative solubility prediction of PEG in different solvents using the electrostatic δ_{el} and van der Waals solubility parameter δ_{vdw} calculated using atomistic simulations in comparison with experimental observations [193]. Solvents enclosed by the circle with radius $R_c = 4.6$ MPa$^{0.5}$ are predicted to dissolve PEG for arbitrary solution compositions.

5.2.2 Refined modeling of polymer mixtures

In case of strongly hydrogen bonding mixtures, such as aqueous PEG solutions, the qualitative solubility model described in the previous section clearly fails. Therefore, atomistic simulations of the actual mixtures are indispensable in order to account for specific interactions. While atomistic simulations were shown to accurately describe intermolecular interactions (Section 5.1.1), thermodynamic models such as FH mean-field lattice theory do not consider the effects of specific (directional) interactions. Similarly, the PHSC EOS assumes a statistical ensemble of randomly mixed hard sphere chains (*cf.* Fig. 2.4) without explicit consideration of specific interactions. Therefore, the effects of specific interactions on the temperature dependence of the interaction parameters ε_{ij} and ω_{ij} of the FH model and the PHSC EOS, respectively, are considered using the model in eq 2.65 for modeling the closed-loop phase diagram of PEG-H$_2$O.

TABLE 5.2: Parameters $\omega_{ij,ns}$ [K], $\delta\omega_{ij}$ [K] and q_{ij} for calculation of the temperature dependent intersegment interaction ω_{ij} (eq 2.65) of the square well potential (eq 2.30). In addition, the coordination numbers z_{ij} and the parameters J_{ij}, L_{ij} used for calculation of the composition dependent FH parameter χ_z (eq 2.46) for PEG ($i, j = 1$) and H$_2$O ($i, j = 2$) are shown.

Model	$\omega_{ij,ns}$	$\delta\omega_{ij}$	q_{ij}	z_{11}	z_{22}	z_{12}	J_{ij}	L_{ij}
PEG	491	704	1.627	3.599	0	0	-1.257	-2.342
H$_2$O	585	964	5.386	0	7.086	0	-9.087	2.001
PEG-H$_2$O	128	976	5.726	2.527	4.835	1.896	4.022	-

Table 5.2 lists the parameters for calculation of the temperature dependence of interaction parameter ω_{ij} (eq 2.65) of the square well (SW) potential (eq 2.30), which is used together with the coordination numbers z_{ij} for calculation of the FH parameter χ_{FH} (eq 2.33). Please note, in order to keep consistency with the original formulation of the FH theory ω_{ij} was defined as

$\omega_{ij}(T) = -\varepsilon_{ij}(T)$ in eq 2.65. The intermolecular interaction parameter of PEG segment is -1100 K at 300 K and increases to -976 K at 550 K. For water, stronger intersegment interactions with ω_{22} ranging from -1378 to -1084 K between 300 and 550 K were found. In the same temperature range the interaction between PEG and H_2O segments changes decreases from -928 to -624 K. Together with an average coordination number $z_{FH} = 5.3$ (black dotted line in Fig. 2.3), the calculated FH interaction parameters χ_{FH} are highly positive ranging from 5.5 at 300 K to 3.9 at 550 K.

Moreover, the parameters used for calculation of the composition dependent FH parameter χ_z are shown in Table 5.2. Due to the large difference of z_{11} and z_{22}, pronounced composition dependence of the lattice coordination number was obtained (*cf.* Fig. 2.3). The relatively large coordination number of water z_{22} of 7.1 originates from the definition of R_1 (about 3.9 Å) in eq 2.28 as diameter of a sphere showing the molar volume of water, which includes also free volume and, thus, z_{22} includes parts of the second coordination shell (next nearest neighbors).

TABLE 5.3: Parameters σ_{ij}^{un} [Å] as well as $\varepsilon_{ij,ns}^{un}$ [K], $\delta\varepsilon_{ij}^{un}$ [K] and q_{ij}^{un} of the temperature dependent Lennard-Jones potential (eqs 2.31, 2.65) of molecular units (un) defined as PEG repeating units and H_2O molecules, respectively.

	$\varepsilon_{ij,ns}^{un}$	$\delta\varepsilon_{ij}^{un}$	q_{ij}^{un}	$\sigma_{ij}^{un}(T)$					
				300	350	400	450	500	550
PEG	398.308	962.871	337.238	4.575	4.622	4.657	4.689	4.719	4.743
H_2O	592.601	958.375	5.457	2.867	2.870	2.873	2.877	2.881	2.886
PEG-H_2O	82.479	1084.703	7.022	3.481	3.504	3.533	3.559	3.584	3.613

In contrast to the SW potential, the derivation of the effective Lennard-Jones (LJ) potential of PEG repeating units (un) and H_2O molecules, respectively, used not only the CED (eq 2.28) but also the pressure as a function of temperature (compressibility factor Z, eq 2.32) obtained from atomistic simulations. The resulting parameters $\sigma_{ij}^{un}(T)$ as well as $\varepsilon_{ij,ns}^{un}$, $\delta\varepsilon_{ij}^{un}$ and q_{ij}^{un} for calculation of the temperature dependent interaction parameter $\varepsilon_{ij}^{un}(T)$ (eq 2.65) are summarized in Table 5.3. In each case, these parameters provide good agreement of the CED and pressure with a root mean square deviation lower than 1.8 J/cm^3 and 0.9 MPa, respectively, far lower than the estimated uncertainty of the employed IP (Section 5.1.1). The (average) equilibrium distance of two neighboring units $\sigma_{ij}^{un}(T)$ increases slightly with temperature in accordance with positive thermal expansion of PEG-H_2O mixtures observed in experiments [195]. The interaction parameter $\varepsilon_{ij}^{un}(T)$ of PEG-PEG, H_2O-H_2O and PEG-H_2O pairs decreases between 300 and 550 K in the range of 464-415 K, 1376-1082 K and 995-631 K, respectively. This indicates that specific interactions of H_2O-H_2O and PEG-H_2O pairs affect the physico-chemical properties of aqueous PEG solutions most.

Table 5.4 shows three parameter sets P1-P3 of the PHSC EOS for pure PEG and H_2O calculated by using least square fitting of the repulsive (rep) and attractive (att) CED (c_{rep}, c_{att}) and pressures (p_{rep}, p_{att}) obtained from simulations (*cf.* Section 2.1.4). The same model for the temperature dependence of the interaction parameters ε_{ij} (eq 2.65) as for the LJ and SW potential was applied. The PHSC EOS models every molecular unit (polymer repeating unit or solvent molecule) as chains of spherical segments with σ_{ij} and chain length r_i^* (*cf.* Fig. 2.4). The total length of a (macro)molecule consisting of N_{un} units is $r_i = r_i^* N_{un}$ (used in eqs 2.53-2.59). In addition, the parameters of the intersegment potential of PEG-H_2O segment pairs for

TABLE 5.4: Fitted parameter sets P1-P3 of the intersegment potential of the PHSC EOS (eqs 2.53-2.66) for pure PEG and H_2O. They include the segment diameter σ_{ij} [Å], the number of segments per molecular unit r_i^* as well as model parameters of the temperature dependent interaction parameter (eq 2.65) $\varepsilon_{ij,ns}$ [K], $\delta\varepsilon_{ij}$ [K] and q_{ij}.

	PEG					H_2O				
	$\varepsilon_{11,ns}$	$\delta\varepsilon_{11}$	q_{11}	σ_{11}	r_1^*	$\varepsilon_{22,ns}$	$\delta\varepsilon_{22}$	q_{22}	σ_{22}	r_2^*
P1	171.04	0.5903	233.36	2.7237	3.8693	501.07	130.61	1.7977	2.9446	1.4631
P2	171.89	0.5849	231.31	2.7201	3.8643	479.76	134.09	1.7314	2.9985	1.4177
P3	170.79	0.5924	234.27	2.7250	3.8711	497.25	129.36	1.7948	2.9353	1.4532

P1-P3 are shown in Table 5.5 including parameter λ_{12} that corrects the arithmetic average of σ_{11} and σ_{22} for calculation of σ_{12} (eq 2.64).

TABLE 5.5: Fitted parameter sets P1-P3 of the intersegment potential the PHSC EOS (eqs 2.53-2.66) for PEG-H_2O segments pairs. The temperature dependence of ε_{12} is modeled using eq 2.65 along with $\varepsilon_{12,ns}$ [K], $\delta\varepsilon_{12}$ [K] and q_{12}, while λ_{12} corrects the average segment diameter σ_{12} (eq 2.64).

	PEG-H_2O			
	$\varepsilon_{12,ns}$	$\delta\varepsilon_{12}$	q_{12}	λ_{12}
P1	318.50	369.38	572.84	-0.050759
P2	306.42	475.54	833.44	-0.088426
P3	321.96	401.43	516.17	-0.045405

Least square fitting of the PHSC EOS to the simulation results yielded three very similar parameter sets P1-P3 for the pure components. Slightly larger differences between the parameter sets were obtained for segment pairs. The mean interaction parameters $\varepsilon_{ij}(T)$ show qualitatively the same trends compared to the LJ parameters $\varepsilon_{ij}^{un}(T)$. Strongest interactions were found for H_2O segment pairs with, *e.g.* in case of P1, ε_{22} of 561 K at T = 300 K that decreases to 555 K when temperature raises to 550 K. For all parameter sets, ε_{11} is about 171 K and independent of temperature indicating low influence of specific interactions of PEG-PEG segment pairs on CED and pressure. The interaction parameter ε_{12} is only slightly dependent on temperature ranging from about 321 K to 320 K in case of P1.

Figure 5.6 shows (total) CED as well as pressures p as a function of temperature calculated using the parameter sets P1-P3 of the PHSC EOS and the LJ potential derived from atomistic simulations (SIM). Calculations used constant density obtained from NPT simulations at 300 K. In case of pure PEG, the $p(T)$ curves show fairly good agreement at 300 and 350 K. However, due to the clearly lower slope of $p(T)$ for P1-P3 compared to SIM, the PHSC EOS considerably underestimates the pressures at higher temperatures. The corresponding CED of P1-P3 are systematically higher than SIM by about 30%. In contrast, for water a larger slope of $p(T)$ was found for P1-P3 in comparison with SIM, while the CED are upto 15% lower in case of P2 (at 300 K). Due to the systematic overestimation of the CED of PEG, the CED of the mixture were not included in the training data for fitting of the PEG-H_2O parameters. Therefore, the $p(T)$ curves calculated using P1-P3 show a very good agreement with SIM, and similar to PEG, the CED is overestimated upto 27%. In general, the similarity of the PHSC EOS parameters P1-P3 results in close lying values for CED and pressures with exception of slightly lower CED of pure
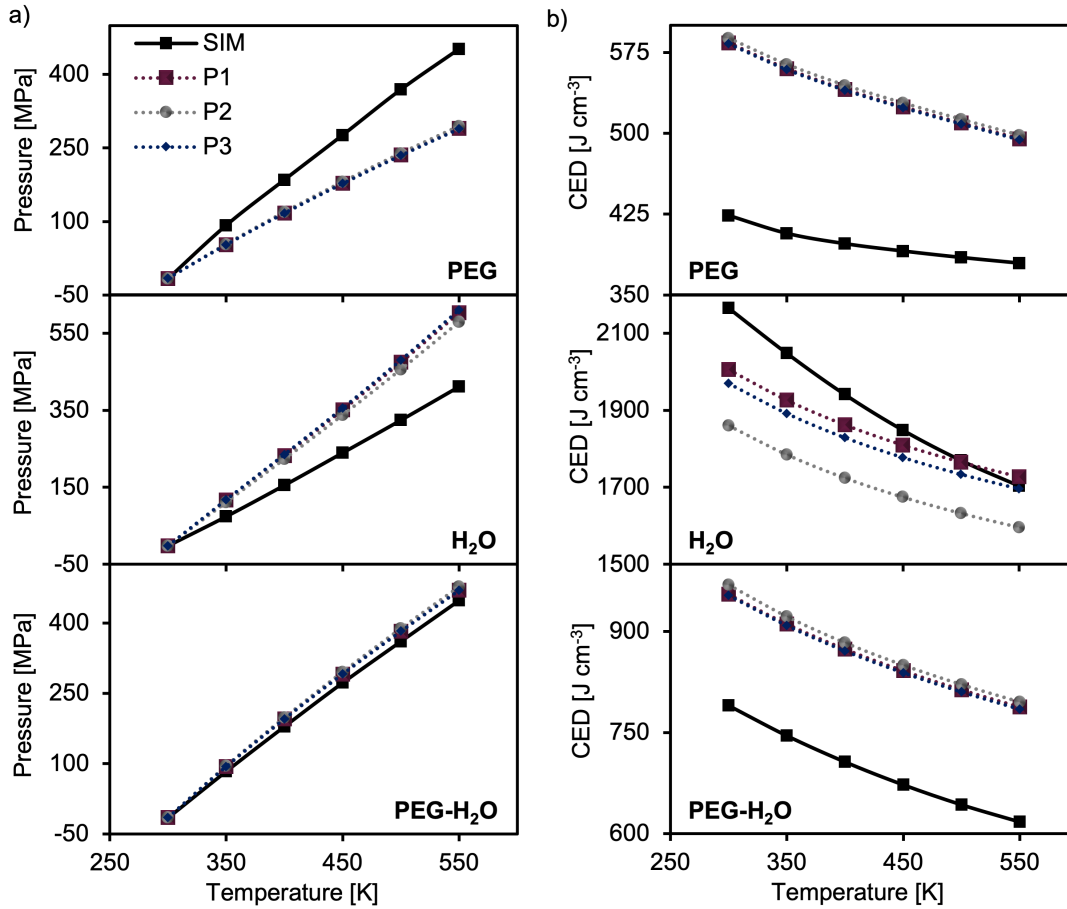
FIGURE 5.6: Pressures (a) and cohesive energy (b) densities (CED) as a function of temperature calculated using the Lennard-Jones potential derived from atomistic simulations (SIM) and the PHSC EOS employing the parameter sets P1-P3 (*cf.* Tables 5.4 and 5.5).

water in case of P2.

The separation of the intersegment (PHSC EOS) and LJ potential into repulsive (rep) and attractive (att) parts (*cf.* eqs 2.69 and 2.70) allows split of the total CED and pressures into attractive and repulsive contributions c_{rep}, c_{att} and p_{rep}, p_{att}, respectively. Deviations of c_{rep}, c_{att}, p_{rep} and p_{att} calculated using the fitted PHSC parameter set P1 with respect to the results of the LJ potential derived from atomistic simulations (SIM) at different temperatures are summarized in Table 5.6. For pure PEG, only minor deviations were obtained for c_{rep}, while c_{att} is considerably overestimated by P1 over the whole temperature range yielding too high total CED (Fig. 5.6). In contrast, the too low values of p_{rep} are compensated by too large p_{att} at lower temperatures. However, deviations of p_{rep} considerably increase with temperature, while the error of p_{att} remains almost constant resulting in a lower slope of $p(T)$ for P1 compared to SIM. Similarly, the relatively small deviations of p_{rep} and p_{att} in case of H_2O compensate at lower T, yet the overestimation of p_{rep} by P1 strongly increases at higher temperatures. Conversely, deviations c_{rep} are virtually independent of temperature, while the overestimation of c_{att} increases with increasing temperature yielding error compensation at higher T. In case of the PEG-H_2O mixture, largest deviations were obtained for c_{att} and comparatively pronounced

TABLE 5.6: Difference of repulsive (rep) and attractive (att) cohesive energy densities c_{rep}, c_{att} [J/cm^3] and pressures p_{rep}, p_{att} [MPa] of fitted PHSC parameter set P1 with respect to results calculated using the Lennard-Jones (LJ) potential obtained from atomistic simulations at different temperatures T [K].

	T	PEG				H$_2$O				PEG-H$_2$O			
		c_{rep}	c_{att}	p_{rep}	p_{att}	c_{rep}	c_{att}	p_{rep}	p_{att}	c_{rep}	c_{att}	p_{rep}	p_{att}
	300	-68	492	611	-628	-147	2313	2106	-2109	-91	881	957	-973
SIM	400	-92	490	796	-611	-144	2085	2062	-1907	-106	812	1069	-890
	500	-117	502	986	-616	-147	1917	2085	-1760	-123	765	1194	-834
	300	+0.3	+160	-92	+93	-340	+180	+17	-17	-58	+223	-36	+36
P1	400	+7	+136	-165	+98	-375	+296	+158	-81	-52	+219	+12	+4
	500	+8	+116	-256	+122	-344	+339	+271	-121	-49	+220	+38	-17

relative errors for c_{rep}, both almost independent of T.

In summary, an accurate fit of the PHSC (EOS) to the results obtained from atomistic simulations of both, $p(T)$ dependence and absolute values of CED for PEG containing systems, could not be achieved. As shown in eq 2.67, the (residual) potential energy $e_{\text{EOS}} < 0$ calculated from a pressure explicit EOS decreases with increasing slope of $p(T)$ at constant density. Consequently, steeper increase of pressure with temperature results in higher CED since $c = -\rho e_{\text{EOS}}$. Therefore, the employed PHSC EOS is not accurate enough to reproduce the simulation results for temperature dependence of the CED and pressure with equal quality. This is mainly connected with two major shortcomings of the parameterized EOS. First, the simple van der Waals perturbation Z_{pert} (eq 2.59) does not consider hard sphere contacts of a dense liquid, that is, it does not include a realistic (hard sphere) radial distribution function $g_{ij}\left(\eta,\, \xi_{ij}\right)$ (eq 2.55) as used in Z_{HS}. More accurate expressions for Z_{pert} have been derived by Hino and Prausnitz [196] using a square well potential for attractive intersegment interactions along with an approximate expression for consideration of $g_{ij}\left(\eta,\, \xi_{ij}\right)$. Second deficiency of the employed PHSC EOS is the simplified model for consideration of specific, directional interactions by using an average, temperature dependent interaction parameter $\varepsilon_{ij}(T)$ (eq 2.65). Obviously, this model is insufficient to accurately include the effects of hydrogen bonding. This can be resolved by adding analytical expressions for association sites of hydrogen bonds to the PHSC using, *e.g.*, the Statistical Association Fluid Theory (SAFT) [101, 102, 132]. Employing such extensions of the PHSC EOS appears promising to facilitate more accurate modeling of the temperature dependence of CED and pressures obtained from atomistic simulations.

Figure 5.7 shows experimentally observed water vapor pressures [197], mass densities of PEG-water solutions [195] and phase diagrams [198] for different PEG chain lengths (76 and 341) in comparison with the results calculated using the PHSC EOS along with the parameter sets P1-P3. Best agreement with experimentally determined water vapor pressures shows P2, despite it deviates most from CED obtained from simulations (Fig. 5.6). However, also P1 and P3 provide good agreement with experiments upto temperatures of about 500 K. In contrast, P1 and P3 show best agreement with experimental results for the mass densities of aqueous PEG solutions, yet all PHSC EOS parameters underestimate densities of concentrated PEG mixtures with PEG weight fractions above 0.8. The calculated phase diagrams using P1 and P2 depicted in Figure 5.7c show fairly good agreement with the experimentally determined ones. In particular, P1 accurately reproduces the experimentally observed upper critical solution
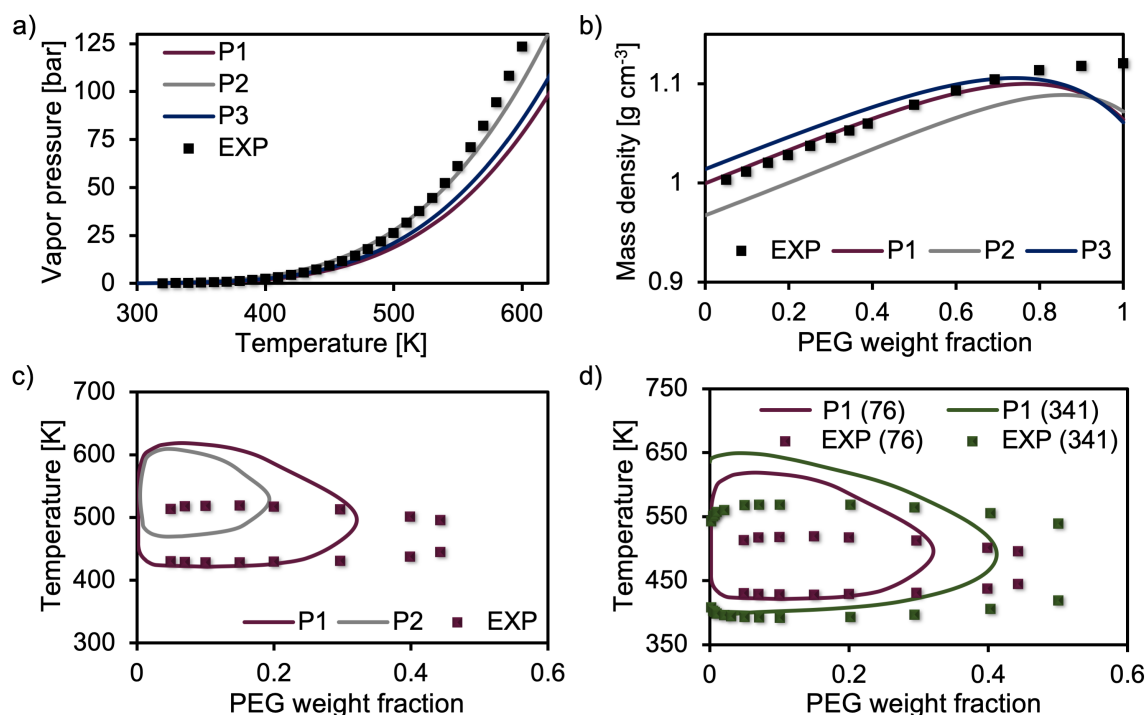
FIGURE 5.7: Results of the PHSC EOS using the parameter sets P1-P3 in comparison with experimental results (EXP): a) temperature dependence of the H_2O vapor pressure [197], b) mass densities of PEG-H_2O mixtures (PEG chain length 9) [195] and PEG-H_2O phase diagrams calculated using P1 and P2 for PEG chain lengths of 76 (c) as well as 341 (d). Experimentally determined phase diagrams taken from ref. [198].

temperatures (UCST) upto PEG weight fractions of 0.3, yet clearly overestimates the LCST. In case of P3, PEG is predicted to be soluble in water over the whole temperature (300 to 700 K) and composition range (0 to 1) considered. In addition, the calculated phase diagrams using P1 for different PEG chain lengths show a very good qualitative correlation with the chain length dependencies observed in experiments, particularly in case of the UCST. This clearly proofs that the employed parameterization procedure of the PHSC EOS by atomistic simulations is capable to provide reasonable thermodynamic models even for mixtures showing pronounced specific interactions, albeit it is connected with an error cancellation (at least) in case of the PEG and PEG-H_2O CED.

Despite the obtained parameters P1-P3 are very similar providing almost identical fits of CED and pressures (with exceptions of the water CED for P2), they yield distinct results for the physico-chemical properties of PEG-water mixtures. In particular, only small deviations Gibbs energies of mixing Δg_{mix} (per molecular unit) can lead to very different phase diagrams. Figure 5.8a depicts the comparison of $\Delta g_{mix,FH}$ and $\Delta g_{mix,z}$ calculated using the Flory-Huggins (FH) theory along with constant χ_{FH} (eq 2.33) and composition dependent χ_z (FH$_z$, eq 2.46) interaction parameter, respectively. Furthermore, values for $\Delta g_{mix,EOS}$ calculated using the PHSC

EOS along with P1-P3 are shown. As mentioned above, the parameters of the square well potential and the coordination numbers derived from simulations (Table 5.2) yield clearly positive χ_{FH} and, therefore, incorrectly predicts positive values for $\Delta g_{mix,FH}$ for all mixture compositions. One shortcoming of this approach is the assumption of a random mean field lattice with a coordination number z_{FH} independent of composition, which clearly disagrees with the RDF calculated from simulations (*cf.* Figs. 5.4 and 2.3). By employing the simple quadratic interpolation of the coordination numbers z_{ij} (*cf.* eqs 2.41 and 2.42) for calculation of χ_z provides indeed a qualitative correction of $\Delta g_{mix,FH}$ for PEG-water mixtures below PEG weight fractions of 0.8, yet quantitatively disagree with PHSC results for P1-P3. For the latter, similar $\Delta g_{mix,EOS}$ as a function of the solution composition were obtained, however, these minor differences lead to very distinct results for modeling of the PEG-H$_2$O phase diagram. Therefore, precise predictions of phase diagrams are not possible by combining the atomistic simulations with the PHSC EOS presented in this work. Yet, reasonable and reproducible values for $\Delta g_{mix,EOS}$ were obtained with an absolute deviation between P1 and P2 of less than 0.5 kJ/mol (MAE 0.3 kJ/mol). Thus, the employed simulation and modeling procedure is expected to provide sufficiently accurate $\Delta g_{mix,EOS}$ for evaluation of thermodynamic compatibility of active substances and various polymers. In contrast, the FH theory even by employing the proposed composition correction is unsuitable for thermodynamic modeling of mixtures showing pronounced specific interactions.

This is not only connected with the incorrect modeling of Δh_{mix} but also with the assumption of an ideal lattice for calculation of Δs_{mix}. Figure 5.8b shows the enthalpic Δh_{mix} and entropic contributions $-T\Delta s_{mix}$ to Δg_{mix} for P1 and FH$_z$ along with experimentally determined Δh_{mix} [199] for a PEG chain length of 68 at 353 K. Please note, as mentioned in Section 2.1.4 Δh_{mix} is well approximated by the energy of mixing Δe_{mix} at moderate pressures considered in this work. The composition dependence of $\Delta h_{mix,z}$ is similar to $\Delta g_{mix,z}$ due to the minor (negative) contributions of $-T\Delta s_{mix,z}$ using the ideal entropy of mixing $\Delta s_{mix,z} > 0$. In contrast, positive values $-T\Delta s_{mix,EOS}$ upto a PEG weight fraction of about 0.8 were obtained in case of P1, while $\Delta h_{mix,EOS}$, contrary to $\Delta h_{mix,z}$, shows fairly good agreement with the experimentally determined values. As for $\Delta g_{mix,EOS}$, similar values of the enthalpy and entropy of mixing were calculated for P2 and P3.

Table 5.7 compares Δg_{mix}, Δh_{mix} and Δs_{mix} calculated using the PHSC EOS (P1-P3) as well as the Flory-Huggins theory (FH and FH$_z$) with values for Δh_{mix} obtained from simulations and experiments [199] for a PEG weight fraction of about 0.8 and T = 353 K. The error of $\Delta h_{mix,sim} \approx \Delta e_{mix,sim}$ calculated using atomistic simulations, was estimated using error propagation of the general definition of Δe_{mix} (eq 2.29) assuming an uncertainty of the CED for pure PEG, water as well as their mixture of 30 J/cm^3 (MAE, *cf.* Section 5.1.1) yielding error limits of about ±1.9 kJ/mol. Therefore, the incorrect simulation result of an endothermic mixture with $\Delta h_{mix,sim}$ of 0.8±1.9 kJ/mol originates from the inaccuracy of the interatomic potential functions employed for calculations of CED. An uncertainty of 1.9 kJ/mol for Δh_{mix} corresponds to an expected error of the FH interaction parameter χ_{FH} of about ±3 in case of PEG-H$_2$O mixtures at 300 K and a PEG weight fraction of 0.8. Such error exceeds the value of FH parameters for many common polymer-solvent combinations [130, 193]. Therefore, the parameterization of accurate thermodynamic models exclusively based on CED and the energy of mixing
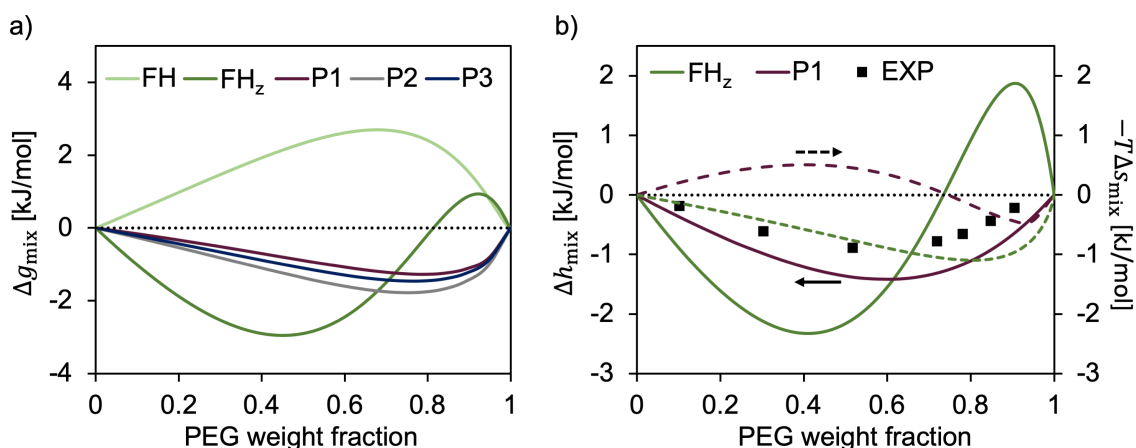
FIGURE 5.8: Results of the Flory-Huggins theory using composition independent (FH) and composition dependent (FH_z) interaction parameters as well as of the PHSC EOS using different parameter sets: a) Gibbs energy Δg_{mix} of mixing and its b) enthalpy Δh_{mix} (solid lines) and entropy contribution $-T\Delta s_{mix}$ (dashed lines) per molecular unit as a function of the PEG weight fraction. Calculations used PEG chain lengths of 68 at $T = 353$ K. Experimental (EXP) results for Δh_{mix} taken from ref. [199].

is virtually impossible, despite the calculated solubility parameters show a very good agreement with experiments (*cf.* Fig. 5.1). Furthermore, the estimated error of $\Delta h_{mix,sim}$ rationalizes the contradicting results of solubility predictions using the FH theory for various polymer drug/active mixtures obtained recently, which only partially agree with experimental observation (*e.g.*, refs. [74, 82, 83] and [X]). However, if specific interactions do not dominate the physico-chemical properties of polymer mixtures, as indicated by relatively low values of $\delta_{i,el}$, the calculated SP $\delta_{i,vdw}$ and $\delta_{i,el}$ can be used for qualitative solubility predictions potentially facilitating rapid screening of the thermodynamic compatibility between polymers and biologically active compounds (*cf.* Fig. 5.5).

TABLE 5.7: Gibbs energy Δg_{mix}, enthalpy Δh_{mix} [kJ/mol] and entropy Δs_{mix} of mixing [J/(mol K)] calculated using the PHSC EOS (P1-P3) as well as the Flory-Huggins theory (FH and FH_z) in comparison with simulations (sim.) and experiments (exp.) [199] for a PEG weight fraction of about 0.8 and $T = 353$ K.

	FH	FH_z	P1	P2	P3	sim.	exp.
Δg_{mix}	2.4	-0.3	-1.3	-1.8	-1.5	-	-
Δh_{mix}	3.5	0.8	-1.2	-2.4	-1.4	0.8 ± 1.9	-0.70 ± 0.01
Δs_{mix}	3.1	3.1	0.4	-1.8	0.3	-	-

Contrary to the FH theory, the parameterization of the PHSC EOS used not only the temperature dependence of CED but also of pressures. This allows a more accurate modeling of the intermolecular interactions by employing a LJ potential using both, pure and mixed states of the compounds under consideration. The subsequent separation of the intermolecular potential into repulsive and attractive contributions (eqs 2.69 and 2.70) facilitates the targeted parameterization of the reference part of the PHSC EOS $Z_{ref} = 1 + Z_{HS} + Z_{CB}$ representing an ensemble of non-interacting hard sphere chains and the perturbation part Z_{pert} including all

attractive interactions. In this way, considerably improved thermodynamic modeling of aqueous PEG solutions is achieved compared to the FH theory providing fairly good agreement of $\Delta h_{\mathrm{mix,EOS}}$ with experiments as well as negative $\Delta s_{\mathrm{mix,EOS}}$. The decrease of entropy due to mixing of two compounds showing strong hydrogen bonding is connected with the formation of complexes in solution as observed, *e.g.,* for alcohol-water mixtures [96, 97]. Similarly, previous theoretical studies [98] on the thermodynamic properties of PEG-H_2O mixtures found negative Δs_{mix}, which coincides largely with the results obtained in this work. In addition, negative Δs_{mix} were, *e.g.,* obtained for mixtures of meloxicam, a non-steroidal anti-inflammatory drug, and aqueous PEG solutions. This emphasizes the need for accurate thermodynamic models including the effects of pronounced hydrogen bonding on the physico-chemical properties of polymer-active mixtures. Even though the PHSC EOS parameterized in this work provides a reasonable thermodynamic description of PEG-H_2O solutions, its accuracy is still insufficient to reproduce both, CED and pressures as a function of temperature, with equal quality. However, by using more sophisticated expressions for Z_{pert} and applying more accurate models for consideration of specific interactions as discussed above, the present computational methodology appears a promising way for predictions of the capability of polymers to solubilize biologically active compounds. Moreover, the PHSC EOS has been extended for the thermodynamic modeling of statistical, block and alternating copolymers as well as their corresponding mixtures [135]. Therefore, the combination of such EOS with the atomistic simulation procedures presented here would provide a promising tool for the efficient, *in silico* design of sophisticated (co-)polymeric drug nanocarriers.

6   Conclusions

In summary, computational methods for the time effective, targeted design of materials have been proposed and applied to three case studies for distinct types of materials. Starting point in all cases was the determination of suitable atomic structure models allowing the subsequent calculation of the physico-chemical properties. Due to the combination of atomistic simulations with experimental observations, not only the prediction accuracy of the models parameterized was evaluated but also empirical corrections were derived facilitating computationally efficient predictions of structure property relationships.

In Chapter 3, comprehensive sampling of atomic configurations of $Ba_{1-m}Sr_mZn_{2-2n}Mg_{2n}Si_2O_7$ (BZS) solid solutions provided not only the lowest energy structures but also confirmed that structure and relative energies are almost independent of the precise arrangement of Ba^{2+}, Sr^{2+}, Zn^{2+} and Mg^{2+} ions on the respective lattice sites. Consequently, the lowest energy configurations obtained could be used for predictions of the martensitic phase transition temperatures T_t as a function of the chemical compositions (m, n). For this purpose, model functions for the vibrational free energy along with the harmonic approximation have been derived from DFT simulations for five chemical compositions with $(m > 0, n = 0)$ and $(m = 0, n > 0)$, respectively. However, predictions using the harmonic approximation considerably overestimate T_t by more than 1000 K and also qualitatively disagree with experimental observations of T_t for different chemical compositions. Therefore, available experimentally determined T_t have been used for derivation of an empirical correction of the vibrational free energy considering not only the effects of anharmonic lattice vibrations but also the error of DFT simulations as well as the simple composition dependent Debye model for the vibrational density of states (VDOS). The estimated prediction uncertainty is about ±100 K that is similar to the accuracy of the DFT simulations for prediction of polymorphous phase transitions. By employing the derived model, the T_t for all compositions (m, n) have been calculated showing almost same deviation of ±100 K from experimentally determined T_t not included in the model derivation.

Moreover, an empirical measure for T_t of 500 K has been used for elucidation of the chemical compositions for which the HT phase emerges during glass crystallization and persists during cooling down to room temperature. This is probably connected with kinetic hindrance of the martensitic phase transition. Therefore, the employed approach that combines DFT simulations with experimental data can be used for rapid predictions of both, T_t and promising chemical composition for which the desired HT phase can be obtained. For the latter, computationally more demanding simulations such as *ab initio* MD simulations can be applied in future studies to provide a deeper understanding of the structure-property relations of this BZS glass ceramics.

For BZS solid solutions $Ba_{1-m}Sr_mZn_2Si_2O_7$ with m = 0.25, 0.5 and 0.75, only the HT phase showing negative thermal expansion (NTE) emerges during glass crystallization. In addition, they show pronounced dependence of the anisotropic thermal expansion on the chemical

compositions. In contrast, the highly anisotropic elastic constants are almost independent of the chemical compositions. Therefore, the change of the negative thermal expansion along the crystallographic *a* axis has been attributed to the dependence of the Grüneisen parameters on the chemical composition that are connected with the lattice vibrations. Most pronounced changes of the VDOS have been obtained in the low frequency range (0-5 THz) at which the average microscopic Grüneisen parameters show negative values. The considerable shift of VDOS in this frequency range due to the substitution Ba^{2+} with Sr^{2+} rationalizes the decrease of the NTE along the *a* axis with increasing *m*. Furthermore, this NTE originates from the deformation of two-membered OSi–O–ZnO rings as indicated by the calculated microscopic Grüneisen parameters. By characterization of the anisotropic thermal expansion and calculation of the elastic constants, future continuum mechanics simulations, e.g., using the finite element method are capable to facilitate the targeted design of the microstructure of BZS glass ceramics for development of novel zero thermal expansion materials.

In case of small Fe_2O_3 gas phase clusters and nanoparticles (NP), the precise atomic structures cannot be determined by experiments. Therefore the atomic structure and properties of nanoparticulate Fe_2O_3 are characterized by combining global structure optimizations for small $(Fe_2O_3)_n$ gas phase clusters and simulated crystallizations of lager Fe_2O_3 NP. Structure elucidation of $(Fe_2O_3)_n$ nanoclusters used a two stage procedure that combines *ab initio* derived interatomic potential functions (IP) with refinements at the DFT level. Except for the tetrahedral, adamantane-like $(Fe_2O_3)_2$, $(Fe_2O_3)_n$ nanoclusters assume compact, almost amorphous structures with little or no symmetry. For larger $(Fe_2O_3)_n$ gas phase cluster with *n* > 5, lowest energy structures show the adamantane-like $(Fe_2O_3)_2$ entity as the main building unit. In addition, with growing cluster size they increasingly assume tetrahedral morphology. Simulated crystallization of larger NP used molecular dynamics simulations along with the tailored IP yielding single crystals with tetrahedral morphology in case of NP with diameters up to 3 nm. Larger NP with diameters of about 5 nm show hexagonal morphology and monocrystalline structures resembling ϵ-Fe_2O_3. These findings show very good agreement with the structure analysis of Fe_2O_3 nanopowders prepared by laser vaporization. Together with the good agreement between the IP calculated structures and properties of small nanoclusters and the results refined at the DFT level, this confirms the reliability of the employed approach for elucidation of structure and properties of nanoparticulate Fe_2O_3. Therefore, the structure models predicted are the basis for future simulations of the thermodynamic and magnetic properties to acquire deeper understanding of the structure property relations of Fe_2O_3 nanoparticles. Moreover, the first direct indication that ϵ-Fe_2O_3 may be thermodynamically the most stable phase in this size regime has been provided.

Finally, computationally efficient approaches for predictions of the thermodynamic compatibility between polymers and low molecular weight compounds have been proposed. For this purpose, the two main factors that determine the accuracy of polymer solubility predictions have been addressed. First, the inherent structures sampling (ISS) has been used for accurate modeling of the atomic structure of amorphous polymers facilitating efficient calculations of physico-chemical properties, particularly cohesive energy densities (CED) and pressures. Accuracy of the ISS has been confirmed by comprehensive test calculations using the direct sampling (DS) of polymer conformations within a single unit cell, which were shown

to provide reproducible results for the CED. Main advantage of the ISS over the DS is the simple yet efficient parallelization of the sampling of the potential energy surface. In addition, the accuracy of the interatomic functions used for calculation of CED has been evaluated yielding good agreement with experiments along with a mean absolute error of about 30 J/cm^3 for compounds containing C, N, O and H, that are the most important elements of biomedically relevant substances.

Subsequently, different models have been parameterized from the simulation results to facilitate an accurate modeling of the polymer solubility - the second central factor for prediction of the thermodynamic polymer-active compatibility. The CED obtained from simulations along with their energetic contributions of electrostatic and van der Waals interactions have been used for calculations of the solubility parameters (SP) based on the concept of Hansen. Together with the Flory-Huggins (FH) theory, the SP have been employed for qualitative solubility predictions of the model polymer polyethylene glycol (PEG) with various solvents, denoted here as solubility maps. These show good agreement with experimental observations, if the van der Waals part dominates the intermolecular interactions. However, this model fails for polymer mixtures showing pronounced specific interactions such as hydrogen bonding. The electrostatic SP can potentially be used for quantification of specific interactions, albeit more test simulations are required to confirm this. Such an approach would allow rapid determination of promising polymer-active combinations that show high encapsulation efficiency of the corresponding nanocarriers.

For the refined modeling of the polymer solubility, the specific interactions have to be explicitly considered by atomistic simulations of the actual polymer solution. Here, aqueous PEG solutions showing pronounced hydrogen bonding have been chosen as test case. The FH theory clearly fails to describe such systems irrespective if a constant or composition dependent interaction parameter is used. This is mainly due to the inaccuracy of the IP employed for calculation of the CED that translates into an error of 1.9 kJ/mol for the enthalpy of mixing. Since such an uncertainty exceeds the enthalpy of mixing of most polymer mixtures, parameterization of accurate thermodynamic models based on CED alone is virtually impossible. Second shortcoming of FH theory is the assumption of the ideal lattice for calculation the entropy of mixing unable to model negative entropy changes of strongly hydrogen bonded mixtures such as aqueous PEG solutions.

In contrast, the parameterization of the PHSC EOS used both, CED and pressures as a function of the temperature yielding good agreement with experimental data as well as previous theoretical studies of PEG-water mixtures including the enthalpy and entropy of mixing. However, this is partially connected with error compensations of the CED of PEG and the PEG-water mixture since the used PHSC EOS is still too inaccurate to reproduce CED and pressures obtained from simulations with same quality. This is most probably due to the oversimplified van der Waals perturbation term of the compressibility factor used that emphasizes the need of more accurate expressions to model such systems. Consequently, accurate and reproducible predictions of phase diagrams could not be obtained since only small errors of the free energy lead to large deviations of the calculated phase diagrams. Nonetheless, the PHSC EOS provides reproducible values of the free energy of mixing that are expected to be sufficiently accurate for reliable predictions of the thermodynamic compatibility between polymers and drugs even for systems showing strong specific interactions. Moreover, the PHSC EOS can

be straightforwardly extended to copolymers for modeling of more sophisticated polymeric nanocarriers. Therefore, the combination of qualitative solubility predictions using the FH theory (solubility maps) as rapid prescreening approach with parameterization of the PHSC EOS by atomistic simulations of polymer mixtures for explicit consideration of specific interactions is expected to be an efficient tool for the *in silico* design of polymeric drug nanocarriers.

Bibliography

[1] S. M. Woodley, R. Catlow, *Nat. Mater.* **2008**, *7*, 937–946.

[2] K. T. Butler, J. M. Frost, J. M. Skelton, K. L. Svane, A. Walsh, *Chem. Soc. Rev.* **2016**, *45*, 6138–6146.

[3] S. Curtarolo, G. L. W. Hart, M. B. Nardelli, N. Mingo, S. Sanvito, O. Levy, *Nat. Mater.* **2013**, *12*, 191–201.

[4] A. Ganesan, M. L. Coote, K. Barakat, *Drug Discov. Today* **2017**, *22*, 249–269.

[5] A. Jain, Y. Shin, K. A. Persson, *Nat. Rev. Mater.* **2016**, *1*, 15004.

[6] P. Friederich, V. Gómez, C. Sprau, V. Meded, T. Strunk, M. Jenne, A. Magri, F. Symalla, A. Colsmann, M. Ruben, W. Wenzel, *Adv. Mater.* **2017**, 1703505.

[7] A. G. Slater, A. I. Cooper, *Science* **2015**, *348*, aaa8075.

[8] M. Sierka, *Prog. Surf. Sci.* **2010**, *85*, 398–434.

[9] B. Fultz, *Prog. Mater. Sci.* **2010**, *55*, 247–352.

[10] J. Neugebauer, T. Hickel, *Wiley Interdiscip. Rev. Comput. Mol. Sci.* **2013**, *3*, 438–448.

[11] P. Anastas, N. Eghbali, *Chem. Soc. Rev.* **2010**, *39*, 301–312.

[12] M. Sankar, N. Dimitratos, P. J. Miedziak, P. P. Wells, C. J. Kiely, G. J. Hutchings, *Chem. Soc. Rev.* **2012**, *41*, 8099.

[13] M.-M. Titirici, R. J. White, N. Brun, V. L. Budarin, D. S. Su, F. del Monte, J. H. Clark, M. J. MacLachlan, *Chem. Soc. Rev.* **2015**, *44*, 250–290.

[14] H. Bach, D. Krause, *Low Thermal Expansion Glass Ceramics*, 2nd ed., Springer, Berlin, Heidelberg, **2005**.

[15] G. D. Barrera, J. A. O. Bruno, T. H. K. Barron, N. L. Allan, *J. Phys.-Condens. Matter* **2005**, *17*, 217–252.

[16] K. Takenaka, *Sci. Technol. Adv. Mater.* **2012**, *13*, 013001.

[17] W. Miller, C. W. Smith, D. S. Mackenzie, K. E. Evans, *J. Mater. Sci.* **2009**, *44*, 5441–5451.

[18] C. Thieme, C. Rüssel, *Materials* **2016**, *9*, 631.

[19] C. Thieme, T. Waurischk, S. Heitmann, C. Rüssel, *Inorg. Chem.* **2016**, *55*, 4476–4484.

[20] J. Lin, G. Lu, J. Du, M. Su, C.-K. Loong, J. Richardson, *J. Phys. Chem. Solids* **1999**, *60*, 975–983.

[21] M. Kerstan, M. Müller, C. Rüssel, *J. Solid State Chem.* **2012**, *188*, 84–91.

[22] C. Thieme, C. Rüssel, *Dalton Trans.* **2016**, *45*, 4888–4895.

[23] S. Baroni, S. de Gironcoli, A. Dal Corso, P. Giannozzi, *Rev. Mod. Phys.* **2001**, *73*, 515–562.

[24] R. P. Stoffel, C. Wessel, M.-W. Lumey, R. Dronskowski, *Angew. Chem. Int. Ed.* **2010**, *49*, 5242–5266.

[25] A. Oganov in *Mineral Physics*, Treatise on Geophysics, Elsevier, **2007**, pp. 121–152.

[26] Y.-S. Lee, Y. Kim, Y. W. Cho, D. Shapiro, C. Wolverton, V. Ozoliņš, *Phys. Rev. B* **2009**, *79*, 104107.

[27] D.-B. Zhang, T. Sun, R. M. Wentzcovitch, *Phys. Rev. Lett.* **2014**, *112*, 058501.

[28] J. B. Haskins, A. E. Thompson, J. W. Lawson, *Phys. Rev. B* **2016**, *94*, 214110.

[29] O. J. Weber, D. Ghosh, S. Gaines, P. F. Henry, A. B. Walker, M. S. Islam, M. T. Weller, *Chem. Mater.* **2018**, *30*, 3768–3778.

[30] F. C. Serbena, E. D. Zanotto, *J. Non-Cryst. Solids* **2012**, *358*, 975–984.

[31] A. Erba, J. Maul, M. De La Pierre, R. Dovesi, *J. Chem. Phys.* **2015**, *142*, 204502.

[32] D. Chang, Y. Weiyang, Q. Sun, J. Yu, *Phys. Chem. Chem. Phys.* **2017**, *19*, 2067–2072.

[33] M. T. Dove, H. Fang, *Rep. Prog. Phys.* **2016**, *79*, 066503.

[34] O. L. Anderson, *Equations of State of Solids for Geophysics and Ceramic Science*, Oxford University Press, New York, **1995**.

[35] A. Navrotsky, *Geochem. Trans.* **2003**, *4*, 34.

[36] J. Jeevanandam, A. Barhoum, Y. S. Chan, A. Dufresne, M. K. Danquah, *Beilstein J. Nanotechnol.* **2018**, *9*, 1050–1074.

[37] S. Laurent, D. Forge, M. Port, A. Roch, C. Robic, L. V. Elst, R. N. Muller, *Chem. Rev.* **2008**, *108*, 2064–2110.

[38] A. S. Teja, P. Y. Koh, *Prog. Cryst. Growth Charact. Mater.* **2009**, *55*, 22–45.

[39] A. Schätz, O. Reiser, W. J. Stark, *Chem.-Eur. J.* **2010**, *16*, 8950–8967.

[40] L. Machala, J. Tuček, R. Zbořil, *Chem. Mater.* **2011**, *23*, 3255–3272.

[41] J. Tuček, R. Zbořil, A. Namai, S. Ohkoshi, *Chem. Mater.* **2010**, *22*, 6483–6505.

[42] J. Jin, S. Ohkoshi, K. Hashimoto, *Adv. Mater.* **2004**, *16*, 48–51.

[43] S. Ohkoshi, S. Sakurai, J. Jin, K. Hashimoto, *J. Appl. Phys.* **2005**, *97*, 10K312.

[44] D. Gatteschi, M. Fittipaldi, C. Sangregorio, L. Sorace, *Angew. Chem. Int. Ed.* **2012**, *51*, 4792–4800.

[45] B. H. Kim, M. J. Hackett, J. Park, T. Hyeon, *Chem. Mater.* **2014**, *26*, 59–71.

[46] C. R. A. Catlow, S. T. Bromley, S. Hamad, M. Mora-Fonz, A. A. Sokol, S. M. Woodley, *Phys. Chem. Chem. Phys.* **2010**, *12*, 786–811.

[47] D. Wales, *Energy Landscapes: Applications to Clusters, Biomolecules and Glasses*, Cambridge University Press, Cambridge, **2003**.

[48] B. Hartke, *Wiley Interdiscip. Rev.-Comput. Mol. Sci.* **2011**, *1*, 879–887.

[49] S. Heiles, R. L. Johnston, *Int. J. Quantum Chem.* **2013**, *113*, 2091–2109.

[50] Z. X. Cao, M. Duran, M. Solà, *Chem. Phys. Lett.* **1997**, *274*, 411–421.

[51] G. L. Gutsev, S. N. Khanna, B. K. Rao, P. Jena, *J. Phys. Chem. A* **1999**, *103*, 5812–5822.

[52]   A. T. Garcìa-Sosa, M. Castro, *Int. J. Quantum Chem.* **2000**, *80*, 307–319.

[53]   H. Shiroishi, T. Oda, I. Hamada, N. Fujima, *Mol. Simul.* **2004**, *30*, 911–915.

[54]   H. Shiroishi, T. Oda, I. Hamada, N. Fujima, *Polyhedron* **2005**, *24*, 2472–2476.

[55]   N. M. Reilly, J. U. Reveles, G. E. Johnson, S. N. Khanna, A. W. Castleman, *J. Phys. Chem. A* **2007**, *111*, 4158–4166.

[56]   N. M. Reilly, J. U. Reveles, G. E. Johnson, J. M. del Campo, S. N. Khanna, A. M. Köster, A. W. Castleman, *J. Phys. Chem. C* **2007**, *111*, 19086–19097.

[57]   Q. Wang, Q. Sun, M. Sakurai, J. Z. Yu, B. L. Gu, K. Sumiyama, Y. Kawazoe, *Phys. Rev. B* **1999**, *59*, 12672–12677.

[58]   S. López, A. H. Romero, J. Mejía-López, J. Mazo-Zuluaga, J. Restrepo, *Phys. Rev. B* **2009**, *80*, 085107.

[59]   H. Shiroishi, T. Oda, I. Hamada, N. Fujima, *Eur. Phys. J. D* **2003**, *24*, 85–88.

[60]   N. O. Jones, B. V. Reddy, F. Rasouli, S. N. Khanna, *Phys. Rev. B* **2005**, *72*, 165411.

[61]   A. Kirilyuk, A. Fielicke, K. Demyk, G. von Helden, G. Meijer, T. Rasing, *Phys. Rev. B* **2010**, *82*, 020405(R).

[62]   X. L. Ding, W. Xue, Y. P. Ma, Z. C. Wang, S. G. He, *J. Chem. Phys.* **2009**, *130*, 014303.

[63]   S. Kirkpatrick, C. D. Gelatt, M. P. Vecchi, *Science* **1983**, *220*, 671–680.

[64]   T. X. T. Sayle, C. R. A. Catlow, R. R. Maphanga, P. E. Ngoepe, D. C. Sayle, *J. Am. Chem. Soc.* **2005**, *127*, 12828–12837.

[65]   T. X. T. Sayle, P. E. Ngoepe, D. C. Sayle, *J. Mater. Chem.* **2010**, *20*, 10452–10458.

[66]   X. D. Feng, D. C. Sayle, Z. L. Wang, M. S. Paras, B. Santora, A. C. Sutorik, T. X. T. Sayle, Y. Yang, Y. Ding, X. D. Wang, Y. S. Her, *Science* **2006**, *312*, 1504–1508.

[67]   B. T. H. L. Khanh, V. V. Hoang, H. Zung, *Eur. Phys. J. D* **2008**, *49*, 325–332.

[68]   A. Erlebach, *Entwicklung Interatomarer Potentialfunktionen Zur Beschreibung Zweiphasiger Fe₂O₃·SiO₂-Nanopartikel*, Master Thesis, Friedrich Schiller University Jena, Jena, **2013**.

[69]   M. G. De Angelis, G. C. Sarti, *Annu. Rev. Chem. Biomol. Eng. Vol 2* **2011**, *2*, 97–120.

[70]   H. Holback, Y. Yeo, *Pharm. Res.* **2011**, *28*, 1819–1830.

[71]   J. Hou, Q. Zhang, X. Li, Y. Tang, M.-R. Cao, F. Bai, Q. Shi, C.-H. Yang, D.-L. Kong, G. Bai, *J. Biomed. Mater. Res. A* **2011**, *99A*, 684–689.

[72]   N. C. Garbett, J. B. Chaires, *Expert Opin. Drug Discov.* **2012**, *7*, 299–314.

[73]   S. K. Patel, A. Lavasanifar, P. Choi, *Biomaterials* **2010**, *31*, 1780–1786.

[74]   A. O. Kasimova, G. M. Pavan, A. Danani, K. Mondon, A. Cristiani, L. Scapozza, R. Gurny, M. Möller, *J. Phys. Chem. B* **2012**, *116*, 4338–4345.

[75]   L. Huynh, C. Neale, R. Pomès, C. Allen, *Nanomed. Nanotechnol. Biol. Med.* **2012**, *8*, 20–36.

[76]   J. H. Hildebrand, R. L. Scott, *The Solubility of Nonelectrolytes*, 3rd ed., Dover Publications, Inc., New York, **1964**.

[77]   A. F. M. Barton, *Chem. Rev.* **1975**, *75*, 731–753.

[78]   P. J. Flory, *J. Chem. Phys.* **1942**, *10*, 51–61.

[79]   M. L. Huggins, *J. Phys. Chem.* **1942**, *46*, 151–158.

[80]   C. Hansen, M., *Hansen Solubility Parameters: A User's Handbook*, 2nd ed., CRC Press, Boca Raton, FL, **2007**.

[81]   B. Sanchez-Lengeling, L. M. Roch, J. D. Perea, S. Langner, C. J. Brabec, A. Aspuru-Guzik, *Adv. Theory Simul.* **2019**, *2*, 1800069.

[82]   B. D. Anderson, *J. Pharm. Sci.* **2018**, *107*, 24–33.

[83]   E. R. Turpin, V. Taresco, W. A. Al-Hachami, J. Booth, K. Treacher, S. Tomasi, C. Alexander, J. Burley, C. A. Laughton, M. C. Garnett, *Mol. Pharm.* **2018**, *15*, 4654–4667.

[84]   A. D. Glova, S. G. Falkovich, D. I. Dmitrienko, A. V. Lyulin, S. V. Larin, V. M. Nazarychev, M. Karttunen, S. V. Lyulin, *Macromolecules* **2018**, *51*, 552–563.

[85]   S. V. Lyulin, A. A. Gurtovenko, S. V. Larin, V. M. Nazarychev, A. V. Lyulin, *Macromolecules* **2013**, *46*, 6357–6363.

[86]   D. N. Theodorou, U. W. Suter, *Macromolecules* **1985**, *18*, 1467–1478.

[87]   R. L. Akkermans, N. A. Spenley, S. H. Robertson, *Mol. Simul.* **2013**, *39*, 1153–1164.

[88]   F. H. Stillinger, T. A. Weber, *Science* **1984**, *225*, 983–989.

[89]   F. H. Stillinger, *J. Chem. Phys.* **1988**, *88*, 7818–7825.

[90]   P. G. Debenedetti, F. H. Stillinger, *Nature* **2001**, *410*, 259–267.

[91]   F. Sciortino, W. Kob, P. Tartaglia, *Phys. Rev. Lett.* **1999**, *83*, 3214–3217.

[92]   A. Heuer, *J. Phys. Condens. Matter* **2008**, *20*, 373101.

[93]   D. J. Wales, *Phys. Biol.* **2005**, *2*, S86–S93.

[94]   D. J. Wales, T. V. Bogdan, *J. Phys. Chem. B* **2006**, *110*, 20765–20776.

[95]   F. H. Stillinger, P. G. Debenedetti, *Annu. Rev. Condens. Matter Phys.* **2013**, *4*, 263–285.

[96]   S. Dixit, J. Crain, W. C. K. Poon, J. L. Finney, A. K. Soper, *Nature* **2002**, *416*, 829–832.

[97]   A. K. Soper, L. Dougan, J. Crain, J. L. Finney, *J. Phys. Chem. B* **2006**, *110*, 3472–3476.

[98]   R. Kjellander, E. Florin, *J. Chem. Soc. Faraday Trans. 1* **1981**, *77*, 2053.

[99]   Z. J. Cárdenas, D. M. Jiménez, F. Martínez, *J. Mol. Liq.* **2015**, *211*, 233–238.

[100] Y. Guerrieri, K. V. Pontes, G. M. N. Costa, M. Embiruçu in *Polymerization*, (Ed.: A. D. S. Gomes), InTechOpen, Rijeka, **2012**, pp. 357–402.

[101] W. Chapman, K. Gubbins, G. Jackson, M. Radosz, *Fluid Phase Equilib.* **1989**, *52*, 31–38.

[102] W. G. Chapman, K. E. Gubbins, G. Jackson, M. Radosz, *Ind. Eng. Chem. Res.* **1990**, *29*, 1709–1721.

[103] Y. Song, S. M. Lambert, J. M. Prausnitz, *Macromolecules* **1994**, *27*, 441–448.

[104] Y. Song, S. M. Lambert, J. M. Prausnitz, *Ind. Eng. Chem. Res.* **1994**, *33*, 1047–1057.

[105] Y. Song, S. M. Lambert, J. M. Prausnitz, *Chem. Eng. Sci.* **1994**, *49*, 2765–2775.

[106] M. Fermeglia, S. Pricl, *AIChE J.* **1999**, *45*, 2619–2627.

[107] M. Fermeglia, S. Pricl, *Fluid Phase Equilib.* **1999**, *158-160*, 49–58.

[108] J. M. Prausnitz, R. N. Lichtenthaler, E. G. de Azevedo, *Molecular Thermodynamics of Fluid-Phase Equilibria*, 3rd ed, Prentice Hall PTR, Upper Saddle River, NJ, **1999**.

[109] D. Frenkel, B. Smit, *Understanding Molecular Simulations*, Academic Press, London, **2002**.

[110] P. W. Atkins, J. De Paula, *Atkins' Physical Chemistry*, 9th ed, Oxford University Press, Oxford, New York, **2010**.

[111] A. van de Walle, M. Asta in *Handbook of Materials Modeling*, (Ed.: S. Yip), Springer Netherlands, Dordrecht, **2005**, pp. 349–365.

[112] R. Grau-Crespo, S. Hamad, C. R. A. Catlow, N. H. de Leeuw, *J. Phys. Condens. Matter* **2007**, *19*, 256201.

[113] P. Vinet, J. Ferrante, J. R. Smith, J. H. Rose, *J. Phys. C Solid State Phys.* **1986**, *19*, L467–L473.

[114] P. Vinet, J. R. Smith, J. Ferrante, J. H. Rose, *Phys. Rev. B* **1987**, *35*, 1945–1953.

[115] F. D. Murnaghan, *Proc. Natl. Acad. Sci.* **1944**, *30*, 244–247.

[116] F. Birch, *Phys. Rev.* **1947**, *71*, 809–824.

[117] D. C. Wallace, *Thermodynamics of Crystals*, Dover Publications, New York, **1998**.

[118] Y. Marcus, *Chem. Rev.* **2013**, *113*, 6536–6551.

[119] E. Wilhelm, *J. Solut. Chem.* **2014**, *43*, 525–576.

[120] E. Wilhelm in *Enthalpy and Internal Energy*, (Eds.: E. Wilhelm, T. Letcher), Royal Society of Chemistry, Cambridge, **2017**, pp. 447–476.

[121] M. H. Jacobs, B. H. de Jong, *Phys. Chem. Miner.* **2005**, *32*, 614–626.

[122] F. Guyot, Y. Wang, P. Gillet, Y. Ricard, *Phys. Earth Planet. Inter.* **1996**, *98*, 17–29.

[123] S. W. Kieffer, *Rev. Geophys.* **1979**, *17*, 1.

[124] J. F. Nye, *Physical Properties of Crystals: Their Representation by Tensors and Matrices*, 1st, Clarendon Press, Oxford University Press, Oxford, New York, **1985**.

[125] T. Barron, J. Collins, G. White, *Adv. Phys.* **1980**, *29*, 609–730.

[126] A. Togo, I. Tanaka, *Scr. Mater.* **2015**, *108*, 1–5.

[127] G. Mansoori, *Fluid Phase Equilib.* **1993**, *87*, 1–22.

[128] M. L. Huggins, *J. Am. Chem. Soc.* **1942**, *64*, 1712–1719.

[129] I. Teraoka, *Polymer Solutions: An Introduction to Physical Properties*, John Wiley & Sons, Inc., New York, **2002**.

[130] B. A. Wolf in *Polymer Thermodynamics: Liquid Polymer-Containing Mixtures*, (Eds.: B. A. Wolf, S. Enders), Springer Berlin Heidelberg, Berlin, Heidelberg, **2011**, pp. 1–66.

[131] H. Sun, Z. Jin, C. Yang, R. L. C. Akkermans, S. H. Robertson, N. A. Spenley, S. Miller, S. M. Todd, *J. Mol. Model.* **2016**, *22*, 47.

[132] B. Schaefer, S. Lambert, Y. Song, J. Prausnitz, Phase Equilibria in Strong Polar Fluids Using a Perturbed Hard-Sphere-Chain Equation of State Combined with Three Different Association Models (Report No. LBL-36814), tech. rep. LBL-36814, USDOE, Washington DC, United States, **1994**.

[133] T. Boublík, *J. Chem. Phys.* **1970**, *53*, 471–472.

[134] G. A. Mansoori, N. F. Carnahan, K. E. Starling, T. W. Leland, *J. Chem. Phys.* **1971**, *54*, 1523–1525.

[135] Y. Song, T. Hino, S. M. Lambert, J. M. Prausnitz, *Fluid Phase Equilib.* **1996**, *117*, 69–76.

[136] T. Hino, S. M. Lambert, D. S. Soane, J. M. Prausnitz, *AIChE J.* **1993**, *39*, 837–845.

[137] G. ten Brinke, F. E. Karasz, *Macromolecules* **1984**, *17*, 815–820.

[138] I. C. Sanchez, A. C. Balazs, *Macromolecules* **1989**, *22*, 2325–2331.

[139] J. D. Weeks, D. Chandler, H. C. Andersen, *J. Chem. Phys.* **1971**, *54*, 5237–5247.

[140] M. Born, R. Oppenheimer, *Ann. Phys.* **1927**, *389*, 457–484.

[141] J. P. Perdew, Stefan Kurth in *A Primer in Density Functional Theory*, (Eds.: C. Fiolhais, F. Nogueira, M. A. L. Marques), Lecture Notes in Physics, Springer, Berlin, Heidelberg, **2003**, pp. 1–55.

[142] W. Koch, M. C. Holthausen, *A Chemist's Guide to Density Functional Theory*, Wiley-VCH, Weinheim, New York, **2001**.

[143] K. Burke, L. O. Wagner, *Int. J. Quantum Chem.* **2013**, *113*, 96–101.

[144] J. P. Perdew, A. Ruzsinszky, G. I. Csonka, O. A. Vydrov, G. E. Scuseria, L. A. Constantin, X. L. Zhou, K. Burke, *Phys. Rev. Lett.* **2008**, *100*, Phys Rev Lett, 136406.

[145] J. P. Perdew, A. Ruzsinszky, G. I. Csonka, O. A. Vydrov, G. E. Scuseria, L. A. Constantin, X. L. Zhou, K. Burke, *Phys. Rev. Lett.* **2009**, *102*, Phys Rev Lett, 136406.

[146] M. Born, J. E. Mayer, *Z. Phys.* **1932**, *75*, 1–18.

[147] M. T. Dove, *Introduction to Lattice Dynamics*, Cambridge University Press, Cambridge, **1993**.

[148] Y. Le Page, P. Saxe, *Phys. Rev. B* **2002**, *65*, 104104.

[149] N. Metropolis, A. W. Rosenbluth, M. N. Rosenbluth, A. H. Teller, E. Teller, *J. Chem. Phys.* **1953**, *21*, 1087–1092.

[150] L. Verlet, *Phys. Rev.* **1967**, *159*, 98–103.

[151] D. Thirumalai, R. D. Mountain, T. R. Kirkpatrick, *Phys. Rev. A* **1989**, *39*, 3563–3574.

[152] R. Palmer, *Adv. Phys.* **1982**, *31*, 669–735.

[153] J. C. Mauro, M. M. Smedskjaer, *J. Non-Cryst. Solids* **2014**, *396-397*, 41–53.

[154] S. Nosé, *J. Chem. Phys.* **1984**, *81*, 511–519.

[155] W. G. Hoover, *Phys. Rev. A* **1985**, *31*, 1695–1697.

[156] H. J. C. Berendsen, J. P. M. Postma, W. F. van Gunsteren, A. DiNola, J. R. Haak, *J. Chem. Phys.* **1984**, *81*, 3684–3690.

[157] M. Parrinello, A. Rahman, *J. Appl. Phys.* **1981**, *52*, 7182–7190.

[158] J.-Y. Yi, J. Bernholc, P. Salamon, *Comput. Phys. Commun.* **1991**, *66*, 177–180.

[159] B. Helmich, M. Sierka, *J. Comput. Chem.* **2012**, *33*, 134–140.

[160] G. Kresse, J. Furthmüller, *Phys. Rev. B* **1996**, *54*, 11169–11186.

[161] G. Kresse, J. Furthmüller, *Comput. Mater. Sci.* **1996**, *6*, 15–50.

[162] S. Grimme, J. Antony, S. Ehrlich, H. Krieg, *J. Chem. Phys.* **2010**, *132*, 154104.

[163] P. E. Blöchl, *Phys. Rev. B* **1994**, *50*, Phys Rev B, 17953–17979.

[164] G. Kresse, D. Joubert, *Phys. Rev. B* **1999**, *59*, Phys Rev B, 1758–1775.

[165] H. J. Monkhorst, J. D. Pack, *Phys. Rev. B* **1976**, *13*, Phys Rev B, 5188–5192.

[166] TURBOMOLE V6.5 2013, a Development of University of Karlsruhe and Forschungszentrum Karlsruhe GmbH, 1989-2007, TURBOMOLE GmbH, since 2007; Available from http://www.turbomole.com.

[167] R. Ahlrichs, M. Bär, M. Häser, H. Horn, C. Kölmel, *Chem. Phys. Lett.* **1989**, *162*, 165–169.

[168] F. Furche, R. Ahlrichs, C. Hättig, W. Klopper, M. Sierka, F. Weigend, *WIREs Comput. Mol. Sci.* **2014**, *4*, 91–100.

[169] S. H. Vosko, L. Wilk, M. Nusair, *Can. J. Phys.* **1980**, *58*, 1200–1211.

[170] C. T. Lee, W. T. Yang, R. G. Parr, *Phys. Rev. B* **1988**, *37*, 785–789.

[171] A. D. Becke, *J. Chem. Phys.* **1993**, *98*, 5648–5652.

[172] F. Weigend, R. Ahlrichs, *Phys. Chem. Chem. Phys.* **2005**, *7*, 3297–3305.

[173] M. Sierka, A. Hogekamp, R. Ahlrichs, *J. Chem. Phys.* **2003**, *118*, 9136–9148.

[174] F. Weigend, *Phys. Chem. Chem. Phys.* **2006**, *8*, 1057–1065.

[175] S. Plimpton, *J. Comput. Phys.* **1995**, *117*, 1–19.

[176] C. G. Shull, W. A. Strauser, E. O. Wollan, *Phys. Rev.* **1951**, *83*, 333–345.

[177] R. L. Blake, R. E. Hessevick, T. Zoltai, L. W. Finger, *Am. Mineral.* **1966**, *51*, 123–129.

[178] R. Grau-Crespo, A. Y. Al-Baitai, I. Saadoune, N. H. De Leeuw, *J. Phys.: Condens. Matter* **2010**, *22*, 255401.

[179] W. Shinoda, M. Shiga, M. Mikami, *Phys. Rev. B* **2004**, *69*, 134103.

[180] M. E. Tuckerman, J. Alejandre, R. López-Rendón, A. L. Jochim, G. J. Martyna, *J. Phys. A-Math. Gen.* **2006**, *39*, 5629–5651.

[181] M. Chi, *Thermodynamic Modelling of Polymer-Solvent Solubility*, Master Thesis, Friedrich Schiller University Jena, Jena, **2018**.

[182] J. A. Faucher, J. V. Koleske, E. R. Santee, J. J. Stratta, C. W. Wilson, *J. Appl. Phys.* **1966**, *37*, 3962–3964.

[183] L. Vegard, *Z. Phys.* **1921**, *5*, 17–26.

[184] C. Thieme, M. Schlesier, C. Bocker, G. Buzatto de Souza, C. Rüssel, *ACS Appl. Mater. Interfaces* **2016**, *8*, 20212–20219.

[185] M. Kracker, L. Vladislavova, C. Thieme, T. Zscheckel, K. Thieme, T. Höche, C. Rüssel, *RSC Adv.* **2017**, *7*, 44834–44842.

[186] N. Chawla, B. Patel, M. Koopman, K. Chawla, R. Saha, B. Patterson, E. Fuller, S. Langer, *Mater. Charact.* **2002**, *49*, 395–407.

[187] S. Ozaki, Y. Aoki, T. Osada, K. Takeo, W. Nakao, *J. Am. Ceram. Soc.* **2018**, *101*, 3191–3204.

[188] C. Thieme, H. Görls, C. Rüssel, *Sci. Rep.* **2015**, *5*, 18040.

[189] C. Q. Sun, *Prog. Solid State Ch.* **2007**, *35*, 1–159.

[190] E. Tronc, C. Chanéac, J. P. Jolivet, *J. Solid State Chem.* **1998**, *139*, 93–104.

[191] C. Stötzel, H. D. Kurland, J. Grabow, S. Dutz, E. Müller, M. Sierka, F. A. Müller, *Cryst. Growth Des.* **2013**, *13*, 4868–4876.

[192] E. Taboada, M. Gich, A. Roig, *ACS Nano* **2009**, *3*, 3377–3382.

[193] J. E. Mark, *Polymer Data Handbook,* Oxford University Press, Inc., New York, **1999**.

[194] C. M. Roland, *Soft Matter* **2008**, *4*, 2316.

[195] A. Eliassi, H. Modarress, G. A. Mansoori, *J. Chem. Eng. Data* **1998**, *43*, 719–721.

[196] T. Hino, J. M. Prausnitz, *Fluid Phase Equilib.* **1997**, *138*, 105–130.

[197] W. Wagner, A. Pruß, *J. Phys. Chem. Ref. Data* **2002**, *31*, 387–535.

[198] Y. C. Bae, S. M. Lambert, D. S. Soane, J. M. Prausnitz, *Macromolecules* **1991**, *24*, 4403–4407.

[199] G. N. Malcolm, J. S. Rowlinson, *Trans. Faraday Soc.* **1957**, *53*, 921.

Publications

[I] M. Zekri, **A. Erlebach**, A. Herrmann, K. Damak, C. Rüssel, M. Sierka, R. Maâlej, Structure Prediction of Rare Earth Doped BaO and MgO Containing Aluminosilicate Glasses – the Model Case of Gd_2O_3, *Materials*, **2018**, *11*, 1790.

[II] C. Thieme, **A. Erlebach**, C. Patzig, K. Thieme, M. Sierka, Thomas Höche, C. Rüssel, WO_3 as nucleating agent for $BaO/SrO/ZnO/SiO_2$ glasses – experiments and simulations, *CrystEngComm*, **2018**, *20*, 4565-4574.

[III] L. Wondraczek, Z. Pan, T. Palenta, **A. Erlebach**, S. T. Misture, M. Sierka, M. Micoulaut, U. Hoppe, J. Deubener, G. N. Greaves, Kinetics of decelerated melting, *Adv. Sci.* **2018**, 1700850.

[IV] C. Thieme, M. Kracker, **A. Erlebach**, C. Patzig, M. Sierka, T. Höche, C. Rüssel, Effect of Al_2O_3 on Phase formation and thermal expansion of a $BaO-SrO-ZnO-SiO_2$ glass ceramic, *Ceram. Int.* **2018**, *44*, 2098–2108.

[V] **A. Erlebach**, K. Thieme, M. Sierka, C. Rüssel, Structure and crystallization of SiO_2 and B_2O_3 doped lithium disilicate glasses from theory and experiment, *Phys. Chem. Chem. Phys.* **2017**, *19*, 25298-25308.

[VI] B. P. Rodrigues, C. Hühn, **A. Erlebach**, D. Mey, M. Sierka, L. Wondraczek, Parametrization in models of subcritical glass fracture: Activation offset and concerted activation, *Front. Mater.* **2017**, *4*, 20.

[VII] C. Hühn, **A. Erlebach**, D. Mey, L. Wondraczek, M. Sierka, Ab initio energetics of Si-O bond cleavage, *J. Comp. Chem.* **2017**, *38*, 2349-2353.

[VIII] A. E. Seitz, M. Eckhardt, S. S. Sen, **A. Erlebach**, E. V. Peresypkina, H. W. Roesky, M. Sierka, M. Scheer, Different reactivity of As_4 towards disilenes and silylenes, *Angew. Chem. Int. Ed.* **2017**, *56*, 6655-6659.

[IX] A. E. Seitz, M. Eckhardt, **A. Erlebach**, E. V. Peresypkina, M. Sierka, M. Scheer, Pnictogen-silicon analogues of benzene, *J. Am. Chem. Soc.* **2016**, *138*, 10433-10436.

[X] **A. Erlebach**, T. Ott, C. Otzen, S. Schubert, J. Czaplewska, U. S. Schubert and M. Sierka, Thermodynamic compatibility of actives encapsulated into PEG-PLA nanoparticles: *In silico* predictions and experimental verification, *J. Comp. Chem.* **2016**, *37*, 2220-2227.

[XI] **A. Erlebach**, H.-D. Kurland, J. Grabow, F. A. Müller, M. Sierka, Structure evolution of nanoparticulate Fe_2O_3, *Nanoscale* **2015**, *7*, 2960-2969.

[XII] **A. Erlebach**, C. Hühn, R. Jana, M. Sierka, Structure and Magnetic Properties of $(Fe_2O_3)_n$ Clusters ($n = 1$-5), *Phys. Chem. Chem. Phys.* **2014**, *16*, 26421-26426.

Affidavit

Hereby, I declare that I have prepared independently the present work entitled "Methods for *in silico* design of innovative materials" without the unauthorized help of third parties and without the use of other help and literature except for those stated. The data and concepts taken directly or indirectly from other sources are clearly indicated. All contents prepared with assistance of or in collaboration with other people, respectively, are clearly stated at the respective text passages and summarized in the acknowledgments.

Other persons were not involved in the preparation of the present work. In particular, I did not used the help of advisory services (doctoral consultants or other persons) for this purpose. I provided no one neither directly nor indirectly monetary benefits for work related to the content of the dissertation submitted.

This work has not been submitted to another institution in Germany or abroad in the same or similar form.

I am aware of the promotion regulation of the Faculty of Physics and Astronomy of the Friedrich Schiller University Jena.

I hereby affirm that to the best of my knowledge I told nothing but the truth and did not concealed anything.

Place, date:

_____

Signature:

_____

Ehrenwörtliche Erklärung

Ich erkläre hiermit ehrenwörtlich, dass ich die vorliegende Arbeit mit dem Titel "Methods for *in silico* design of innovative materials" selbständig ohne unzulässige Hilfe Dritter und ohne Benutzung anderer als der angegebenen Hilfsmittel und Literatur angefertigt habe. Die aus anderen Quellen direkt oder indirekt übernommenen Daten und Konzepte sind unter Angabe der Quelle gekennzeichnet. Sämtliche Inhalte die mit Hilfe bzw. in Zusammenarbeit mit anderen Personen erstellt wurden sind an den entsprechenden Textstellen klar gekennzeichnet und in der Danksagung zusammengefasst.

Weitere Personen waren an der inhaltlich-materiellen Erstellung der vorliegenden Arbeit nicht beteiligt. Insbesondere habe ich hierfür nicht die entgeltliche Hilfe von Vermittlungs- bzw. Beratungsdiensten (Promotionsberater oder andere Personen) in Anspruch genommen. Niemand hat von mir unmittelbar oder mittelbar geldwerte Leistungen für Arbeiten erhalten, die im Zusammenhang mit dem Inhalt der vorgelegten Dissertation stehen.

Die Arbeit wurde bisher weder im In- noch im Ausland in gleicher oder ähnlicher Form einer anderen Prüfungsbehörde vorgelegt.

Die geltende Promotionsordnung der Physikalisch-Astronomischen Fakultät ist mir bekannt. Ich versichere ehrenwörtlich, dass ich nach bestem Wissen die reine Wahrheit gesagt und nichts verschwiegen habe.

Ort, Datum:

_____

Unterschrift:

_____